UNIVERSITY OF CALIFORNIA
SANTA CRUZ

THE PROMISE AND CHALLENGE OF SUBSTELLAR ATMOSPHERES AT INCREASED SPECTRAL RESOLUTION

A dissertation submitted in partial satisfaction of the
requirements for the degree of

Doctor of Philosophy

in

ASTRONOMY AND ASTROPHYSICS

by

Callie E. Hood

September 2023

The Dissertation of Callie E. Hood is approved:

Jonathan J. Fortney, Chair

Andrew Skemer

Xi Zhang

Michael R. Line

Peter F. Biehl
Vice Provost and Dean of Graduate Studies

Table of Contents

List of Figures

List of Tables

Abstract

The Promise and Challenge of Substellar Atmospheres at Increased Spectral Resolution

by

Callie E. Hood

The spectral resolution of instruments used to characterize substellar atmospheres has greatly increased over the past decade. As we more frequently observe exoplanet and brown dwarf atmospheres at higher spectral resolution, more work is needed to assess both what new information is contained in these improved observations as well as how our current modeling tools fall short in accurately reproducing these spectra. My dissertation has examined this question from multiple angles to ultimately prepare the field to better understand substellar atmospheres through the better quality spectra we will receive from the JWST and the upcoming ELTs. First, I present how high-resolution cross-correlation spectroscopy (R $\sim$ 25,000 to 100,000) will allow us to probe the regions in the atmospheres of sub-Neptune exoplanets above the clouds or hazes which obscure molecular features in observations at low spectral resolution. Using theoretical models of high-resolution observations for a typical hazy sub-Neptune, we calculate the signal-to-noise of these spectra required to robustly detect a host of molecules as a function of spectral resolution and wavelength coverage to aid in planning future observations and instruments.

Next, I present two projects focused on adapting atmospheric retrieval methods

for medium-resolution spectra of brown dwarfs. I first describe applying a GPU-version of the CHIMERA retrieval framework to a high signal-to-noise, medium-resolution (R$\sim$6000) FIRE spectrum of a T9 dwarf from 0.85-2.5 μm. At 60$\times$ higher spectral resolution than previous brown dwarf retrievals, a number of novel challenges arise, which I explore. I show that compared to retrieval results from a R$\sim$100 spectrum of the same object, constraints on atmospheric abundances improve by an order of magnitude or more with increased spectral resolution.

Finally, I apply lessons learned from this project to JWST NIRSpec/G395H (R$\sim$2700, 2.87 - 5.14 μm) observations of a T8 dwarf, presenting the first retrieval analysis taking full advantage of the maximum spectral resolution available with NIRSpec. I obtain precise ($\sim$ 0.02 dex) abundance constraints for a number of species, which indicate shortcomings in our understanding of disequilibrium chemistry in brown dwarf atmospheres. I also present the measured ^{12}CO/^{13}CO ratio for this brown dwarf, making it the fourth and coldest ($\sim$ 760 K) extrasolar object with such a measurement. Together, these projects illustrate the power of high-quality, medium-to-high resolution spectra to precisely constrain atmospheric properties, furthering our understanding of the formation and atmospheres of substellar objects.

For my grandfather, Gary Hollifield.

Personal Acknowledgments

I would first like to thank my PhD advisor, Jonathan Fortney. You have been such a constant source of guidance and support throughout my graduate career. Thank you for never making me feel like I've asked a dumb question and teaching me so much about astronomy, both as a subject and career path. I really appreciate how much you care about your mentees, not only as scientists, but as whole people. I also thank you for fostering such a supportive and welcoming research environment which has been critical to my sense of belonging at UCSC. To that end, I particularly want to acknowledge the numerous postdocs, graduate students, and undergraduates from the Fortney group and broader UCSC exoplanet community who have taught me so much, including Natasha, Naor, Emily, Xinting, Kat, Daniel, Maggie, Zafar, Lorraine, and Sagnick.

I also want to thank the numerous other mentors who have guided me along the way. To Jayne Birkby, thank you for advising my first ever exoplanet project, igniting my interest in exoplanet atmospheres and high resolution spectroscopy, and pointing me to UCSC. To Caroline Morley, thank you for sharing your modeling tools with me, answering all my questions, and being a welcoming presence at many exoplanet workshops and conferences throughout the years. To Mike Line, thank you for teaching me everything I know about retrievals, from explaining likelihood mappings during our first conversation at OWL to becoming a secondary advisor who has been critical to the success all of my projects. To Jackie Faherty, thank you for sharing your data with me and providing helpful commentary and insight into brown dwarf observations. I would also like to thank Andy Skemer and Xi Zhang for teaching some of my favorite courses

at UCSC and serving on my Qualifying and Defense Committees.

My time at UCSC has been greatly shaped for the better by the community and friendships I formed. I am so glad I got to enter grad school with my cohort, who were an important source of support throughout the years. I want to thank the entire astronomy grad student community for being so welcoming and supportive, particularly Miranda, Annie, Rachel, Erica, and Evan. Thanks to Molly and Aribeth for opening their home to me and being my first friends in Santa Cruz. My COVID bubble was essential to my mental health during the pandemic and I can't thank you all enough.

To Zack, despite our surface differences, I knew we connected and would be friends very early on and I'm so glad I was right. Thank you for always being down to watch any flavor of cozy trash with me and talk about all the random related trivia we can think of the whole time. To Enia and Amanda, I am beyond grateful for the joy and friendship y'all have brought to my life that I know will be continue for a long time. Enia, I am inspired by so much about how you move through the world. You are always so fun to be around but at the same time available for an in depth conversation anytime. I am so glad we both ended up in Baltimore and you're only a short drive away. Amanda, the home we built together in Santa Cruz meant the world to me and will always hold a special place in my heart. Thank you for listening to every detail of my day and holding so much space for me. Though you didn't come to Maryland with the rest of us, I know I can always count on you for a sympathetic ear or motivational message anytime (and you're only a short train ride away). To Matt, I can't thank you enough for the companionship and support you have offered me during the last half of

my grad school career. Thank you for always listening to my many worries and helping me prioritize myself when needed. I am so proud of and thankful for the life we have built together in Baltimore. Relatedly, to Willow, thanks for finally making me a cat mom and the many cuddles that got me through the home stretch of this thesis.

I have also been incredibly supported by the friendships I made prior to graduate school. I thank my physics friends at UNC who spent many hours working on problem sets or bemoaning difficult labs for me. The Women in Physics group at UNC was an invaluable source of inspiration and community. To Anna, Anne, Ariel, Caitlyn, and Shafali, thank you so much for all of the laughter and encouragement throughout our time as Tarheels. I also thank my Hickory friends - Elizabeth, Laura, Anna, Mary, and Sarah (ECLAMS), for their ongoing love and support that have shaped me into the woman I am today. I am so lucky to have made foundational friendships at such a young age. You all have been in my life for more than a decade and I know will continue to be there for me for many more.

Finally, my family have been my number one fans and supporters for my entire life. I want to especially thank my grandparents Judy and Gary Hollifield for their unending love and care which allowed me to do so much as a young person. To my brother Wilson, I am so thankful for your continued friendship and encouragement as we became adults. To my parents, Sandi and David Hood, I can never thank you enough for everything you have given me. I am so lucky to have such great parents and guiding lights in my life.

Scientific Acknowledgements and Published Material

My thesis work was supported by the UCSC Dissertation Year Fellowship. The computational work for this thesis was mostly carried out on the lux supercomputer at UC Santa Cruz, funded by NSF MRI grant AST 1828315. I would like to thank Brant Robertson and Josh Sonstroem for their hard work maintaining lux.

I would like to thank the many coauthors that contributed to the works that make up this thesis. The text of this dissertation includes reprints of the following previously published material led by Callie Hood.

Chapter 2 was previously published as Hood et al. 2020. I was responsible for performing most of the analysis (with the exception of the exposure time calculations performed by co-author Emily Martin), making all figures, and writing the text. I thank co-authors Jonathan Fortney, Michael Line, and Jayne Birkby for their advice and feedback. I thank co-authors Caroline Morley and Zafar Rustamkulov for sharing their modeling tools with me. I thank co-author Emily Martin for the previously-mentioned exposure time calculations and for further guidance on connecting my results to observability. I also thank co-authors Roxana Lupu and Richard Freedman for their work on the opacity calculations used in these models.

Chapter 3 was previously published as Hood et al. 2023. I was responsible for performing the retrieval analysis, creating the figures, and writing the text. I thank co-author Jonathan Fortney for his guidance and comments. I thank co-author Mike Line for assistance with applying and adapting CHIMERA. I thank co-author Jacqueline Faherty for providing the reduced and stitched FIRE spectrum.

Chapter 4 contains material soon to be submitted to Nature Astronomy. I

was responsible for performing the retrieval analysis, creating the figures, and writing most of the text, with the exceptions of the sections on the observations and Sonora Elf Owl grid analysis in the methods. I would like to thank my co-authors, Jonathan Fortney and Mike Line for their guidance and feedback. I thank Jacqueline Faherty for providing me with reduced and calibrated spectra from JWST/NIRSpec, IRTF/SpeX, and Spitzer/IRS. I thank Sagnick Mukherjee for his work on fitting the observed spectra to his Sonora Elf Owl grid of models.

Chapter 1

Introduction

1.1 Exoplanet and Brown Dwarf Synergy

At the Cool Stars 9 conference in 1995, two exciting discoveries were announced: the first exoplanet around a main sequence star, 51 Peg b (Mayor & Queloz 1995), and the first confirmed brown dwarf, Gliese 229B (Nakajima et al. 1995). In the decades since, the exoplanet and brown dwarf fields have both rapidly expanded and developed, building on the foundation of preceding work on stellar and solar system astrophysics. Thousands of exoplanets of have been discovered since 1995, demonstrating a remarkable diversity of planetary systems wildly different than our own. Detected exoplanets include gas giants with large gas envelopes, Neptune-like ice giants with thinner envelopes around icy cores, sub-Neptunes with sizes between that of Earth of Neptune, and terrestrial, rocky planets similar to Earth. At the same time, multitudes of brown dwarfs have similarly been found, including $\sim$ 525 within 20 pc of the Sun (Kirkpatrick et al. 2021).

The line between gas giant exoplanet and brown dwarfs is a blurry one. The International Astronomical Union definition mostly relies on mass, with brown dwarfs consisting of objects too small to fuse hydrogen but massive enough to fuse deuterium ($\sim$13 M_{Jup} - 73 M_{Jup} for a solar metallicity object) regardless of location or formation. Objects below the minimum deuterium fusing mass orbiting a star or brown dwarf and have a mass ratio with the central object below the L_4/L_5 instability are classified as planets, while free-floating objects below the cutoff are considered sub-brown dwarfs (Lecavelier des Etangs & Lissauer 2022). However, formation-based definitions have also been proposed, where the lowest-mass objects from gravitational collapse in molecular clouds are considered brown dwarfs and objects that form "bottom-up" from accretion in protoplanetary disks are considered planets, regardless of mass (Chabrier et al. 2014). However, mass is an easier property to probe than formation pathway, although observational signatures of the different formation scenarios have been proposed (e.g., Chabrier et al. 2014; Y. Zhang et al. 2021a).

Brown dwarfs and gas giant planets have a lot in common. Both are expected to host hydrogen-dominated atmospheres, with secondary elements like C, O, and N nevertheless having significant impacts (Lodders & Fegley 2002). Furthermore, brown dwarfs and gas giant exoplanets can span a similar temperature range, indicating the potential for similar chemical and physical processes at work in their atmospheres (Faherty et al. 2016). While the characterization of exoplanet atmospheres has greatly progressed in the past decade, isolated brown dwarfs are still often significantly easier to observe due to the lack of contamination from a host star. Thus, brown dwarf spectra

act as an important testbed for our understanding of the relevant atmospheric processes at these temperatures.

1.2 Observing Substellar Atmospheres

1.2.1 Observations of Transiting Planets

For planets that happen to "transit," or pass directly in front of their host stars from our point of view, multiple techniques can be used to probe their atmospheres.

Transmission Spectroscopy: The first used(Charbonneau et al. 2002) and most common method for detecting exoplanet atmospheres involves spectroscopy taken during the planet's transit. The transit depth is given by R_p^2/R_{star}^2, where R_p is the planet radius and R_{star} is the radius of the host star (e.g., Seager & Lissauer 2010). As light from the host star is filtered through the planet's atmosphere, the observed radius of the planet and therefore transit depth will appear larger at wavelengths where the atmosphere is opaque. Thus, we construct the transmission spectrum of the planet by measuring the transit depth as a function of wavelength. Since chemical species absorb light at unique sets of wavelengths, features in the transmission spectrum can be related to the atmosphere's composition.

Dozens of exoplanet atmospheres have been characterized with transmission spectroscopy, particularly using the Hubble Space Telescope (HST), showcasing a range of spectral features and detected molecules. Muted features attributed to clouds or hazes in the upper atmosphere have been seen for a multitude of planets (e.g., Sing et al. 2016). Sub-Neptune planets have been particularly difficult to investigate with this

technique. For example, observations of the very-well studied sub-Neptune GJ 1214b show little variation in transit depth as a function of wavelength. Kreidberg et al. (2014) used 60 orbits of HST/WFC3 observations to construct an ultra-precise transmission spectrum of GJ 1214b that was consistent with a flat line, indicating the presence of aerosol opacity obscuring any molecular features in the spectrum. Thus, transmission spectra can provide some limits on clouds or hazes in exoplanet atmospheres, but other techniques may be needed to fully probe the characteristics of these objects.

Secondary Eclipse Spectroscopy: We can also compare the observed flux just before a planet passes behind its star to when the planet is blocked by the star (the secondary eclipse). The difference of these two fluxes represents the total flux emitted and/or reflected by the planet. The resulting emission spectrum contains thermal temperature information and probes deeper pressures than in transmission, providing constraints on the thermal structure of the atmosphere in addition to its composition. These observations are often taken in the infrared, where the host star is dimmer and the planet's thermal emission peaks. As such, the first confirmed secondary eclipse observations were taken with the Spitzer telescope (Charbonneau et al. 2005; Deming et al. 2005) and many more planets have been observed similarly since. Time-resolved lightcurves during ingress and egress can also be used for "eclipse mapping," producing a brightness map of latitudinal and longitudinal variation across the dayside of a transiting planet (e.g., Rauscher et al. 2019).

Phase Curves: The phase curve of a transiting planet shows how the planet's brightness changes across a full orbit. Phase curves can be used to probe the longitudinal

inhomogeneities of an exoplanet's atmosphere, such as day-to-night contrasts and a hot spot offset (Showman & Guillot 2002). Many close-in gas giants have observed phase curves, allowing for increased understanding of the three-dimensional nature of these objects (see Parmentier & Crossfield (2018) for a review). The launch of JWST allows for the extension of this technique to smaller, cooler atmospheres. Kempton et al. (2023) present a spectroscopic phase curve of GJ 1214b in the mid-infrared, providing more detailed information about the sub-Neptune's atmosphere than was previously possible with transmission spectra.

1.2.2 Observations of Directly Imaged Companions

With the aid of sophisticated instrumentation like extreme adaptive optics and coronagraphs, we can directly observe planet or brown dwarf companions that are bright and orbit at wide distances from their host stars. Such planets are young and therefore still glowing from their heat of formation. Observing the light from these planets at multiple wavelengths allows for another method of measuring the thermal emission spectrum of an exoplanet. Like thermal emission spectra of transiting planets, spectroscopy of directly imaged planets can allow for robust constraints on the thermal profile as well as detections of molecules.

The first such spectra were observed for the HR 8799 planets, allowing for the detection of H_2O and CO as well as constraints on other planetary properties (Barman et al. 2011; Konopacky et al. 2013). Instruments like SPHERE (Beuzit et al. 2008) and GPI (Macintosh et al. 2014) have observed a number of emission spectra for directly imaged planets, in addition to interferometric observations with GRAVITY (GRAVITY

Collaboration et al. 2017). While most observations have been taken in the near infrared, JWST will allow for longer wavelength observations of these directly imaged systems. For example, Carter et al. (2023) presented the first direct detection of an exoplanet at wavelengths beyond 5 μm.

1.2.3 Observations of Isolated Brown Dwarfs

As the spectra of isolated brown dwarfs are comparatively much easier to observe than substellar companions to a host star, a wide range of observations of their thermal emission spectra exist across many wavelength ranges and spectral resolutions. The wealth of observations has led to the development of an extension to the Morgan-Keenan classification systems for stars (Keenan 1985) that consists of the L, T, and Y spectral classes (Kirkpatrick 2005; Cushing et al. 2011). Brown dwarfs cool over time, leading to the formation of condensates and molecules in their atmospheres which sculpt their emitted spectra; the emergence and disappearance of the absorption features from these species define each spectral class. Each spectral class is further subdivided into 10 subtypes typically based on the relative strength in features and tracing changes in effective temperature.

The transition from M to L dwarfs is marked by the weakening of optical absorption features from TiO and VO as titanium- and vanadium-bearing clouds condense, while absorption from H_2O and CO increases. L dwarf atmospheres are further affected by the formation of iron and silicate clouds (Allard et al. 2001; Marley et al. 2002) which redden their emergent near-infrared spectra. The transition from L to T dwarfs consists of the onset of CH_4 absorption in the near-infrared as it becomes the

major carbon-bearing molecule over CO at cooler temperatures. Clouds may also break up or sink below the photosphere at this transition, leading to bluer observed colors in the near-infrared (e.g. Marley et al. 2010), although alternative cloud-free explanations for the L/T transition have been proposed (Tremblin et al. 2016). T dwarf spectra are predominantly sculpted by H_2O and CH_4 absorption in the near-infrared. The coolest spectral class, Y dwarfs, is defined by the emergence of NH_3 absorption in the near-infrared Cushing et al. (2011).

1.3 Modeling Substellar Atmospheres

After the spectrum of an exoplanet or brown dwarf has been observed, we must turn to atmospheric modeling to interpret the data. All types of observations described in the previous section are related in some way to atmospheric properties like composition, surface gravity, and thermal structure, and models are needed to figure out the exact connection between these quantities and observational signatures. We can compare models with observations in order to constrain the values of these parameters for a given object. On a broader scale, atmospheric models can be used to both understand population level trends, like the appearance and disappearance of certain molecular features, as well as predict observable qualities for aid in planning observations. At the same time, shortcomings in their ability to reproduce observations can offer clues as to how models need to be modified, in turn indicating revisions needed to our understanding of the underlying physical and chemical processes in these atmospheres.

1.3.1 Self-Consistent Models

Self-consistent model grids offer one approach for modeling substellar atmospheres. Such grids typically assume radiative-convective equilibrium, balancing internal heat flux and any absorbed stellar flux (for objects with host stars) with outgoing fluxes carried by thermal radiative transport and convection. For a set of given parameters like effective temperature, gravity, and elemental composition, the model iterates until it converges on a 1D thermal and chemical profile of the model atmosphere which follows all assumed physical and chemical processes (see Marley & Robinson 2015 for a review for brown dwarfs and giant planets). Modeling the atmospheric structure and emitted radiation also provide an important upper boundary condition for evolution models, as the atmosphere controls how quickly the interior cools.

The thermal structure and chemical abundances of an atmosphere can then be used to simulate spectra for a variety of observational setups. Grid models can vary in complexity, often using only a small number of parameters such as surface gravity, effective temperature, metallicity, C/O, etc. For this thesis, we will focus on 1D grid models which do not take into account latitudinal or longitudinal variations. Numerous families of grid models exist, differing in the treatments of physics, chemistry, and opacity data used to generate the model spectra.

Grid models provide a way to connect our best understanding of how substellar atmospheres should function with predicted and observed spectral features, allowing for initial interpretations of observed data. However, they do not always do a good job at reproducing observations. For brown dwarfs in particular, grid models have been shown

to have difficulty reproducing observed shapes and relative colors of observed spectra (e.g. Leggett et al. 2021). The assumption of chemical equilibrium has particularly been proven false with a multitude of observations demonstrating features from species unexpected in equilibrium (Noll et al. 1997; Saumon et al. 2000; Geballe et al. 2009; Sorahana & Yamamura 2012; Miles et al. 2020). Thus, more sophisticated grid models incorporating additional processes like clouds and disequilibrium chemistry have arisen to help improve fits to observed spectra (e.g., Hubeny & Burrows 2007; Morley et al. 2012; Mukherjee et al. 2022).

1.3.2 Atmospheric Retrievals

A more data-driven alternative method is "atmospheric retrieval." Derived from remote sensing approaches in solar system science (e.g., Rodgers 2000; Fletcher et al. 2007), atmospheric retrievals have been widely-adopted in exoplanet studies (see Madhusudhan 2018 for a review) and recently applied for brown dwarfs as well (Line et al. 2015, 2017; Burningham et al. 2017). Generally, retrievals aim to make minimal assumptions about the processes at work in an atmosphere, which comes at the cost of far more free parameters. A forward model within a retrieval framework will typically involve a parameterized temperature-pressure profile and chemical abundances that can vary freely from one another, in addition to parameters like the surface gravity, radius, cloud opacity, etc. A Bayesian statistical inference algorithm such as Markov Chain Monte Carlo or nested sampling is then used to explore the full probability posterior distribution of the parameters by generating thousands of forward models and comparing them to observations. Thus, the computational efficiency of the forward

model within a retrieval framework is critical.

Through this atmospheric retrieval process, one can get estimated values for each parameter in the model as well as explore the relationship between parameters. Removing assumptions common to grid models allows for direct measurement of values like chemical abundances, free of relation to solar values and equilibrium calculations. However, while physically-motivated priors may be included in the Bayesian parameter estimation, unphysical solutions can still be produced. Furthermore, retrieval results on their own do not offer any connection to our understanding of the physics and chemistry that may produce such an atmosphere. Theoretical expectations from grid models can thus provide important context to retrieval results.

1.4 Benefits and Challenges of Increased Spectral Resolution

1.4.1 High-Resolution Cross-Correlation Spectroscopy

At increased spectral resolution, molecular features are resolved into densely-packed individual lines, as shown in Figure 1.1, that are shifted and broadened by the orbital motion and rotation of the planet. However, the signal-to-noise of each line can be quite low, especially when light is divided across many spectral bins. The combined signal of all the lines can be obtained by computing the cross-correlation function (CCF) of observations with a template model spectrum as a function of the radial velocity of the template. The CCF should have a strong peak when the template and observed spectra overlap, with the peak occurring at the line-of-sight velocity of the planet. The

strength of this detection increases with the square root of the number of observed lines, motivating the desire for instruments with both high resolving power and large spectral grasp.

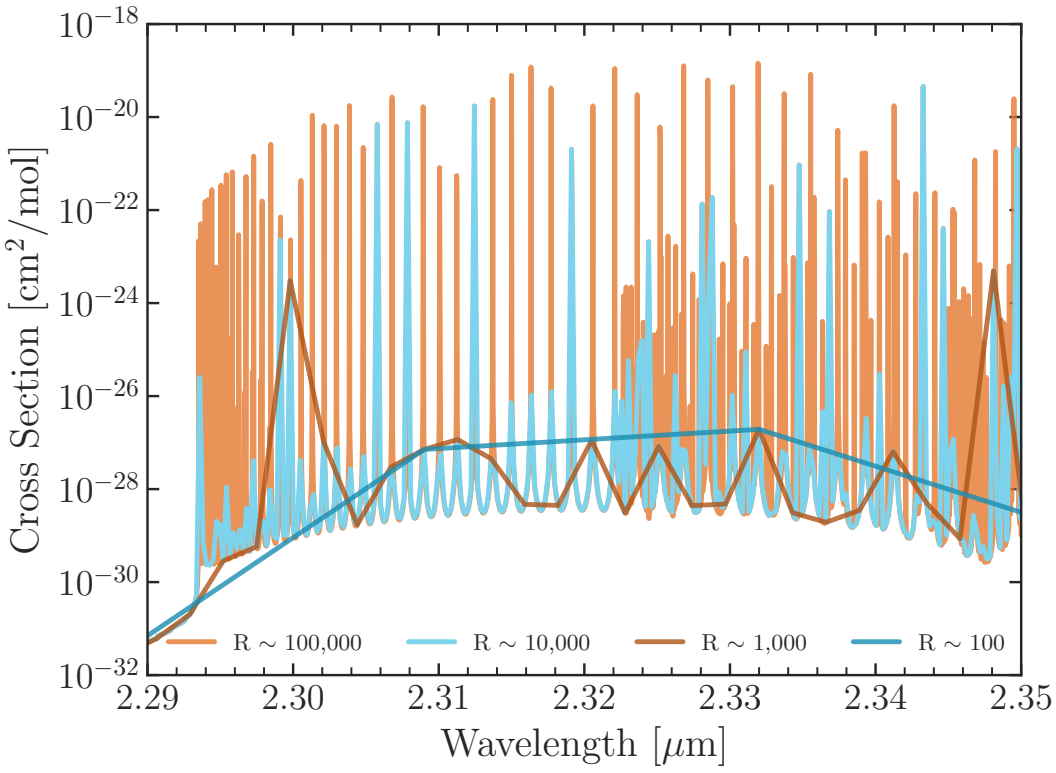

Figure 1.1: Absorption cross sections for CO at 10^{-6} bars and 650 K, sampled at resolutions from R ~ 100 - 100,000. Fewer CO absorption lines are detectable at increasingly low resolution.

The CCF technique can be used for the transmission, reflected, and emission spectra of substellar companions, which can be either close-in or widely-separated. For planets on close orbits, we can use the Doppler shift of the planet lines to separate them from quasi-static stellar or telluric contamination using detrending algorithms like SYSREM or PCA (Birkby et al. 2013; de Kok et al. 2013). However, the removal of this contamination often causes the loss of continuum information for the planetary

spectrum. For widely-separated planet or brown dwarf companions, high resolution spectroscopy can be combined with high contrast imaging to prevent contamination from the host star (Snellen et al. 2014). Even at moderate spectral resolution, Hoeijmakers et al. (2018) used integral field spectroscopy to create a 'molecule map" of β Pic b which used the strength of the cross-correlation function in each spaxel to determine the planet's location and detect its atmosphere.

Snellen et al. (2010) presented the first successful application of this technique using R$\sim$100,000 spectra from VLT/CRIRES to detect carbon monoxide in the atmosphere of the hot Jupiter HD 209458b. Numerous atomic and molecular species have been detected with CCFs since then, using observations in both the optical and near infrared (see Birkby 2018 for a review). In addition, this technique has led to molecules detected in the atmospheres of close-in, non-transiting planets, which are hard to characterize otherwise (Brogi et al. 2012; Birkby et al. 2017). Atmospheric dynamics are also measurable using the CCF, such as Doppler shifts from wind speeds or broadening from rotation (e.g., Snellen et al. 2010; Bryan et al. 2018). Furthermore, likelihood functions have been devised for these types of observations to allow for incorporation into retrieval frameworks, leading to further detailed characterization of these atmospheres (Brogi & Line 2019; Gibson et al. 2020). Recent instruments combining high-resolution spectroscopy and high-contrast imaging such as the Keck Planet Imager and Characterizer (KPIC; Delorme et al. 2021) and High-Resolution Imaging and Spectroscopy of Exoplanets at the VLT (HiRISE; Vigan et al. 2022) will further improve the scientific impact of these types of observations. Looking forward, instruments on the extremely

large telescopes may even allow for the characterization of terrestrial planets around nearby stars (Snellen et al. 2015).

1.4.2 Medium-to-High Resolution Spectra of Brown Dwarfs and Directly Imaged Companions

In contrast to exoplanets, brown dwarfs have been routinely observed at medium-to-high spectral resolution ($R \gtrapprox 2000$) for decades. However, most studies have typically focused on classifying objects or measuring radial velocities rather than in-depth atmospheric characterization, particularly early on (e.g. McLean et al. 2003, 2007; Zapatero Osorio et al. 2007; Blake et al. 2010; Burgasser et al. 2015; Marocco et al. 2015). Some brown dwarf spectral surveys focus on identifying low-gravity spectral features for a large number of objects (McGovern et al. 2004; Martin et al. 2017). Those studies which do fit their observed brown dwarf spectra to grid models often report difficulty accurately reproducing observed fluxes and widely varying results depending on choice of model and fitted wavelength region (e.g., Del Burgo et al. 2009; Patience et al. 2012; Logsdon et al. 2018). Even the most recent studies comparing medium or high resolution spectra to the most up-to-date model grids show significant discrepancies from observations for both brown dwarfs and companions straddling the brown dwarf/exoplanet boundary (Wilcomb et al. 2020; Petrus et al. 2020, 2021, 2023; Hsu et al. 2021; Hoch et al. 2022; Miles et al. 2023; Palma-Bifani et al. 2023).

Despite the mismatch between models and observations at these increased spectral resolutions, numerous insights have been gained from comparing high signal-to-noise observations to model grids. For example, Bochanski et al. (2011) report the

first detection of ammonia absorption in the near-infrared using R∼6000 spectra from the Folded-Port Infrared Echellette (FIRE) Spectrograph. Both Bochanski et al. (2011) and Canty et al. (2015) use R∼5000-6000 spectra of T dwarfs to assess the completeness and validity of line lists for important molecular absorbers available at the time. Tannock et al. (2022) (for which I am a coauthor) presents the perhaps most in-depth comparison of a high-resolution brown dwarf spectrum to grid models, focusing on IGRINS observations of a T6 dwarf at R $\sim$ 45,000 over 1.45 - 2.48 μm with S/N $\sim$ 200. Tannock et al. fit each order of data to multiple different families of model grids, showing how best fit parameters vary widely across wavelength region and model family as shown in previous brown dwarf papers. I post-processed the Sonora Bobcat models with updated line lists for H_2O,CH_4,NH_3 for this project, which greatly improved the fit to the data and yielded the most consistent parameter measurements across orders. In addition, Tannock et al. report the first unambiguous detections of molecular absorption from H_2S and H_2 in an extrasolar atmosphere, only possible with data of this quality.

Retrievals have been significantly less common than grid model fits for these observations, as most brown dwarf retrieval studies have focused on low-resolution (R $\sim$ 100) spectra. Wang et al. (2022) and Xuan et al. (2022) report results from retrieval studies of brown dwarf companions for R$\sim$ 35,000 observations from 2.03 - 2.38 μm, presenting robust constraints on properties like the metallicity and C/O ratio. Furthermore, Y. Zhang et al. (2021a) carried out a retrieval analysis of R $\sim$ 4500 observations in K band of the emission spectrum of the young super-Jupiter TYC 8998-760-1 b,

finding a well-constrained isotopologue ratio of ^{12}CO/^{13}CO in addition to other atmospheric parameters. The authors perform a similar analysis for archival R $\sim$ 25,000 K band spectra of the L5 dwarf 2MASS J03552337+1133437, again measuring the ratio of ^{12}CO/^{13}CO (Y. Zhang et al. 2021b). Other than these few exceptions, all of which focus on K band observations and mostly use restricted chemistry schemes, retrievals on medium-to-high resolution spectroscopy of brown dwarfs are relatively untested ground.

1.4.3 Modeling Considerations

As we more frequently observe brown dwarfs and exoplanets at higher spectral resolution, complementary progress in analysis methods and atmospheric modeling tools is required. Increasing the spectral resolution of our observations offers a number of advantages. Molecular band heads are resolved into unique groups of individual lines, meaning absorption from different species are easier to disentangle. Furthermore, a wider span of pressures are probed than typical at low-resolution, offering more information about the upper end of the object's temperature-pressure profile. For transmission spectra, the cores of the strongest lines may even form above a cloud or haze deck that leads to featureless spectra at low-resolution (de Kok et al. 2014; Kempton et al. 2014). Thus, high-resolution transmission spectroscopy may provide an avenue for characterizing very cloudy or hazy planets. In addition to providing comparison to observed data, model spectra of exoplanets and brown dwarfs can be used to optimize future observing programs and instrument designs to maximize the scientific potential of these observations.

However, moving to increased spectral resolution also generates challenges on

the modeling side. Resolving individual molecular absorption lines means the fidelity of the opacity data used becomes critical for accurately reproducing observations. For example, Figure 1.2 shows cross sections for CH_4 from Yurchenko & Tennyson (2014) and Hargreaves et al. (2020) at low and high spectral resolution - while the two line lists are virtually indistinguishable at low resolution, differences in line positions and strengths are clearly seen at high resolution. Tannock et al. (2022) show how best-fit parameters for brown dwarf spectra from model grids can be strongly biased by choice of line list. The cross-correlation method is also significantly affected by choice of line list, as inaccurate line positions can reduce signal strength or bias retrieved abundances (Brogi & Line 2019; Tannock et al. 2022). The greater computational challenge of producing models at high resolution also provides a barrier for applying many existing retrieval frameworks, leading to an increased reliance on methods involving grid models (Petrus et al. 2020). However, GPU-based methods offer a promising approach to speeding up retrieval studies (Zalesky et al. 2022). Additionally, better quality data also requires more careful examination of which parameterizations and assumptions can be incorporated into our models without biasing our analysis. For example, one may need to modify existing models to incorporate minor species which are undetectable for low-resolution observations or extend temperature-pressure profile parameters to lower pressures.

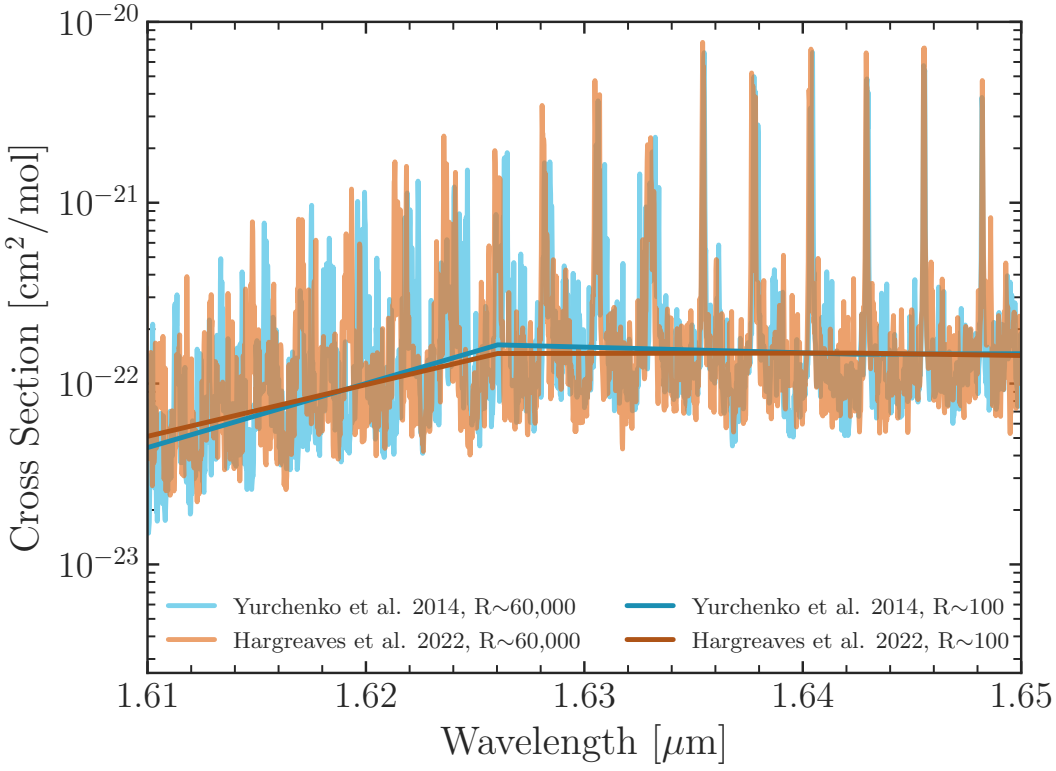

Figure 1.2: Comparison of CH_4 absorption cross sections from the ExoMol 10to10 (Yurchenko & Tennyson 2014) and HITEMP (Hargreaves et al. 2020) line lists 10^{-6} bars and 650 K, at R∼ 100 and R∼60,000. Clear discrepancies in line positions and strengths between the two lists are seen at high spectral resolution.

1.5 Structure of This Work

The aim of this thesis is to explore these modeling considerations for medium-to-high spectral resolution observations of exoplanets and brown dwarfs. In particular, I have focused on two guiding questions: 1) How do current modeling tools need to be modified to accurately reproduce these spectra? and 2) What new insight into atmospheric compositions and structures can be gleaned from these types of observations? The structure of the remainder of this thesis is as follows.

Chapter 2 considers the application of high-resolution cross-correlation spectroscopy to the haziest sub-Neptunes planets. Using theoretical grid models to simulate observed high-resolution transmission spectra of the canonical sub-Neptune GJ 1214b, I present the minimum signal-to-noise needed to detect a number of molecules such as CO and H_2O despite the aerosol opacity. I also assess these calculations in relation to what is achievable with current and future potential instruments.

Chapters 3 and 4 switch focus to retrieval studies of cool brown dwarfs. Chapter 3 focuses on a retrieval analysis of a high signal-to-noise, medium-resolution (R$\sim$6000) ground-based spectrum from 0.85-2.5 μm of the T9 dwarf UGPS J072227.51-054031.2. I present a number of modifications to the CHIMERA retrieval framework used in this work and investigate the resulting effect on our retrieved parameters. I compare these retrieval results to those for a low-resolution spectrum of the same object, demonstrating how constraints on atmospheric abundances improve by an order of magnitude or more with increased spectral resolution. Chapter 4 presents the first atmospheric retrieval analysis taking advantage of the maximum resolution of JWST's NIRSpec instrument,

using observations of the T8 dwarf 2MASS 0415-0935 with the G395H filter (R$\sim$2700 from 2.87 - 5.14 μm). In combination with previous low resolution observations, we analyze the 0.9-20 μm spectral energy distribution of this object, yielding ultra-precise ($\sim$ 0.02 dex) abundance constraints that call into question current models of disequilibrium chemistry. I also measure the ^{12}CO/^{13}CO ratio, making this object the coldest extrasolar body with such a measurement.

Finally, a summary of the findings presented in this thesis and suggested future directions are outlined in Chapter 5.

Chapter 2

Prospects for Characterizing the Haziest Sub-Neptune Exoplanets with High Resolution Spectroscopy

2.1 Introduction

NASA's *Kepler* mission has discovered thousands of exoplanet candidates with sizes between that of Earth and Neptune (Borucki et al. 2011; Batalha et al. 2013; Burke et al. 2014; Mullally et al. 2015; Rowe et al. 2015). These sub-Neptune planets appear to be common, around both M dwarf and Sun-like stars (Petigura et al. 2013; Fressin et al. 2013; Burke et al. 2015; Dressing & Charbonneau 2015). In fact, around a third of

Sun-like stars host a planet of this size with orbital periods less than 100 days (Petigura et al. 2013; Fressin et al. 2013; Burke et al. 2015).

The measured bulk density of these planets could be consistent with a range of compositions (Figueira et al. 2009; Rogers & Seager 2010; Nettelmann et al. 2011). Correspondingly, sub-Neptunes may have a diversity of compositions from rocky to gas-rich as expected from formation and evolution modelling (Fortney et al. 2013; Moses et al. 2013; Lopez & Fortney 2014). A wide range of atmospheres is expected from their bulk compositions (Morley et al. 2017; Kempton et al. 2018). The history of how a planet accreted or outgassed its atmosphere, and its subsequent evolution, may be encoded in the abundances or ratios of molecular species in its atmosphere (Öberg et al. 2011; Booth et al. 2017; Espinoza et al. 2017). Thus, constraining the atmospheric makeup of a sample of sub-Neptune planets may be the best way to understand how and out of what material these objects form. Due to their abundance, more sub-Neptune planets are likely to be found by the TESS mission around nearby, bright M-dwarfs (Ricker et al. 2015; Sullivan et al. 2015; Barclay et al. 2018), providing prime targets for atmospheric characterization with JWST, ARIEL, and large ground-based telescopes (Louie et al. 2018; Kempton et al. 2018; Zellem et al. 2019).

However, these planets have proven hard to characterize; most atmospheric features that are detected are weaker than expected for a solar-metallicity, cloud-free atmosphere (Fraine et al. 2014; Fu et al. 2017; Wakeford et al. 2017; Wakeford et al. 2019). Some measurements have been unable to detect atmospheric features at all (e.g. Knutson et al. 2014a; Kreidberg et al. 2014). Incorporating potentially muted features

into yield calculations, Crossfield & Kreidberg (2017) find that the expected yield of *TESS* planets amenable to characterization with *JWST* is up to 7x worse than when assuming cloud-free conditions.

GJ 1214b, a 6.16 ± 0.91 $M_\oplus$ and 2.71 ± 0.24 $R_\oplus$ planet around a M4.5 star (Charbonneau et al. 2009), is the prototype of this planetary class, and most dramatic example a "difficult" atmosphere. Observations of GJ 1214b taken with ground-based instruments and *HST* are consistent with a flat transmission spectrum (e.g. Bean et al. 2010, 2011; Kreidberg et al. 2014). While early observations were inconclusive, Kreidberg et al. (2014) achieved the signal-to-noise necessary to rule out just a clear but high mean molecular weight atmosphere as the source of the flat transmission spectrum. Instead, significant gray aerosol opacity has been invoked as the source of muted features in transmission spectra, including that of GJ 1214b (e.g. Crossfield et al. 2013; Kreidberg et al. 2014; Knutson et al. 2014a,b; Iyer et al. 2016; Sing et al. 2016).

Aerosols can absorb and scatter light (Heng & Demory 2013), providing an extra opacity source that dampens absorption features in transmission spectra (e.g. Deming et al. 2013; Kreidberg et al. 2014, 2018; Stevenson 2016). Morley et al. (2013) explored two types of aerosols expected to form in GJ 1214b's atmosphere—clouds from equilibrium chemistry and a photochemical haze layer from the destruction of CH_4—finding that either aerosol over a range of parameters could flatten the planet's transmission spectrum. Further cloud formation work found that KCl and ZnS clouds can only be consistent with observations at high metallicities (1000x solar) and with strong atmospheric mixing (Kzz = 10^{10} cm^2 s^{-1}) (Morley et al. 2015; Gao & Benneke

2018). In contrast, photochemical hazes could explain the observed HST observations with lower metallicities $\sim 50\times$ solar (Morley et al. 2015). If an aerosol is the cause of the observed flat transmission spectra, JWST may allow us to characterize sub-Neptunes with it's longer wavelength coverage and higher resolution than HST (Greene et al. 2016; Mai & Line 2019).

However, another potential avenue for studying these atmospheres is ground-based, high-resolution spectroscopy. Over the past decade, spectroscopy with a resolving power $\geq$ 25,000 has been used to characterize the composition, dynamics, and thermal structure of exoplanet atmospheres (see Birkby 2018 for a recent review of the technique and resulting detections). The large variations in the radial velocity of a close-in exoplanet relative to the host star allow for the Doppler-shifted planet spectrum to be disentangled from the relatively static lines of the host star's spectrum as well as from the spectral absorption features of Earth's atmosphere. At high spectral resolution, molecular band heads are resolved into unique groups of individual lines allowing for robust detections from matching these lines to theoretical models. Though first suggested by Deming et al. (2000), Brown (2001), and Sparks & Ford (2002), Snellen et al. (2010) was the first robust detection of a molecule (CO) in a planet's atmosphere using this technique with CRIRES at the VLT. Since then, molecules such as CO and H_2O have been routinely detected for a variety of planets in emission and transmission (e.g. Rodler et al. 2012; Birkby et al. 2013; Brogi et al. 2014). While most of these studies have been of hot Jupiters, a few focused on smaller planets have yielded upper limits on molecular abundances (Crossfield et al. 2011; Esteves et al. 2017; Deibert et al. 2019).

At high spectral resolution, the cores of the strongest molecular lines are formed very high up in the planet's atmosphere, possibly above whatever cloud or haze deck may obscure features at low-resolution (de Kok et al. 2014; Kempton et al. 2014). Thus, planets whose atmospheres are completely obscured in a low-resolution transmission spectrum may still be successfully characterized at high-resolution (Birkby 2018). Pino et al. (2018) showed that not only is H_2O detectable in the presence of an aerosol for a typical hot Jupiter, but the relative cross-correlation strength across multiple wavelength ranges could be used to detect the aerosol's presence.

The aim of this paper is to quantitatively study the feasibility of detecting molecular features of the haziest sub-Neptune planets with high-resolution transmission spectroscopy. Is this achievable? And specifically, is this a science case for current instruments, or only for instruments on upcoming Extremely Large Telescopes? We investigate how a range of observational parameters including signal-to-noise ratio, spectral resolution, and wavelength coverage affect the detection of various molecules.

Furthermore, as high-resolution spectroscopy has become more common, the best way to robustly report detection significances of molecules has been explored. Brogi & Line (2019) proposed a new log likelihood function to use when comparing observed spectra to a model in the place of the traditional cross-correlation function. We will compare the utility of these two metrics, motivating our choice of the log likelihood function for the majority of this work. However, this method may be affected by any "missing" molecules present in the observed atmosphere but absent in the model spectrum. For illustration, we will consider how HCN, a high abundance photochemical

product, affects the observed spectra and reported detection significances.

This work is structured as follows. In section 2, we describe how we generate transmission spectra for hazy GJ 1214b analogs and discuss how we quantify the significance of molecular detection with this technique. In Section 3, we give an overview of the prospects for observing CO, CO_2, H_2O, and CH_4 across a range of planetary insolation levels as well as the spectral resolution and wavelength coverage of the data. A discussion of our results are presented in Section 4 and our conclusions are summarized in Section 5.

2.2 Methods

2.2.1 Model Atmosphere and Spectra

We generate high-resolution transmission spectra based on the 1D radiative-convective-photochemical models presented in Morley et al. (2015). The authors assume 50× solar metallicity and use a 1D radiative-convective model to determine a temperature-pressure profile for the atmosphere assuming radiative-convective equilibrium and calculate gas abundances in different layers of the atmosphere assuming chemical equilibrium. They find the total mass of soot precursors from a photochemical model (Miller-Ricci Kempton et al. 2012; results first published in Fortney et al. 2013) at each layer and assume some percentage (f_{haze}) will form a scattering haze at that layer, with f_{haze} and the mode particle size as free parameters. The optical properties of this haze are calculated with Mie theory. For this study, we focus on a particular combination of parameters that reproduce the "flat" Kreidberg et al. (2014) observa-

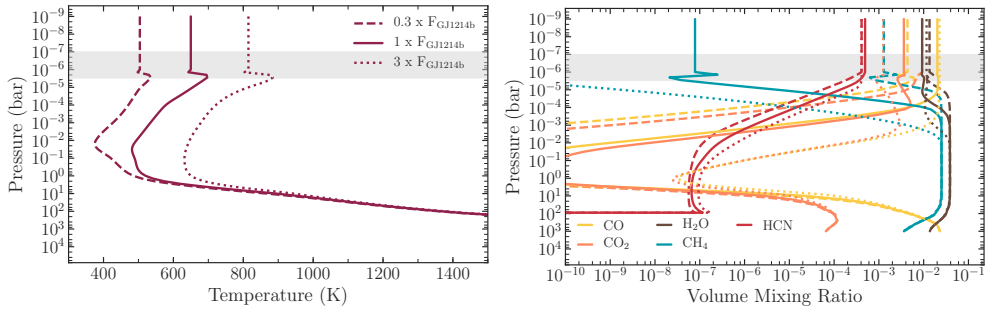

(a) (b)

Figure 2.1: Pressure-temperature profiles and molecular abundances for models with 50× solar metallicity and 0.3× (dashed), 1× (solid), and 3× (dotted) GJ 1214b's insolation. The high-resolution observations discussed in this paper are most sensitive roughly between 3×10^{-6} - 3×10^{-7} bars, marked by the light grey region in each plot.

tions at low-resolution: $f_{haze} = 10\%$ and a mode particle size of 0.1 microns. This haze becomes opaque at a pressure of approximately 10^{-5} bar in the atmosphere. We also look at models for atmospheres with 0.3× and 3× the insolation of GJ 1214 b with the same haze parameters but not the exact same haze. The atmospheres with 0.3×, 1×, and 3× the insolation of GJ 1214 b have effective temperatures of 412, 557, and 733 K, respectively (Fortney et al. 2013). The atmosphere models from Morley et al. (2015) go to 10^{-6} bars at the top of the atmosphere, but our highest resolution spectra are sensitive out to $\sim 3 \times 10^{-7}$ bars, so we assume an isothermal atmosphere above 10^{-6} bars with constant molecular abundances. The resulting pressure-temperature profiles and molecular abundances we use are shown in Figure 2.1.

To produce high-resolution transmission spectra, we use the flexible radiative transfer code described in the appendix of Morley et al. (2017). This line-by-line code takes in the temperature-pressure profiles, chemical abundance profiles, and haze opacity files from (Morley et al. 2015), as well as a mass and radius of the planet. Using the

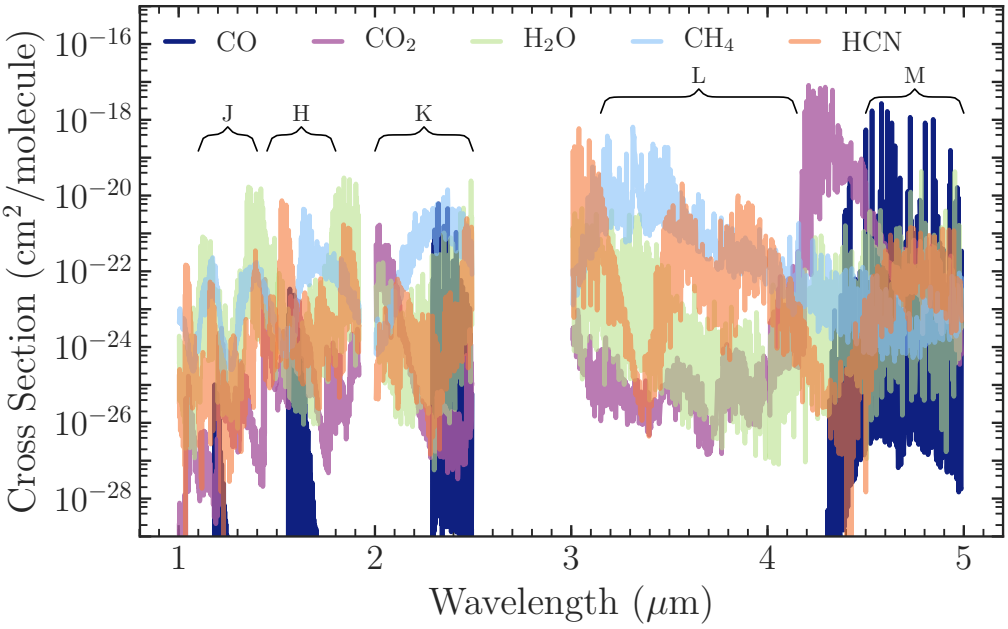

Figure 2.2: Absorption cross sections for the molecules included in our spectra. These cross sections are calculated at a pressure of 10^{-6} bars and a temperature of 650 K, then smoothed to R $\sim$ 1000 for illustrative purposes. Molecules with the strongest features in a particular bandpass, e.g. CO in M band, will be the dominant species in that wavelength range, though this effect is also dependent on the abundance of the molecule (see Figure 2.1b).

the line-by-line optical depth calculations and the vectorized method for calculating transmission spectra presented in (Robinson 2017), this code outputs high resolution line-by-line (R ~500,000) transmission spectra for the planet. We use the cross-section database described in (Freedman et al. 2014). For our calculations we include the opacities of CO (Rothman et al. 2010a), CO_2 (Huang et al. 2014, 2013), H_2O (Barber et al. 2006), CH_4 (Yurchenko & Tennyson 2014; Yurchenko et al. 2013), HCN (Harris et al. 2008), and H_2/He collision-induced absorption (Richard et al. 2012). Absorption cross sections for these molecules are shown in Figure 2.2. A molecule will be easiest to detect where it has the highest cross sections/strongest spectral features, for example H_2O in J and H bands, CH_4 in L band, and CO in M band. [1]

Example transmission spectra in K band for a range of resolutions are shown in Figure 2.3. Though the low resolution transmission spectrum shows little deviation from a flat line, resolved spectral features from CO and H_2O are visible starting with R~10,000 and increase in size as spectral resolution increases. High and low resolution spectra from 1 to 5 μm with and without the haze for all three insolation cases are shown in Figure 2.4. The haze opacity effectively obscures the molecular features below a certain pressure in the atmosphere, reducing the low resolution spectrum in particular to a mostly flat line. As the stellar insolation (and therefore the effective temperature of the atmosphere) increases, CH_4 features in L band disappear while CO shows stronger features in K and M band, in accordance with the change in abundances shown in Figure 2.1b.

[1] Although there have been updates to line lists for certain species since these publications, we do not include them in this study as we are not comparing to observations and are thus internally consistent.

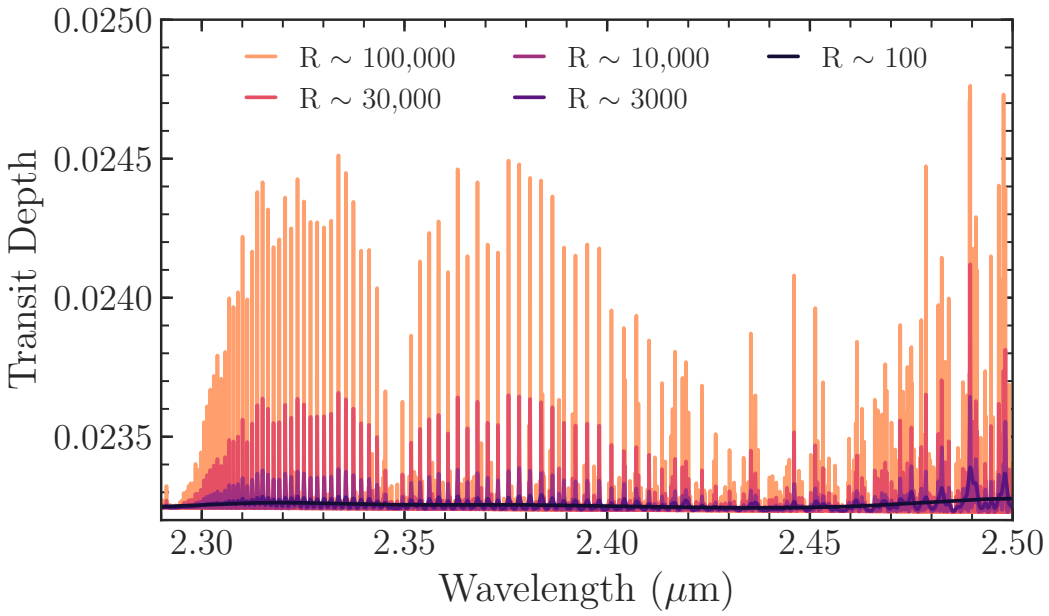

Figure 2.3: Transmission spectra for a GJ 1214b model at the nominal insolation level across a range of spectral resolutions. At low resolution, the transmission spectrum is essentially a flat line, but spectral features are clearly visible at higher resolutions.

Previous analyses of high resolution spectra have involved various methods to remove telluric and stellar contamination of the data which all require normalization of the observed spectra. To approximate an observed and reduced spectrum, we take a R ∼500,000 transmission spectrum model including all opacity sources as described above, Doppler shift it according to the systemic velocity of GJ 1214 (21 km/s), and then to reach the desired spectral resolution smooth with a Gaussian kernel and interpolate the model onto a coarser wavelength grid corresponding to the given resolution and 2 pixels per resolution element (assuming a Nyquist like sampling of 2 pixels per element). We assume telluric and stellar contamination will be dealt with completely by the data reduction process such that they are removed to the photon noise level. Consequently, we only simulate the planet's transmission spectrum, and investigate the effect of the

Figure 2.4: Clear and hazy transmission spectra for models with 0.3× (top), 1× (middle) and 3× (bottom) GJ 1214b's insolation. Both low (R $\sim$ 100) and high (R $\sim$ 100,000) resolution spectra are plotted. The presence of the haze clearly mutes molecular features, particularly in the low resolution spectra. Furthermore, at high resolution the difference between the coolest and hottest models is most pronounced; this difference can be attributed to the larger scale height for the hotter model in addition to differences in abundances.

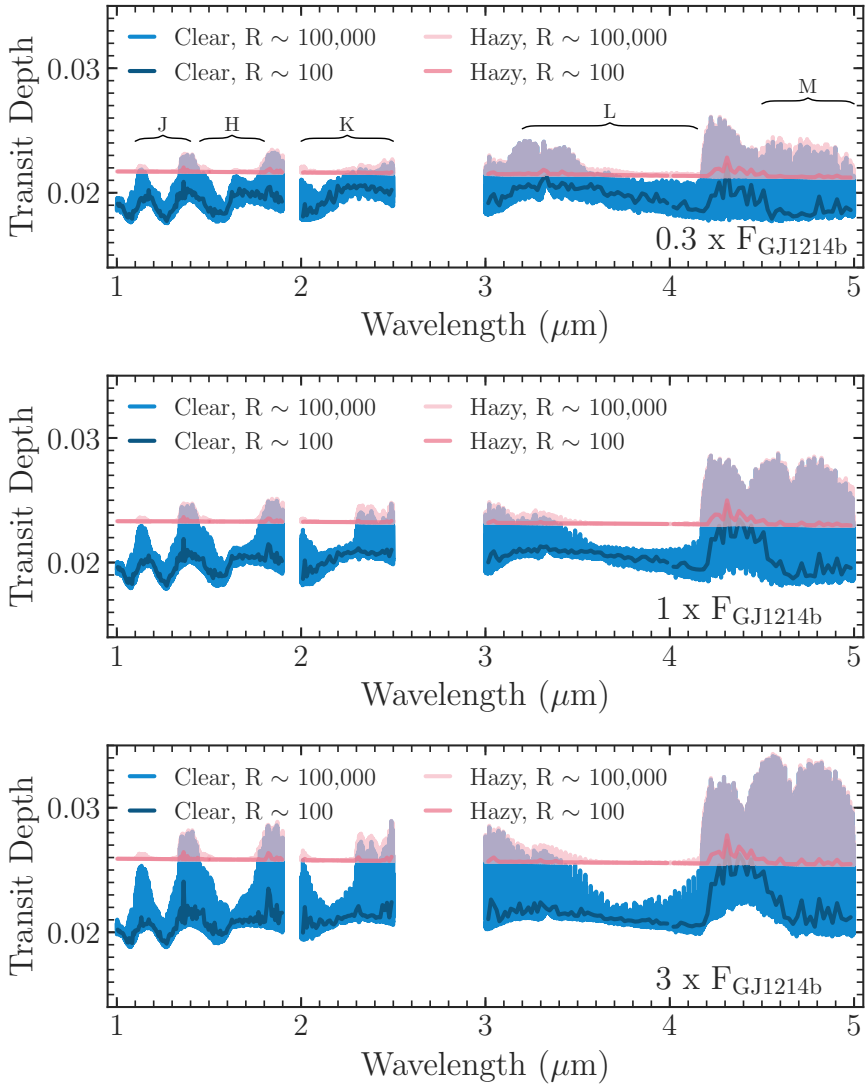

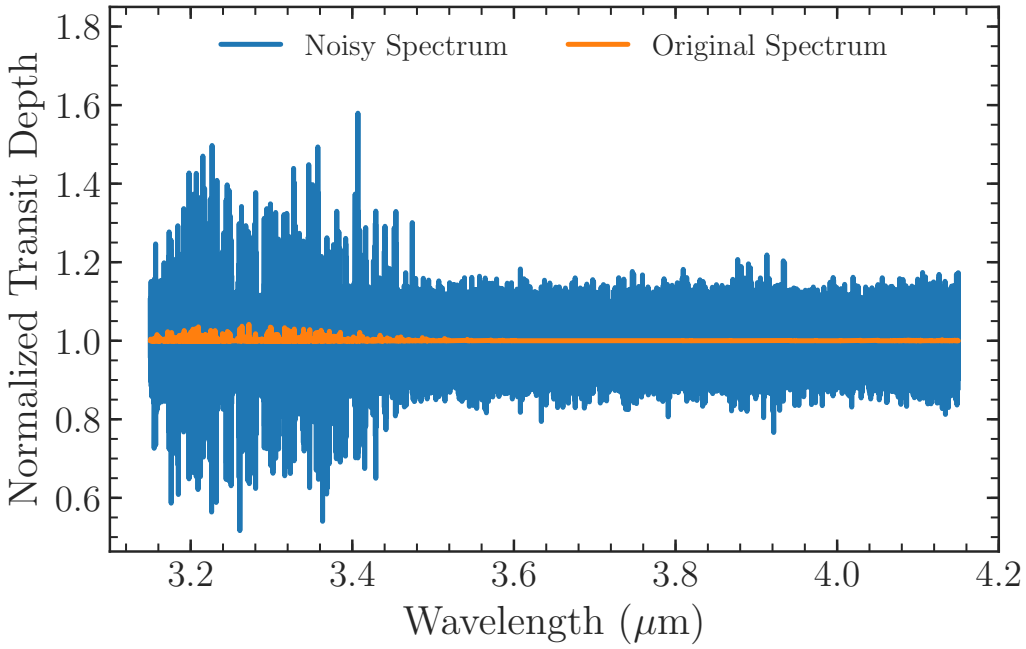

Figure 2.5: Normalized transmission spectra with R $\sim$ 100,000 for a GJ 1214b model before and after the addition of noise. The random noise added to the spectrum has a base S/N$_{res}$ of 1000 (or 1000 ppm of noise), scaled by a model of the Earth's transmission spectrum.

photon noise. While we do not assume a full noise simulator and data processing steps (e.g. Brogi & Line 2019), we approximate the final outcome of such an approach by doing the following. First, to determine the amount of random noise to add to each pixel in our "truth" spectrum, we choose a particular signal-to-noise ratio on what would have been observed in the stellar spectrum per resolution element (S/N_{res}) as in Pino et al. (2018). For the signal-to-noise per pixel, $S/N_{pix}(\lambda)$ we multiply this S/N_{res} by the square root of the telluric absorption spectrum $T(\lambda)$ (which has values between 0 and 1), to mimic the reduction in S/N due to telluric extinction, and the square root of the number of pixels per resolution element. We simulate noise by adding a noise value to each pixel drawn from a Gaussian distribution with a standard deviation equal to the reciprocal of the desired signal-to-noise per pixel. Given that we are assuming photon noise, which follows a Poisson distribution, Gaussian distributed noise is an appropriate approximation for the high stellar photon counts. We obtain $T(\lambda)$ using the ESO Skycalc tool based on the Cerro Paranal Sky Model (Noll et al. 2012; Jones et al. 2013). An example of the normalized transmission spectrum in L band before and after the addition of noise is shown in Figure 2.5. Both the original GJ 1214b transmission spectrum and that of Earth's atmosphere have stronger features on the bluer end of L band, reflected in the noisier but more prominent features on the shorter wavelength end of the noisy spectrum.

2.2.2 Quantifying Detection Significance

High-resolution spectra of exoplanet atmospheres are often "self-calibrated" rather than in comparison to a standard star, meaning broadband information and

changes in flux at a fixed wavelength over time are removed from the data by fitting a trend with airmass or using a principal component analysis based approach (e.g. Snellen et al. 2010; Birkby et al. 2013). These data processing steps to remove the telluric contamination typically remove any reliable planetary continuum level information. This makes typical data-model "chi-square" comparisons difficult, if not impossible, unless the exact stretching/scaling to the data is known. In light of this, the standard approach is to utilize the cross-correlation function (CCF), which leverages information in individual line ratios to determine planetary atmosphere information (see Brogi & Line 2019 and Gibson et al. 2020 for a detailed discussion). The cross-correlation function determines the correlation between the data and a model template as a function of Doppler shift. A model perfectly matched to the data will show a "peak", or maximum correlation, at the planetary velocity (in our case, the systemic velocity). Incorrect models will show no peak or a damped peak relative to the "correct" model. Following the notation of Brogi & Line (2019), we define the variance of the data (s_f^2), the variance of the model (s_g^2), and the cross-covariance R(s) as follows:

$$s_f^2 = \frac{1}{N}\sum_n f^2(n)$$

$$s_g^2 = \frac{1}{N}\sum_n g^2(n-s)$$

$$R(s) = \frac{1}{N}\sum_n f(n)g(n-s)$$

where n is the bin number or spectral channel, s is a bin/wavelength shift, N is the total number of spectral channels, f(n) is an observed spectrum, and g(n) is a model

spectrum for comparison, both mean-subtracted.

The cross-correlation coefficient C(s) is then:

$$C(s) = \frac{R(s)}{\sqrt{s_f^2 s_g^2}} \tag{2.1}$$

In the literature, molecules have been detected by reporting a strong signal in the cross-correlation function of observed spectra with a model that contains solely the molecule of interest. When using the CCF, we compare to models that have only one or two opacity sources at a time, e.g. just CO or CO and the haze opacity. The strength of this detection has often been reported as the ratio of the peak of the CCF and the standard deviation of the coefficient around the peak (e.g. Snellen et al. 2010) though some more sophisticated approaches have also been used like the Welch T-test metric (e.g. Birkby et al. 2013). Hawker et al. (2018) find the ratio of peak to standard deviation to be the most conservative metric for evaluating detection significance, so this is how we will report detection significances from a CCF in this work. However, this peak-to-off-peak comparison only determines the S/N within a given model template relative to the on-to-off velocities, making quantitative comparisons amongst differing model templates challenging.

Brogi & Line (2019) proposed a solution to this problem by developing a mapping of the CCF to a log-likelihood function (log(L)) for use in a Bayesian retrieval framework. Using the above definitions, they related a formal log-likelihood to the CCF

(or rather, the cross-covariance) through:

$$\log(\mathrm{L}) = -\frac{N}{2}\log(s_f^2 - 2R(s) + s_g^2) \tag{2.2}$$

where as defined above N is the total number of spectral channels, s_f^2 is the variance of the data, s_g^2 is the variance of the model, and R(s) is the cross-covariance of the data and a model with some wavelength shift s. Before proceeding with our atmospheric analysis, we first investigate the sensitivity of the model comparisons under the CCF and log(L) assumptions. Since we are not performing a retrieval analysis but instead comparing to forward models, we need a method of mapping the log(L) value to a detection significance analogous to that obtained with the CCF. To do this, we first calculate $\log(L_1)$ for our "truth" spectrum (e.g., the same underlying model used to generate the simulated data, which again, includes the haze continuum and all of the gases). We then compute $\log(L_2)$ for 5 additional nested models that each lack one of our tested opacity sources, so we can isolate how much that missing opacity source decreases the log(L). To quantify the detection of each source of opacity, we utilize the change in Bayesian Information Criterion (BIC) (Schwarz 1978):

$$\mathrm{BIC} = p\log N - 2\log L \tag{2.3}$$

between the full model and the subset model lacking that opacity source, of which we then approximate $\Delta_{BIC} \approx 2 * (\log L_1 - \log L_2)$.[2]. We then relate this change in BIC

[2]Effectively, this becomes a likelihood ratio test to compare models as we are not changing the number of free parameters (p in Equation 2.3). The molecule we remove is not a free parameter as we do not vary its value to fit the data.

to the Bayes factor, using the formula $\Delta_{BIC} = 2 * \log B_{12}$ (e.g. Szydłowski et al. 2015). We can then map this Bayes factor to a frequentist p-value using Table 2 from Trotta (2008), which can in turn be converted into a statistical significance. Due to the limited nature of the table, we are only able to report signficances smaller than 21.3σ; anything that would have a stronger significance is reported as this upper limit.

2.2.3 CCF vs. Log(L) Example: CO in *K* Band

Here we compare molecular detections from the CCF and log(L) approaches as a function of the signal-to-noise per resolution element S/N_{res} for a representative K-band (2-2.5 μm) spectrum of our nominal GJ 1214b model.

First, we look at a single truth spectrum with S/N_{res} of 1000 and R$\sim$100,000, assuming a velocity of 0 km/s for the planet. Figure 2.6 shows the CCFs of this spectrum with models that contain either all opacity sources, just CO and the haze, or just CO; the statistical significances of each peak are 9.9σ, 9.7σ, and 9.1σ, respectively [3]. As expected, the template that contains all of the opacity sources included in the original model gives the highest peak CCF, relative to the off-peak velocity baseline. The template that contains both CO and the haze has a slightly smaller peak, which again decreases when the haze opacity is ignored. However, these decreases are relatively small, suggesting the CCF is not particularly sensitive to the presence of a haze.

Figure 2.7 similarly shows the log(L) as a function of velocity for templates that include all opacities, all but CO, and all but the haze. Figure 2.7a is zoomed in to

[3] Typically in the literature this metric is referred to as the S/N of a detection and lacks the sigma symbol (unlike significance values from the Welch T-test metric for example). However, we will include the sigma in this work to aid in comparison to detection significances derived from the log(L) method.

show how the peak seen when computing log(L) for the full model disappears when CO is removed, highlighting the necessity of CO to properly match the original spectrum. The decrease in log(L) at the planet velocity (0 km/s) corresponds to a 10.9 σ detection of CO (based on Eqn. 2.3 and subsequent discussion). We note that the log(L) for the model without CO has a higher average value than the model with CO; we attribute this effect to the decreased variance (s_g) of the model without the prominent CO lines, which increases the resulting log(L) as seen in Equation 2.2. Thus, a clear peak in the log(L) as a function of velocity should be taken as an indication that a model that correctly matches the truth spectrum rather than just the average value. We assume a retrieval method would identify the correct velocities and so only consider the value at 0 km/s as this is most analogous to what a retrieval detection significance would be. Figure 2.7b shows the same curves, as well as log(L) with a template not containing the haze. When the haze opacity is removed, though the peak in log(L) at 0 km/s is still prominent, log(L) significantly decreases at this velocity, corresponding to a $> 20\sigma$ detection of the haze. Therefore, the haze is also necessary in addition to CO to match the truth spectrum. However, if one did not test the models containing the haze opacity, they may still detect CO since the Log(L) still shows a peak at 0 km/s but assume the atmosphere was clear. Models including a potential source of continuum opacity should be investigated to maximize the atmospheric information one can learn from the data.

Next we explore the differences in detection from the CCF vs. log(L) approach over a small grid of S/N$_{res}$ and resolutions, summarized in Figures 2.8 and 2.9. In order to account for the effect of random noise, we repeat the analysis for 25 different

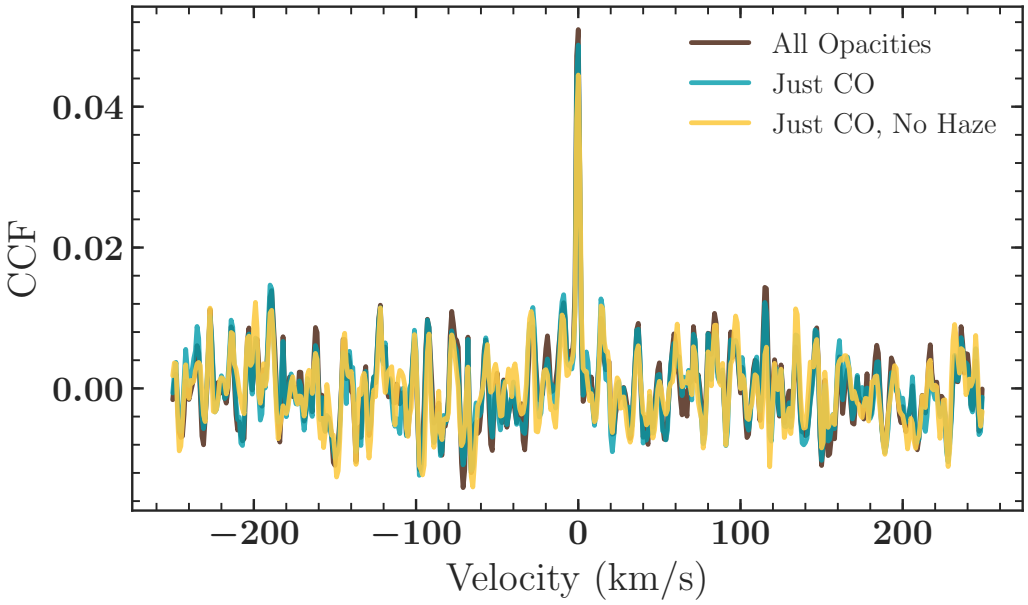

Figure 2.6: CCFs of transmission spectra models including varying opacity sources with a spectrum that includes all opacities and has random noise added to give it a S/N per resolution element of 1000.

noise instances and report the average and standard deviation of the resulting detection strengths. Comparing Figures 2.8a and 2.8b, we see that removing the haze opacity does typically slightly lower the average detection strength of CO when using the CCF regardless of spectral resolution or S/N_{res}. However, within their uncertainties, the detection strengths of CO agree between templates that include or ignore the haze opacity. Figures 2.9a and 2.9b show the detection strengths for CO and haze, respectively, when using the log(L) method. We see that 2.9a resembles 2.8a and 2.8b, meaning that the CCF and log(L) give similar detection strengths for CO. Figure 2.9b shows we can strongly detect the presence of a haze, even when we cannot robustly detect CO (for example, with R$\sim$ 25,000).

Overall, we find that CCF and log(L) give similar answers for molecular detec-

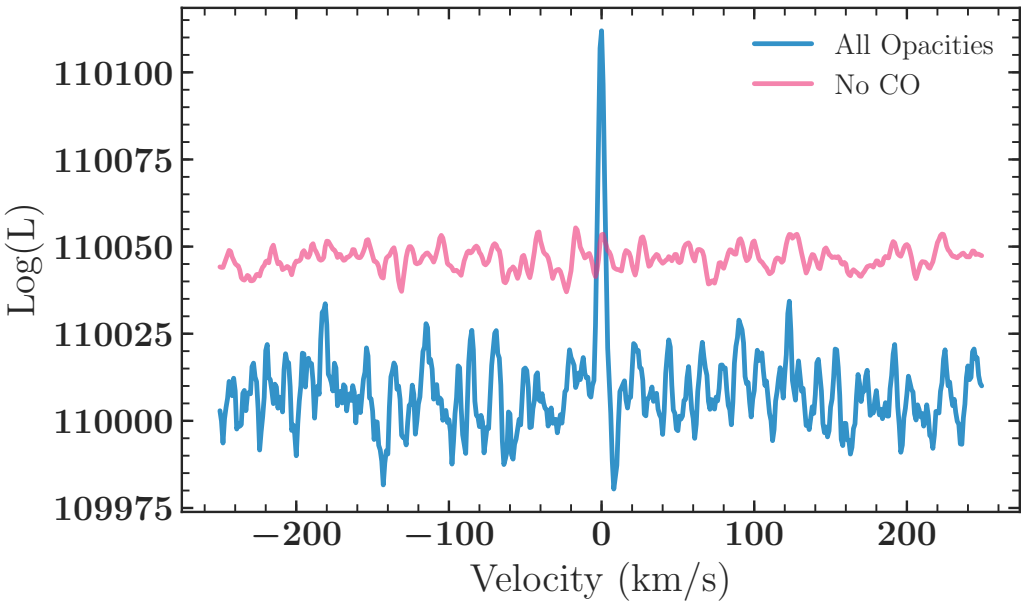

(a)

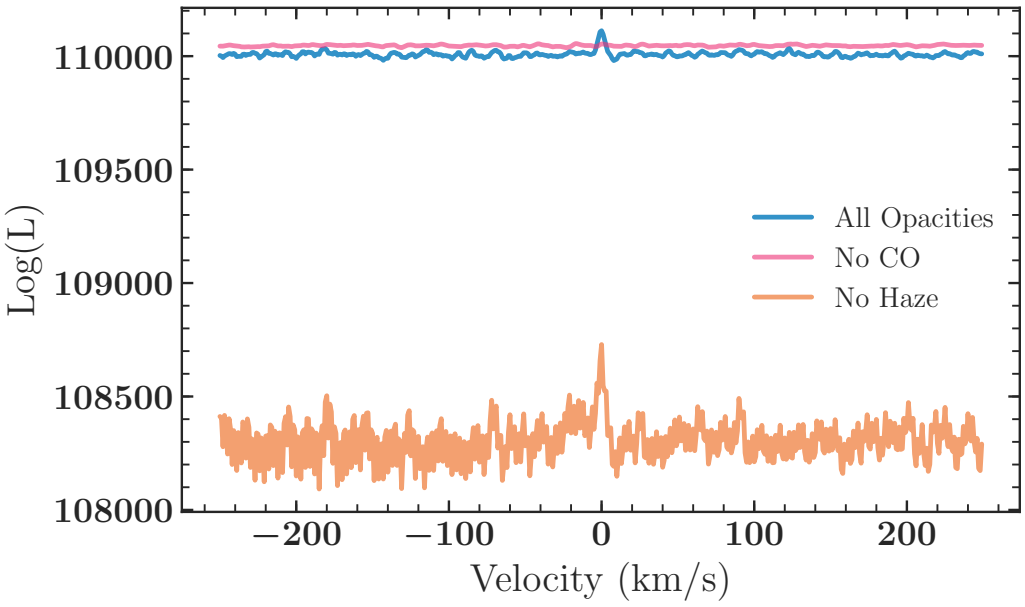

(b)

Figure 2.7: Log(L) for transmission spectrum models that include varying opacity sources with a spectrum that includes all opacities and has random noise added to give it a S/N per resolution element of 1000. In 2.7a, we see that the peak in log(L) seen at zero relative velocity disappears when CO is removed from the model. In 2.7b, we see the value of log(L) drastically decreases when the haze opacity is removed from the model.

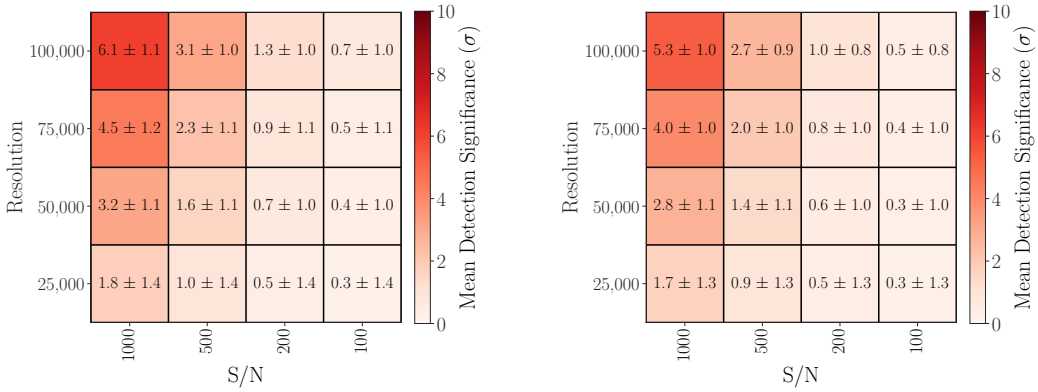

(a) CCF: CO and Haze

(b) CCF: Just CO

Figure 2.8: Detection significance in sigma for CO as a function of spectral resolution and S/N per resolution element of the transmission spectrum of nominal GJ 1214b model (1× insolation). In 2.8a, we have cross-correlated our input spectra with models including opacity only from CO and a haze. In 2.8b, we have removed the haze opacity from the model we use for cross-correlation; the detection significances agree with those obtained when including the haze opacity, making it difficult to robustly identify the presence of a haze when using the CCF.

tions, but the log(L) method is much more sensitive to the presence of a haze opacity. This suggests the high-resolution spectrum is sensitive to the broadband opacity of the haze due to the loss of a myriad of weaker lines. The increased sensitivity of the log(L) is attributable to the treatment of the model and data variance terms (s_f and s_g). As noted in Brogi & Line (2019), the log(L) decreases when s_f and s_g differ significantly, while the CCF is not clearly affected by this discrepancy. The presence of a haze opacity will serve to mute any molecular features (as seen in Figure 2.4), effectively decreasing the variance of the spectrum. As a result, a model that includes the haze will have a more similar variance to the observed spectrum of a hazy object, leading to a detectable change in log(L). Thus, for the remainder of this paper, we will only use the log(L) method to quantify how well we can detect opacity sources.

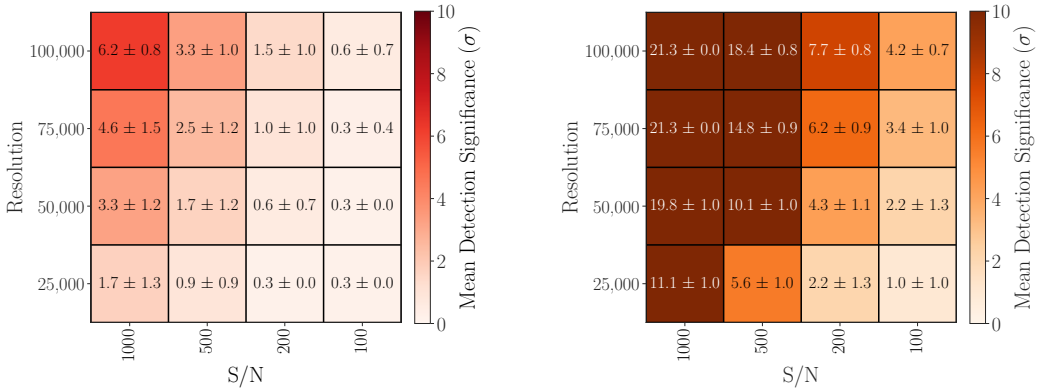

(a) Log(L): CO

(b) Log(L): Haze

Figure 2.9: Detection significances in sigma for CO and a haze as a function of spectral resolution and S/N per resolution element of the transmission spectrum of nominal GJ 1214b model (1× insolation). The detection strengths reported in 2.9a are very similar to those found when detecting CO with the CCF as shown in 2.8a. However, as this method allows us to probe the presence of a haze directly, we can much more confidently report the detection of a haze using the log(L) as shown in 2.9b.

2.3 Results

Here we present the detectability given the above metrics for CO, CO_2, H_2O, CH_4, and a haze opacity as a function of spectral band, resolution, and S/N_{res}. The "truth" spectrum is generated by including all of the above opacity sources as well as H_2/He collision-induced absorption from one of three input pressure-temperature profiles, corresponding to 0.3×, 1×, or 3× GJ 1214 b's stellar insolation (Figure 2.1). The observing bands we consider and their corresponding wavelengths are shown in Table 2.3. These bandpasses are a bit wider than are typically defined for ground based observations as at high resolution telluric absorption features can possibly be resolved with usable data in between, and instruments can have varying wavelength coverage. We test a large range of S/N_{res} from 50 to 5000, averaging the detectability over 25 random

Table 2.1: Observing bands considered in this study.

Observing Band	Wavelength Coverage (microns)
J	1.1 - 1.4
H	1.45 - 1.8
K	2.0 - 2.5
L	3.2 - 4.15
M	4.4 - 5.0

noise instances (as in Section 2.2.3). We then find the average detection strength from these 25 noise instances. Tables 2.3 - 2.3 report the lowest S/N_{res} required for detecting (threshold for detection set at 5σ) a given opacity source (one table per source) as a function of observing band, insolation (relative to that of GJ 1214b), and spectral resolution. We will go into a more detailed overview of these results in the following sections.

2.3.1 1× GJ 1214b Insolation

Three findings are consistently true regardless of wavelength range considered. First, as indicated in Table 2.3, the haze is always the easiest opacity source to detect since it has the lowest required S/N_{res} for detection, which is 500 or less in all cases considered. Thus, if one achieved the S/N_{res} necessary to detect a molecule like CO in the atmosphere of one of these planets, one would necessarily have the required S/N_{res} to rule out a completely clear atmosphere as well. Again, this is made possible through the s_g and s_f terms in the log-likelihood function and would thus be difficult if not impossible to detect using the classic CCF approach.

Second, increasing the spectral resolution appears to have diminishing returns,

Table 2.2: Minimum S/N_{res} required for $\geq 5\sigma$ detection of the haze.

Observing Band	Insolation	Spectral Resolution			
		25,000	50,000	75,000	100,000
	0.3×	400	250	200	150
J	1×	350	200	150	150
	3×	200	150	100	100
	0.3×	350	200	150	150
H	1×	350	200	150	100
	3×	200	100	100	100
	0.3×	400	250	200	150
K	1×	450	250	200	150
	3×	300	150	100	100
	0.3×	300	200	150	100
L	1×	400	250	200	150
	3×	300	200	150	100
	0.3×	350	200	150	150
M	1×	250	150	100	100
	3×	200	150	100	100

Table 2.3: Minimum S/N_{res} required for $\geq 5\sigma$ detection of CO. There are no $\geq 5\sigma$ detections with $S/N_{res} \leq 5000$ for *J*, *H*, and *L* bands.

Observing Band	Insolation	Spectral Resolution			
		25,000	50,000	75,000	100,000
	0.3×	-	4500	3500	2400
K	1×	3500	1600	1100	800
	3×	1800	1000	700	500
	0.3×	1400	800	600	400
M	1×	700	400	250	200
	3×	400	250	150	150

Table 2.4: Minimum S/N_{res} required for $\geq 5\sigma$ detection of CO_2. There are no $\geq 5\sigma$ detections with $S/N_{res} \leq 5000$ for J, H, K, and L bands.

Observing Band	Insolation	Spectral Resolution			
		25,000	50,000	75,000	100,000
M	0.3×	4500	2400	1800	1300
	1×	4500	2400	1700	1300
	3×	4500	2200	1500	1100

Table 2.5: Minimum S/N_{res} required for $\geq 5\sigma$ detection of H_2O.

Observing Band	Insolation	Spectral Resolution			
		25,000	50,000	75,000	100,000
J	0.3×	-	2600	1900	1200
	1×	-	2800	2200	1300
	3×	3000	1600	1200	700
H	0.3×	-	4500	3000	2200
	1×	-	4000	2800	2000
	3×	3500	1800	1200	900
K	0.3×	-	-	4000	3000
	1×	-	-	4000	3000
	3×	5000	2800	1900	1500
L	0.3×	-	4500	3500	2600
	1×	-	4000	3000	2600
	3×	3000	1500	1300	1100
M	0.3×	5000	2800	1900	1300
	1×	4000	2400	1600	1200
	3×	1800	1000	700	500

Table 2.6: Minimum S/N_{res} required for $\geq 5\sigma$ detection of CH_4. There are no $\geq 5\sigma$ detections with $S/N_{res} \leq 5000$ for J, H, and M bands.

Observing Band	Insolation	Spectral Resolution			
		25,000	50,000	75,000	100,000
K	0.3×	-	3000	2000	1600
	1×	-	-	-	-
	3×	-	-	-	-
L	0.3×	1100	700	450	300
	1×	-	-	-	-
	3×	-	-	-	-

i.e. increasing the spectral resolution from R $\sim$ 25,000 to 50,000 yields the greatest decrease in the required S/N_{res} (often a factor of 2) but increasing the spectral resolution further does not yield quite as dramatic of a change in the required S/N level. This is because once enough strong spectral lines are resolved to clearly identify the presence of a molecule, adding additional weaker lines from further increased spectral resolution is an increasingly marginal help. However, increasing to higher spectral resolution may still lead important gains in precision on parameters beyond detection of molecules, such as molecular abundances, temperature structure, or wind speeds that we do not consider in this work.

Lastly, CH_4 is undetectable across all wavelength ranges and spectral resolutions for models with this insolation level. This inability to detect CH_4 is expected due to the lack of CH_4 above $\sim 10^{-4}$ bar (where these observations are most sensitive) as shown in Figure 2.1b.

More specifically, here we break-down the band-by-band results:

Figure 2.10: Detection significances for different opacity sources as function of spectral resolution and S/N_{res} for M band transmission spectra of the model with $1\times$ GJ 1214b's insolation. All tested opacity sources except CH_4 are detectable in M band, though the haze and CO are detectable for a much wider range of combinations of S/N_{res} and spectral resolution than CO_2 and H_2O.

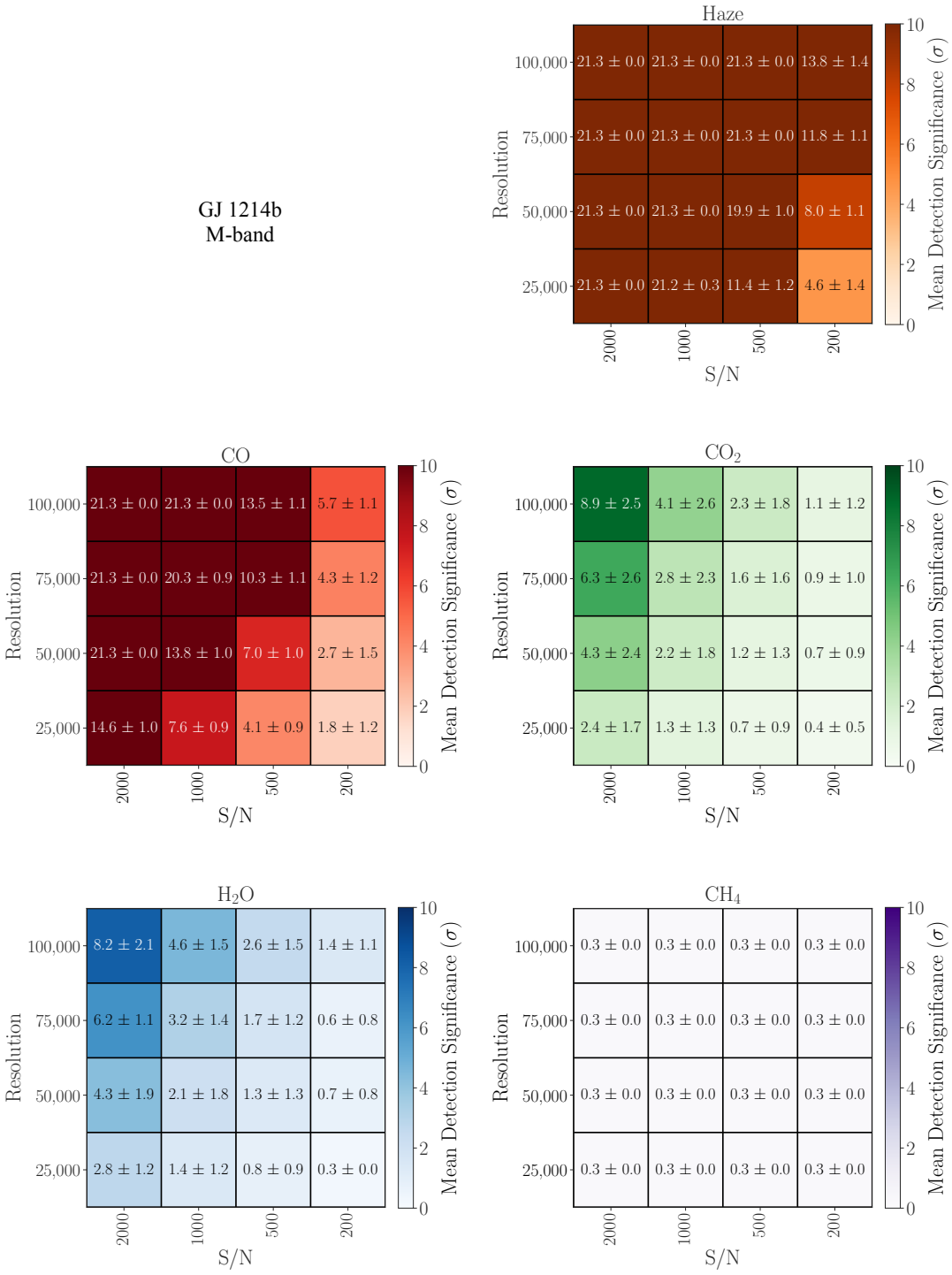

- J and H Bands: H_2O is the only molecular opacity source detectable in addition to the haze. The required S/N_{res} for detecting H_2O is lower in J band than in H - 2800 and 4000, respectively, for R $\sim$ 50,000.

- K Band: CO is detectable for all spectral resolutions, while H_2O is detectable for R $\geq$ 75,000. However, H_2O requires much higher S/N spectra. For example, at a R $\sim$ 75,000, one needs an effective S/N_{res} of 1100 to detect CO but 4000 for H_2O.

- L Band: H_2O is again the only detectable molecule. A higher S/N_{res} is required to detect H_2O compared to J or H, with a required value of 4000 for R $\sim$ 50,000.

- M Band: CO, CO_2, and H_2O are all potentially detectable. Plots of the detection strength for all considered opacities as a function of selected spectral resolutions and S/Ns are shown in Figure 2.10. Detecting CO is significantly easier than in K; at a R $\sim$ 75,000, one only needs an effective S/N_{res} of 250 to detect CO. In addition, CO_2 is only detectable in this wavelength range, though it does require a higher S/N_{res} than that needed to detect CO (for example, 1700 at a R $\sim$ 75,000). H_2O requires comparable S/N_{res} to CO_2, but with spectra at R$\sim$100,000, one could detect CO, CO_2, and H_2O with $S/N_{res} \geq 1100$. Thus, the M band is overall the most promising observing band for detecting 2 or more molecular opacity sources at once. However, the high thermal background in M band may make these observations more challenging as discussed in Section 2.4.1.

In general, the bands in which different molecules are detectable is our work here do reflect previous observational results. H_2O has been detected in J band (Alonso-

Floriano et al. 2019), K band (e.g. Hawker et al. 2018), L band (e.g. Birkby et al. 2013, 2017; Piskorz et al. 2018), and data covering 0.95 - 2.45 μm simultaneously (Brogi et al. 2018; Guilluy et al. 2019). CO has been repeatedly detected in K band (e.g. Snellen et al. 2010; Flagg et al. 2019). To date, no molecules have been reported for high-resolution ground-based M band spectra of an exoplanet atmosphere.

de Kok et al. (2014) investigated the optimal wavelength ranges to detect different molecules in exoplanet atmospheres with the 2014-era CRIRES instrument on the VLT. Similar to our results presented above, they also find that CO is best detected in K and M bands, while H_2O is detectable in J - M bands. However, they find the region around 3.5 μm as optimal for detecting multiple species (CO_2, CH_4, and H_2O), in contrast to our preference for M band. As we will discuss later in Section 2.4.1, the thermal background in M band can make it functionally difficult to reach the required S/N_{res} with current instruments. In addition, they assume a truth spectrum with only one molecule at a time and cross-correlate with a model of just that species; they note that CH_4 or H_2O lines could have a shielding effect that make other molecules more difficult to detect. Thus, our inability to also detect CO_2 in L band can be attributed to the higher cross sections of the many lines of CH_4 and H_2O in this region as shown in Figure 2.2.

2.3.2 0.3× and 3× Insolation

Since we would like to be able to observe a wider range of planets than just GJ 1214b, we also investigate how changing the stellar insolation effects our results, looking at models with 0.3× and 3× the true insolation of GJ 1214b. The primary effect is the

change over of the dominant carbon bearing species with temperature: CH_4 dominating in the 0.3× case and CO/CO_2 in the 3× scenario, with an overlap/transition for the 1× case (Figure 2.1b).

0.3× Insolation

As above, we list our results by observing band, but to simplify the discussion, only summarize the differences from the 1× insolation case. In some cases the haze opacity requires a slightly higher S/N_{res} to detect than the nominal insolation case, but it still remains the easiest opacity source to detect across all wavelength bands and resolutions. Overall, the decrease in temperature for the models with 0.3× GJ 1214 b's insolation makes CO, CO_2, and H_2O slightly harder to detect, while these are the only models where CH_4 is detectable. Though the volume mixing ratio of H_2O is actually slightly higher in the cooler case than that of the nominal insolation, this increase in difficulty may be attributed to the decrease in scale height with decreasing temperature which makes spectral features smaller. However, interference from the many CH_4 lines may also make H_2O harder to detect. To test this idea, we took a 0.3× insolation model in L band (which has the strongest CH_4 features) without CH_4 but including all of our other opacity sources as the "truth" model and computed the required S/N_{res} to detect H_2O in this case. When CH_4 lines are not included, the required S/N_{res} to detect H_2O decreases for all tested spectral resolutions, indicating that interference from CH_4 is indeed a source of the increased difficulty in detecting H_2O for these cooler models.

- J and H Bands: The required S/N_{res} for detecting H_2O is slightly lower in J

band and higher in H band when compared to the 1× results. For example, with R∼ 50,000 spectra, detecting H_2O would require $S/N_{res} \geq 2600$ in J band and $S/N_{res} \geq 4500$ in H band, compared to 2800 and 4000 for the 1× insolation case, respectively.

- K Band: Detecting CO requires a much higher S/N_{res} due to its decreased abundance, and is not detectable at R≤25,000 for any of our noise scenarios. CH_4, which is not detectable in the nominal 1× models, is more readily detectable than CO and H2O in this cooler scenario (i.e. with $S/N_{res} \geq$2000 at R∼75,000, compared to 3500 for CO and 4000 for H_2O). For the highest resolution case (R ∼ 100,000), one could detect CO, H_2O, and CH_4 with a $S/N_{res} \geq 3000$.

- L Band: CH_4 and H_2O are both detectable. Due to the proximity to the v3 band, detecting CH_4 requires a much lower S/N_{res} than in K, with a lower limit of 300 in the R∼100,000 case. A slightly higher S/N_{res} is required to detect H_2O than in the 1× insolation case; $S/N_{res} \geq 3500$ rather than 3000 for R∼75,000.

- M Band: In all cases the required S/N_{res} to detect CO, CO_2, and H_2O is higher than for the nominal models. For R∼ 100,000, CO, CO_2, and H_2O require $S/N_{res} \geq 400$, 1300, and 1300, respectively (compared to 200, 1300, and 1200 for the 1× insolation case).

3× Insolation

The hotter 3× insolation models show qualitatively similar detection behaviour to the 1× case. In most cases the haze opacity requires a slightly lower S/N_{res} to detect

than the nominal insolation case, but the change is often small. The biggest difference is that CO, CO_2 and H_2O are all easier to detect, sometimes by up to a factor of 2 decrease in the required S/N_{res}.

- *J* and *H* Bands: The required S/N_{res} for detecting H_2O is approximately 2× lower than in the 1× insolation case for all resolutions in both bands, likely due to the increase in the size of the features in these bands compared to the nominal insolation case as seen in Figure 2.4.

- *K* Band: Both CO and H_2O are detectable, but again require lower S/N_{res} for a 5σ detection. This decrease in required S/N_{res} is $\sim$ 40% for CO, while closer to $\sim$ 50% for H_2O. Notably, in this hotter scenario, H_2O is detected at R$\leq$50,000 for all explored S/N cases, in contrast to the nominal 1× insolation case where it is only detectable at higher resolutions.

- *L* Band: The required S/N_{res} for H_2O detection is again roughly 50% lower than needed in the 1× insolation case across spectral resolutions.

- *M* Band: The required S/N_{res} to detect CO, CO_2, and H_2O is lower than in the nominal insolation case, with the largest effect for H_2O. With spectra at R$\sim$100,000, one could detect CO, CO_2, and H_2O simultaneously with $S/N_{res} \geq$ 1100 (compared to 1300 in the 1× insolation case).

2.3.3 Observing Multiple Bands

Modern instruments are now able to observe multiple atmospheric windows simultaneously, often some selection of *J*, *H*, and *K* bands, including CARMENES

(Quirrenbach et al. 2016), NIRPS (Wildi et al. 2017), IGRINS (Park et al. 2014), GIANO (Origlia et al. 2014), and SPIRou (Artigau et al. 2014). Access to multiple bands in one exposure allows for more spectral lines of a molecule to be observed, strengthening the signal of that molecule, as the molecular detection S/N scales as the $\sqrt{N_{lines}}$. Over these wavelength ranges, H_2O in particular has millions of spectral lines in each band. Figure 2.11 demonstrates the effect of increasing wavelength range on H_2O detection significance. Figure 2.11b shows a clear improvement when combining J and H bands over just observing J band alone (Figure 2.11a). Furthermore, H_2O is more difficult to observe in K band, as shown in Figure 2.11c and expected since H_2O has larger cross sections in J and H bands as shown in Figure 2.2. However, H_2O is much more detectable at fixed spectral resolution or S/N_{res} when J and H band are also observed (Figure 2.11d). Thus, instruments that can observe J-K band simultaneously will more readily detect H_2O and CO(which is detectable in K band but neither of the other two bands; see Table 2.3 with the same observations.

Looking to future instrumentation, GMTNIRS (Jaffe et al. 2016) is a proposed high-resoltuion spectrograph for the GMT that would cover 1 to 5 μm in one exposure. Table 2.3.3 shows the minimum S/N_{res} required to detect each opacity source when observing all bands (J-M) simultaneously. While the required S/N_{res} to detect H_2O is substantially less than when looking at any single band as shown in Table 2.3, other opacity sources are not as benefited by simultaneous wavelength coverage, due to their narrower span or dominance by H_2O over most bands. In particular, the minimum S/N_{res} required to detect CO and CO_2 is in most cases identical to that required for

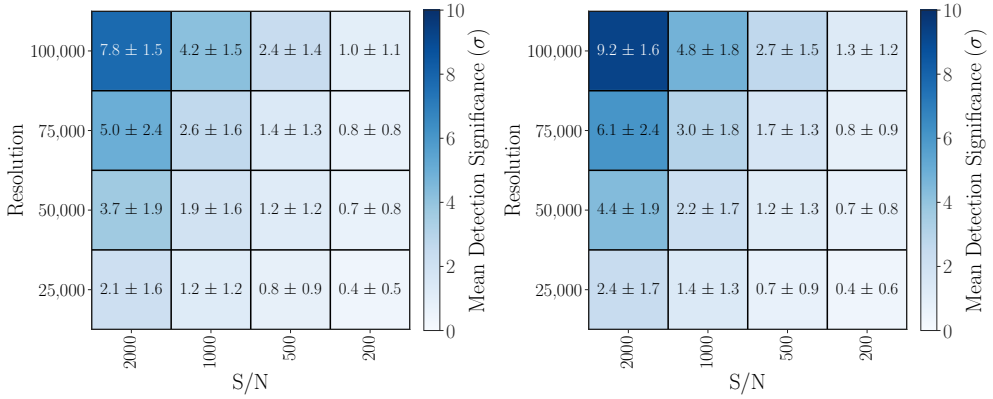

(a) J Band

(b) J and H Band

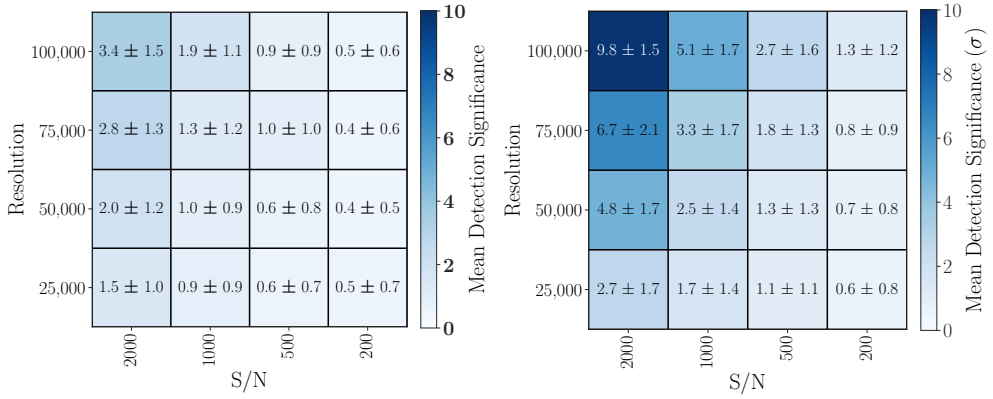

(c) K Band

(d) J, H, and K Band

Figure 2.11: Detection significances for H_2O for different observing bands as a function of spectral resolution and S/N per resolution element of the transmission spectrum. Observing J and H bands simultaneously increased the detection significance of H_2O as shown in 2.11a and 2.11b. Similarly, while the H_2O detection in K band is marginal in 2.11c, adding J and H bands allows for a much stronger detection of H_2O.

when considering solely M band spectra, so adding in other bands does not make either molecule easier to detect. Similarly, the minimum S/N_{res} reported for CH_4 in Table 2.3.3 are identical to those for analyzing solely L band spectra from Table 2.3. Thus, H_2O is the opacity source, under these specific atmospheric conditions, most benefited by an instrument with wide instantaneous wavelength coverage. In scenarios in which other broad-band absorbing molecules dominate, say, higher metallicity where CO/CO_2 are more prominent, or much cooler where CH_4 dominates the full near infrared, the influence of multiple bands on specific molecular detections would undoubtedly change. We leave this detailed analysis to a future study.

simultaneously.

2.3.4 Photochemical Products

Though our results so far have only included four molecules (CO, CO_2, H_2O, and CH_4), other molecules could be important opacity sources for these planets in the near infrared. In particular, photochemical products could affect the high-resolution transmission spectra at these wavelengths and their detection could provide an avenue to distinguish between a photochemical haze and equilibrium condensate clouds. However, not all potential molecules have high fidelity line lists at the temperatures and pressures necessary for generating these models. Hawker et al. (2018) and Cabot et al. (2019) have both presented evidence of HCN in the atmospheres of hot Jupiters using high-resolution spectroscopy, indicating the possibility of detecting this molecule with current line lists. Thus, to test whether photochemical products would be detectable with these kinds of observations, we focus on HCN as an illustrative example using the line list

Table 2.7: Minimum S/N_{res} required for $\geq 5\sigma$ detection of each opacity source for transmission spectra that cover observing bands *J*-*M*

Opacity Source	Insolation	Spectral Resolution			
		25,000	50,000	75,000	100,000
CO	0.3×	1400	800	600	400
	1×	700	350	250	200
	3×	400	250	150	150
CO_2	0.3×	4500	2400	1800	1200
	1×	4500	2400	1700	1300
	3×	4500	2200	1500	1100
H_2O	0.3×	2800	1500	1100	800
	1×	2600	1400	1100	800
	3×	1200	700	500	350
CH_4	0.3×	1100	700	450	300
	1×	-	-	-	-
	3×	-	-	-	-
Haze	0.3×	150	100	100	100
	1×	150	100	100	50
	3×	100	100	50	50

from Harris et al. (2008).

As in Section 2.2.1, we create a new "truth" spectrum that includes HCN in addition to our other opacity sources. We use the results of the photochemical model cited in Section 2.2.1 to determine the HCN abundance. We can then use the log(L) method described in Section 2.2 to compare to the models without HCN and quantify our ability to detect the molecule as a function of S/N_{res} and spectral resolution. We find that L band is the only observing band where HCN is detectable; so far the only spectra used to detect HCN in Hawker et al. (2018) and Cabot et al. (2019) covered 3.18 - 3.27 μm. The minimum S/N_{res} needed to detect HCN is listed in Table 2.3.4. HCN is only detectable for the hottest models and highest spectral resolutions. However, as shown in Figure 2.2, HCN has its strongest features between 3 and 3.2 μm. If spectra starting at 3.1 μm instead of 3.15 μm can be obtained, HCN could be much easier to detect - for example, the required S/N_{res} for 3$\times$ insolation and R $\sim$ 100,000 decreases from 3500 to 1000.

We also explore how unaccounted for photochemical products could affect the detectability of the major molecular species. Our "truth" spectrum inlcudes our standard set of opacities (CO, CO_2, H_2O, CH_4, and H_2/He CIA) plus HCN, but compare to models without HCN (e.g., an "incorrect" model). We find that the detection S/N values do not change in any case, even for L band where HCN is detectable (Table 2.3.4). This consistency suggests that our above results are robust against missing absorbers. However, since HCN is not easily detectable, the minimum S/N_{res} for a detection may be slightly higher than reported here if there are unaccounted-for molecules that would

Table 2.8: Minimum S/N$_{res}$ required for $\geq 5\sigma$ detection of HCN with L band spectra.

Insolation	Spectral Resolution			
	25,000	50,000	75,000	100,000
0.3×	-	-	-	-
1×	-	-	-	-
3×	-	-	4000	3500

Table 2.9: Minimum S/N$_{res}$ required for $\geq 5\sigma$ detection of each opacity source for transmission spectra in L band when HCN is included in the observed spectrum but not the comparison models. CO and CO_2 are not observable with S/N$_{res} \leq 5000$.

Opacity Source	Insolation	Spectral Resolution			
		25,000	50,000	75,000	100,000
H_2O	0.3×	-	4500	3500	2600
	1×	-	4000	3000	2600
	3×	3000	1500	1300	1100
CH_4	0.3×	1100	700	450	300
	1×	-	-	-	-
	3×	-	-	-	-
Haze	0.3×	300	200	150	100
	1×	400	250	200	150
	3×	300	200	100	100

more significantly affect the high-resolution transmission spectrum.

2.4 Discussion

2.4.1 Observability with Current and Future Instrumentation

In Section 3 we presented the required S/N per resolution element to detect molecules over a range of stellar insolation levels ($T_{\rm eff}$ = 412, 557, and 733 K) and

observational parameters (R $\sim$ 25,000 - 100,000, 50 $\leq$ S/N$_{res}$ $\leq$ 5000, and J - M bands). However, the exposure times required to reach these S/N$_{res}$ will vary depending on host star brightness, sky background, telescope aperture size, and instrument sensitivity. While a detailed instrument/observational investigation is outside the scope of this work, we can focus on GJ 1214b as an example of how these factors might affect observations.

We used a simplified noise model for estimating instrumental S/N$_{res}$ as a function of exposure time to determine the observability of molecules as a function of source brightness, telescope size, resolving power, and wavelength. The estimated measured S/N per resolution element depends upon the number of photons received from the source (which itself depends on exposure time, throughput, collecting area, brightness, and resolution), thermal background (which depends on emissivity, throughput, etendue AΩ, and temperature), and instrumental quantities such as total throughput ($\tau \sim$ 0.05), emissivity ($\epsilon = 0.3$), and noise properties of the detector (dark current, read noise), which all combine into:

$$S/N = \frac{S \times T}{\sqrt{S \times T + N_{exp} \times (T_{exp} \times (BKGD + DC) + RN^2)}} \tag{2.4}$$

where S is the signal, T is the total exposure time, $N_{\rm exp}$ is the number of exposures, $T_{\rm exp}$ is the time for a single exposure (assumed to be 600 seconds), $BKGD$ is thermal background, DC is the dark current, and RN is read noise.

Using this equation, it is then possible to estimate the S/N$_{res}$ expected for a given source magnitude, resolving power, and exposure time. For each molecule, we determined the minimum exposure time required to detect the molecule in the 1$\times$ inso-

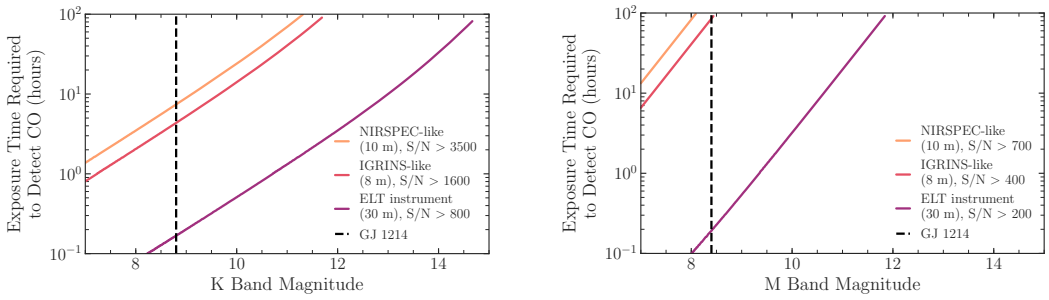

(a) (b)

Figure 2.12: Estimated exposure time required to detect CO as a function of host star magnitude for different instruments in K band (Figure 2.12a) and M band (Figure 2.12b). The magnitude of GJ 1214 is marked by the dashed line. We consider three different types of instruments- a "NIRSPEC-like" R∼25,000 spectrograph on a 10-m telescope, an "IGRINS-like" R∼50,000 spectrograph on an 8-m telescope, and a proposed R∼100,000 spectrograph behind AO on a 30-m telescope like the TMT. We find that although detecting CO requires a lower S/N_{res} in M band than K band, K-band observations are actually much more feasible, particularly for current instruments. However, a potential high-resolution spectrograph on a 30-m telescope would be able to detect CO in GJ 1214b in M band with one transit.

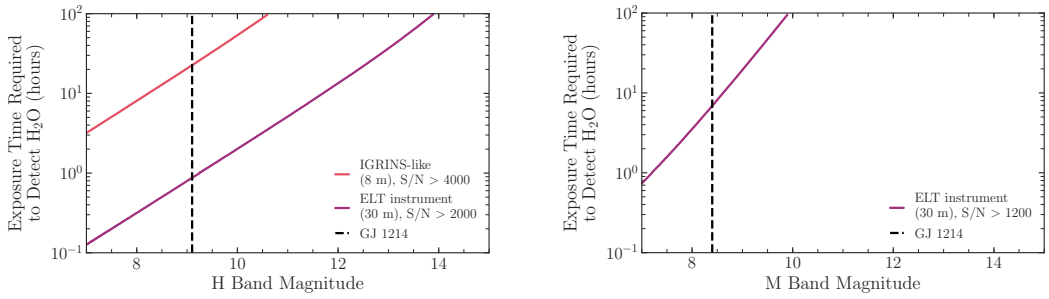

(a) (b)

Figure 2.13: Estimated exposure time required to detect H_2O as a function of host star magnitude for different instruments in H band (Figure 2.13a) and M band (Figure 2.13b). The magnitude of GJ 1214 is marked by the dashed line. In H band we did not have any H_2O detections with $S/N_{res} \leq 5000$ with R ∼ 25,000, so in Figure 2.13a we just consider an "IGRINS-like" R∼50,000 spectrograph on an 8-m telescope and a proposed R∼100,000 spectrograph behind AO on a 30-m telescope like the TMT. Similar to Figure 2.12, we find that although detecting H_2O requires a lower S/N_{res} in M band than H band, H-band observations are more feasible, particularly for current instruments. However, a potential high-resolution spectrograph on a 30-m telescope would be able to detect H_2O in GJ 1214b in H band with ∼ 7 hours of integration time.

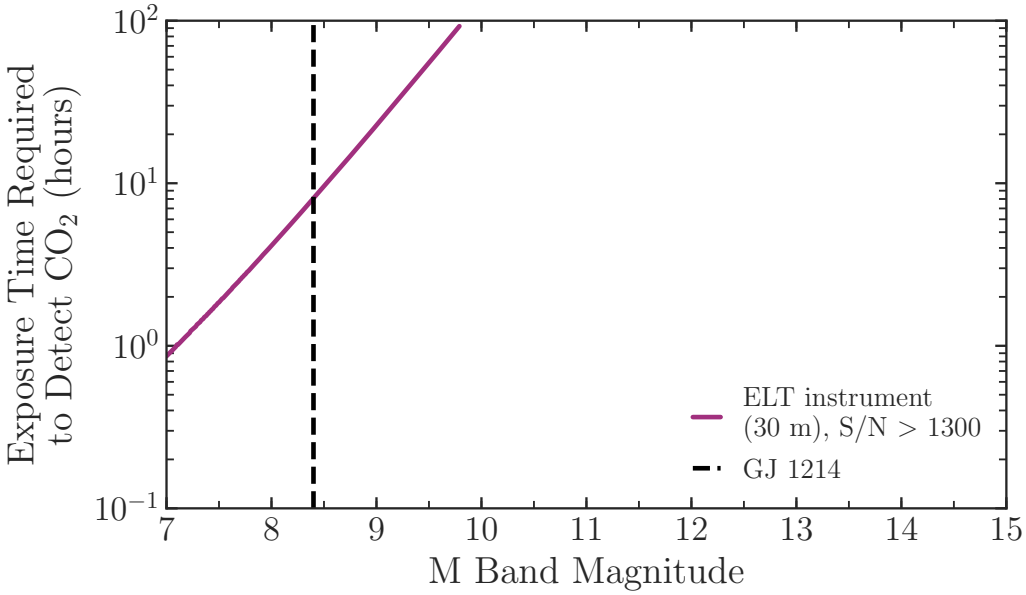

Figure 2.14: Estimated exposure time required to detect CO_2 as a function of host star magnitude for different instruments in M band. The magnitude of GJ 1214 is marked by the dashed line. Of our three investigated instrument types, only a proposed R$\sim$100,000 spectrograph behind AO on a 30-m telescope like the TMT can detect CO_2 in a reasonable amount of observing time ($\sim$ 8 hours for GJ 1214b).

lation scenario (using GJ 1214b-like planet/star parameters) for varying source brightnesses. We simulated the exposure time vs. source brightness relation for three different scenarios: 1) $R \sim 25,000$ instrument on a 10-m telescope, seeing-limited (e.g. NIRSPEC on Keck, McLean et al. 1998, Martin et al. 2018); 2) $R \sim 50,000$ instrument on an 8-m telescope, seeing-limited (e.g. IGRINS on Gemini, Park et al. 2014, Mace et al. 2018); 3) $R \sim 100,000$ instrument on a 30-m telescope, behind Adaptive Optics (AO), such as the proposed METIS on ELT (Brandl et al. 2018) or MODHIS (Mawet et al. 2019) on TMT. The dark current and read noise for the IGRINS-like and ELT instruments were assumed to be typical Teledyne values[4] ; the NIRSPEC-like curve used measured values from that instrument[5]. To easily normalize for each type of instrument, we assumed a "seeing disk" of 20 pixels per resolution element (assuming the resolution element in the imaging and dispersion directions was 5 pixels by 4 pixels). We assume exposures with the maximum practical length one would want to take in a particular band due to sky lines and thermal background: 600 seconds for K band and 30 seconds for M band. We do not assume any overhead time that might occur, for example due to detector readout, which would increase the required amount of telescope time for these observations. Each resolving power requires a different minimum S/N_{res} to detect a molecule. For example, in K band, to detect CO at 5σ significance for $1\times$ insolation, an R$\sim$25,000 instrument requires $S/N_{res} > 3500$, an R$\sim$50,000 instrument needs $S/N_{res} > 1600$, and an R$\sim$100,000 instrument needs $S/N_{res} > 800$.

Figure 2.12 shows the results of our noise observability analysis. For K band,

[4] http://www.teledyne-si.com/products/Documents/H2RG%20Brochure%20-%20September%202017.pdf

[5] https://www2.keck.hawaii.edu/inst/nirspec/Specifications.html

shown in Figure 2.12a, an instrument similar to NIRSPEC would take about 8 hours while the IGRINS-like instrument would take about 4 hours to detect CO. The mean transit duration of GJ 1214b is $52.73^{+0.49}_{-0.35}$ minutes, which translates to ∼8 transits with NIRSPEC and ∼4 transits with IGRINS. An ELT instrument behind AO with R∼100,000 would reduce this required time to around 6 minutes, so observing one full transit will be more than enough time. In contrast, for M band observations, both current instruments would take greater than 100 hours to detect CO due to the much higher background noise in this wavelength range. An ELT instrument behind AO would take about 8 minutes to detect CO in this wavelength range as shown in Figure 2.12b, so again one full transit would be more than enough time. However, we note that these observing times assume good observing conditions and could readily double in the case of low seeing or slit losses.

We performed similar observability calculations for H_2O and CO_2. For H_2O, we looked at H and M bands. For H band spectra, we did not detect H_2O with $S/N_{res} \leq$ 5000 for R∼25,000 (see Table 2.3) so Figure 2.13a only shows the exposure times for the IGRINS-like and TMT instruments. H band spectra with the IGRINS- like instrument would about 12 hours of total integration for H_2O to be detected. Detecting H_2O in M band spectra, however, would take an inordinate amount of observing time ($>$ 100 hours) with current instruments but again should be more easily detectable with about 7 hours on a 30-m telescope with AO for GJ 1214b. Similarly, only the R∼100,000 instrument on a 30-m telescope can detect CO_2 within any reasonable amount of time, $\sim$ 8 hours for GJ 1214b as seen in Figure 2.14.

2.4.2 Additional Caveats

There are other caveats to consider when using the S/N_{res} values in Tables 2-9 to plan observations for GJ 1214b or any other hazy sub-Neptune. First, when computing these values, we assumed all spectra covered the full wavelength range stated in Table 1, regardless of resolution, as the exact wavelength coverage varies between instruments. However, increasing spectral resolution may come with decreased wavelength coverage, leading to fewer spectral lines in the data, which would make these molecules more difficult to detect.

In addition, GJ 1214b has a relatively slow radial velocity change over the course of one transit (12 km s^{-1}; Crossfield et al. 2011), compared to the hot Jupiters for which this technique has successfully been applied. Thus, it may be difficult to remove the quasi-stationary contamination from our atmosphere and the star while preserving the planet spectrum.

Finally, we are assuming no contamination from stellar lines in our spectra (see Section 2.1). This is a good approximation for host stars with minimal spectral features in the observed wavelengths. However, for planets around M-dwarfs like GJ 1214, a myriad of stellar lines may make proper removal of the telluric and stellar contamination challenging. Brogi et al. (2016) and Schwarz et al. (2016) successfully modelled and removed stellar lines before removing the tellurics, but it remains to be seen if this technique can be successfully applied to M-dwarf spectra as more complex stellar models and data analysis are needed to remove overlapping stellar-planet molecular features (e.g., Chiavassa & Brogi 2019). Stellar variability may also pose a challenge, particularly for

combining data from multiple nights, especially for M-dwarfs which are known to have high levels of magnetic activity (e.g., Newton et al. 2016). As a result, a conservative approach may be to focus on detection and characterization of species unlikely to be abundantly present in M-dwarf photospheres (e.g., CH_4, NH_3, HCN, etc.).

2.5 Conclusions

In this work, we have investigated the feasibility of detecting molecules in the atmospheres of hazy sub-Neptunes with ground-based, high-resolution spectroscopy. To do so, we generated high-resolution transmission spectra of GJ 1214b analogs with a photochemical haze that matches the featureless low resolution transmission spectrum. We considered two different metrics from the literature to quantify our detection significances: the cross correlation function (CCF) and a log likelihood function (log(L)) derived by Brogi & Line (2019). While both metrics produced similar detection significances for molecules, only the log(L) was sensitive to the presence of the hazy opacity due to the additional terms that track the spectral variance relative to the data variance. Thus, we used the log(L) for the remainder of this work. However, our method relies on measuring the change in log(L) as we remove one opacity source at a time, indicating more care may need to be taken when determining which opacity sources to include in one's model.

We have calculated the minimum signal-to-noise (S/N) required for a $> 5\sigma$ detection of each opacity source (CO, CO_2, H_2O, CH_4, and the haze) as a function of stellar insolation, spectral resolution, and wavelength range. Our key results are as

follows.

1. High resolution infrared transmission spectrum observations for hazy GJ 1214b analogs probe pressures around 1 μbar and numerous molecular features can be detected for spectra that otherwise appear "featureless" at $R \sim$100-1000.

2. The haze is always the easiest opacity source to detect and observable in all observing bands. Thus, achieving the S/N per resolution element required to detect a molecule will also allow one to rule out a completely clear atmosphere.

3. H_2O is detectable with $S/N_{res} \leq 5000$ for almost all combinations of spectral resolution and wavelength coverage, and is the only molecule observable in J and H bands, but always requires a higher S/N_{res} than any other molecules observable in that band. In contrast, CO is only observable in K and M bands, but is the easiest molecule to detect. CO_2 is only observable in M band; in fact, M band is the observing band that requires the lowest S/N_{res} to detect two or more molecules at once (although in practice requires long observing time due to thermal background noise).

4. In general, increasing the stellar insolation of the model lowers the required S/N_{res} for molecular detections. However, CH_4 is only detectable in the L band spectra of the coldest models.

5. HCN is detectable with L band spectra for high resolution spectra of the hottest models. Detecting HCN, along with other potential photochemical products, could be a way to distinguish between equilibrium cloud and photochemical haze opacity

in a planet's atmosphere.

To further investigate the observability of these ultra-hazy sub-Neptunes, we used a simple model in Section 2.4 to determine the feasibility of observing high-resolution transmission spectroscopy of planets with current and future instruments. We found that detecting CO and H_2O for GJ 1214b with current instruments observing in K and H bands, respectively, requires on the order of 10 hours of observing time. Furthermore, though a lower S/N_{res} is required to detect these molecules in M band, current instruments would need an unreasonable investment of observing time due to the high background. However, such an observation would be trivial behind AO on an ELT class telescope. In addition, a high resolution spectrograph on an actively cooled space telescope could observe in M band without issues from thermal background.

As discussed in Section 2.4, more detailed, instrument-specific simulations for particular targets may be needed for careful observation planning. Such a study for ELT instrument concepts could help inform design decisions to maximize the information we can learn about these objects. Furthermore, an analogous study could be conducted of thermal emission spectra, which will likely require the S/N achievable with ELT instruments. A number of sub-Neptunes will be observable with *JWST*, albeit with lower spectral resolution. Analysis of simulated joint *JWST* and ground-based high-resolution observations could pinpoint optimal observing strategies to take full advantage of these complementary data sets. As more sub-Neptunes around bright, nearby stars are discovered (as expected from NASA's TESS mission; Barclay et al. 2018), considering the best application of observational techniques is essential to maximizing the scientific return

on this abundant class of planets.

Chapter 3

Brown Dwarf Retrievals on FIRE!: Atmospheric Constraints and Lessons Learned from High Signal-to-Noise Medium Resolution Spectroscopy of a T9

Dwarf

3.1 Introduction

Brown dwarfs, objects more massive than gas giant planets but yet not massive enough to sustain hydrogen fusion like a star (13 $M_{Jup} \lesssim M \lesssim 73\ M_{Jup}$, Burrows et al. 2001), provide essential testbeds of our understanding of the physics and chemical processes that sculpt substellar atmospheres. Without a sustained central energy source from fusion, brown dwarfs instead cool over time, leading to the formation of molecules and condensates in their atmospheres which dramatically affect their emitted spectra across the M, L, T, and Y spectral types (e.g. Kirkpatrick 2005; Cushing et al. 2011). The chemical and physical processes shaping these spectra are expected to be similar to those of gas giant exoplanets due to their similar effective temperatures (Faherty et al. 2016). Thus, the often more easily-observable spectra of brown dwarfs can inform our predictions for and interpretations of spectra of directly imaged planets.

Traditionally, brown dwarf spectra have been compared to theoretical "grid models" which use our current understanding of substellar atmospheres and evolution to produce model spectra for a small number of fundamental parameters, such as composition, effective temperature, and surface gravity (see Marley & Robinson (2015) for a review). The cost of a small number of parameters is the number of chemical and physical assumptions, for example radiative-convective and thermochemical equilibrium, that are required. These grid models are an important resource for connecting observed

properties with physical parameters of brown dwarfs as well as predicting signatures to be tested with future observations. However, while advancements in molecular opacities and the increasing model complexity have led to improved fits to observed spectra (Phillips et al. 2020; Marley et al. 2021), notable discrepancies remain (Leggett et al. 2021) indicating there is still much to be learned about modeling these cool atmospheres.

An alternative way to glean information from brown dwarf spectra is atmospheric retrieval, a data-driven Bayesian inverse method where minimal assumptions are made for the cost of far more free parameters. First developed for Earth and Solar System sciences (e.g. Rodgers 2000; Fletcher et al. 2007) and then adapted for exoplanets (e.g. Madhusudhan & Seager 2009; Benneke & Seager 2012; Line et al. 2013), atmospheric retrievals have been applied successfully to brown dwarf spectra of various spectral types (Line et al. 2014, 2015, 2017; Burningham et al. 2017, 2021; Zalesky et al. 2019, 2022; Gonzales et al. 2020, 2021, 2022; Kitzmann et al. 2020; Piette & Madhusudhan 2020; Howe et al. 2022; Lueber et al. 2022; Wang et al. 2022; Xuan et al. 2022; Calamari et al. 2022). Retrievals provide a way to test the assumptions included in grid models; for example, Line et al. (2017) and Zalesky et al. (2019) used retrievals of T and Y dwarfs to show a decrease of Na and K abundances with effective temperature, validating the rainout chemistry paradigm over pure equilibrium. However, while atmospheric retrieval can explore a wider range of possible atmospheres, unphysical combinations of parameters can still provide good fits to the data and therefore spuriously be preferred in retrieval frameworks. In particular, a number of brown dwarf retrieval studies have yielded unphysically small radius constraints (e.g. Burningham

et al. 2021; Lueber et al. 2022) or very high surface gravities (Zalesky et al. 2019). Therefore, comparison to theoretical expectations from grid models are still needed to ensure retrieval results are fully contextualized.

A vast majority of brown dwarf retrieval studies have been conducted on low-resolution (R $\sim$ 100) spectra. At medium-resolution, R $\gtrsim$ 1000, molecular bandheads are resolved into unique groups of densely-packed lines, allowing for more robust detections of molecules. Furthermore, the cores of strong lines are formed at lower pressures than can be sensed at low spectral resolutions, providing better probes of the upper end of the atmosphere's temperature-pressure profile. Comparisons of medium-resolution spectra of brown dwarfs to grid models have provided validations of certain line lists (Canty et al. 2015) and constraints on the brown dwarf's fundamental properties (e.g. Bochanski et al. 2011; Petrus et al. 2022; Hoch et al. 2022). Spectroscopy at medium-to-high spectral resolutions of brown dwarfs have been analyzed in retrieval frameworks, but often over a narrow wavelength range and with relatively low signal-to-noise, though they can also be combined with low-resolution observations for better constraints (Wang et al. 2022; Xuan et al. 2022).

The aim of this work is to test how the atmospheric retrieval framework works at medium spectral resolution (R $\sim$ 6000), in terms of both new insights and novel challenges. We use the same framework successfully applied at low-resolution (e.g. Line et al. 2017; Zalesky et al. 2022) for a spectrum with roughly 60$\times$ higher spectral resolution. This work is structured as follows. In Section 3.2, we describe our dataset, retrieval framework, and the modifications necessary at this spectral resolution. In

Section 3.3, we give an overview of the tests performed and changes made throughout this project, and the accompanying results and lessons learned. In Section 3.4, we put our results in context with constraints from low-resolution spectra of the same object, previous analysis of this dataset, and grid models. Finally, our conclusions are summarized in Section 3.5.

3.2 Methods

3.2.1 Spectra of UGPS 0722

We perform our analysis on the medium-resolution spectrum of UGPS 0722 presented by Bochanski et al. (2011, hereafter B11) obtained with the Folded-port InfraRed Echellette Simcoe et al. (2013, FIRE) at the Magellan Telescopes. This spectrum covers 0.85 to 2.5 μm over 21 orders with R $\sim$ 6000. We scaled the reduced and order-stitched spectrum of B11 to the observed H-band photometry on the Mauna Kea Observatories (MKO) photometric system following Line et al. (2017). We will explore potential issues with which regions of this spectrum to include in our analysis (for example due to telluric absorption or order stitching problems) in later sections.

We also use the low-resolution spectrum of UGPS 0722 from the SpeX Prism Library (Burgasser 2014), which covers a similar wavelength range of 0.8 to 2.5 μm with a wavelength-dependent resolution of $\sim$ 87-300. This spectrum was also calibrated to flux units using the same H-band photometry as for the FIRE spectrum. The flux-calibrated FIRE and SpeX spectra are shown in Figure 3.1.

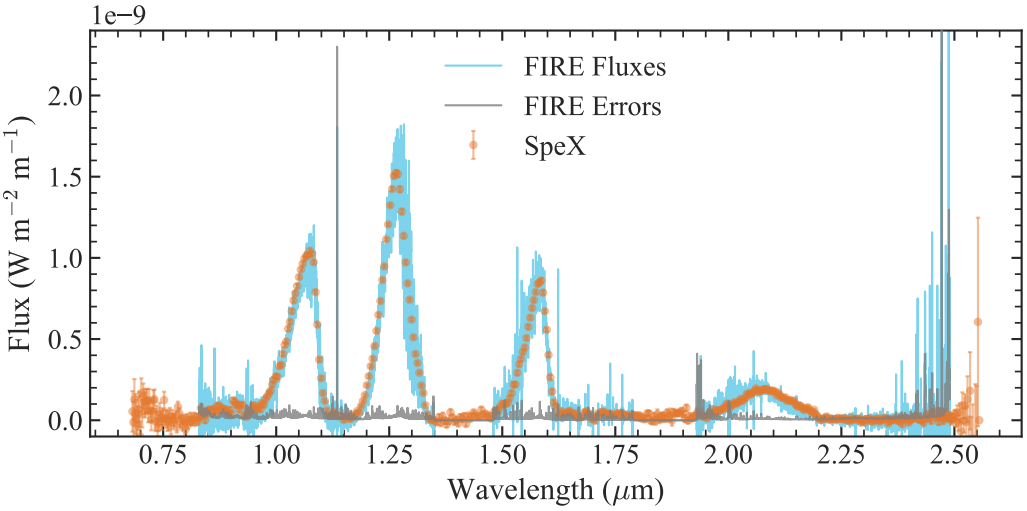

Figure 3.1: The FIRE (B11, R $\sim$ 6000) and SpeX (Burgasser 2014, R $\sim$ 87 - 300) spectra of UGPS 0722. The FIRE fluxes are in blue, FIRE errors in gray, and SpeX datapoints in orange. The FIRE spectrum is available for download online as supplementary data.

3.2.2 GPU Retrieval Framework

We use the CHIMERA retrieval framework successfully applied previously to low-resolution brown dwarf spectra (Line et al. 2015, 2017; Zalesky et al. 2019). However, generating a forward model emission spectrum at a resolution of $\sim$ 60,000 (which is then binned to R $\sim$ 6,000) is quite computationally expensive. Thus, to make this study feasible, we must use a modified version for use with graphical processing units (GPUs), that builds upon the code described in Zalesky et al. (2022). Specifically, we modify the radiative transfer to solve the two stream multiple scattering problem using the methods described in Toon et al. (1989). However, as we are not in a particularly cloud regime, the effects of multiple scattering are neglible. As in the previous studies done with this framework, we use the affine-invariant MCMC ensemble sampler package `emcee` (Foreman-Mackey et al. 2013). We include uniform-with-altitude volume mixing

Table 3.1: Free Parameters in Our Retrieval Model

Parameter	Description
$\log(f_i)$	log of the uniform-with-altitude volume mixing ratios of H_2O, CH_4, CO, NH_3, H_2S, Na, and K
log(g)	log surface gravity [cm s^{-2}]
$(R/D)^2$	radius-to-distance scale [R_{Jup}/pc]
T(P)	temperature at 15 pressure levels [K]
b	errorbar inflation exponent (Line et al. 2015)
γ, β	TP profile smoothing hyperparameters (Line et al. 2015)
log(Cloud VMR)	log of the cloud volume mixing ratio
$\log(P_c)$	log of the cloud base pressure
f_{sed}	sedimentation efficiency
RV	radial velocity [km s^{-1}]
$v \sin i$	rotational velocity [km s^{-1}]

ratios of H_2O, CH_4, CO, NH_3, H_2S, Na, and K, the surface gravity, a radius-to-distance scaling factor, the temperature-pressure (TP) profile, and three cloud parameters: cloud volume mixing ratio, the cloud pressure base, and the sedimentation efficiency (Ackerman & Marley 2001). As in Line et al. (2017), the TP profile is parameterized by 15 independent temperature-pressure points subject to two smoothing hyperparameters. These 15 temperature-pressure points are interpolated onto a finer 70 layer pressure grid for the radiative transfer using a cubic Hermite spline.

The chemical species and associated opacity sources used in this work are listed in Table 3.2.2. We began with the set of absorption cross-sections presented in Freedman et al. (2008) and subsequently updated as detailed in Freedman et al. (2014), Lupu et al. (2014), and Marley et al. (2021). However, we use a set of H_2O opacities calculated based on the POKAZATEL line list (Polyansky et al. 2018). In Section 3.3,

Table 3.2: Opacity Sources for Our Retrieval Model

Species	Opacity Sources
H2-H2, H2-He CIA	Richard et al. (2012)
H_2O	Polyansky et al. (2018)
CH_4	(1) Yurchenko & Tennyson (2014) (2) Hargreaves et al. (2020) (Section 3.3.3)
CO	Rothman et al. (2010b), isotopologues Li et al. (2015)
NH_3	(1) Yurchenko et al. (2011) (2) Coles et al. (2019) (Section 3.3.3)
H_2S	Tennyson & Yurchenko (2012), Azzam et al. (2015), isotopologues Rothman et al. (2013)
K	(1) see Marley et al. (2021) (2) Allard et al. (2016) (Section 3.3.6)
Na	(1) see Marley et al. (2021) (2) Allard et al. (2019) (Section 3.3.6)

we explore the effect of switching our opacity source for a number of species, including NH_3 (Coles et al. 2019), CH_4 (Hargreaves et al. 2020), K (Allard et al. 2016), and Na (Allard et al. 2019). For the cloud opacity, we used Mie scattering theory assuming a Mg_2SiO_4 cloud with optical properties from Wakeford & Sing (2015). However, the exact cloud species assumed should not particularly matter as cloud optical properties tend to be gray over these near-infrared wavelengths and the cloud's placement and extent in the atmosphere are parameterized independent of composition.

At these moderate resolutions, the radial and rotational velocities present in the spectrum, thus we add these as two additional parameters in the retrieval forward model. Both properties were measured in B11 by comparison to grid models. We use the *dopplerShift* function from PyAstronomy (Czesla et al. 2019) to shift the forward

modeled emission spectrum by a given radial velocity and interpolate it back onto the input wavelength grid.

For the rotational velocity, we first tested the *rotBroad* function from PyAstronomy which implements rotational broadening as described by Gray (2008) for a given v sin i and linear limb-darkening coefficient (we chose 0). This function convolves the modeled spectral lines with a wavelength-dependent line profile representing the Doppler line broadening from rotation, called the "broadening kernel." However, this method proved infeasibly slow, requiring 89 seconds to generate one broadened forward model spectrum. We then tested the *fastRotBroad* function from PyAstronomy, which uses a single broadening kernel that only depends on the median wavelength of the input data, leading to a much faster forward model generating time of 0.19 seconds but differences from the slower version that were larger than the error bars of the FIRE spectrum as shown in Figure 3.2. As a compromise, we split our spectrum into two and used *fastRotBroad* for each half, taking 0.2 seconds but leading to differences from the more accurate function that were smaller than the error bars.

To test how our retrieval framework might perform on the FIRE data of UGPS 0722, we generated a fake test data set. We used CHIMERA to create one forward model based on the TP profile from the Sonora Bobcat grid (Marley et al. 2021) for an object with T_{eff} = 600 K and log(g)= 4.0, giving it a radial velocity of 47 km s^{-1} and v sin i of 40 km s^{-1}. We assume constant with altitude chemical abundances with log volume mixing ratios of H_2O = -3.09, CH_4 = -3.33, CO = -10.37, H_2S = -4.59, NH_3 =-5.00, K = -6.80, and Na = -4.90. This forward model was convolved to the FIRE instrument

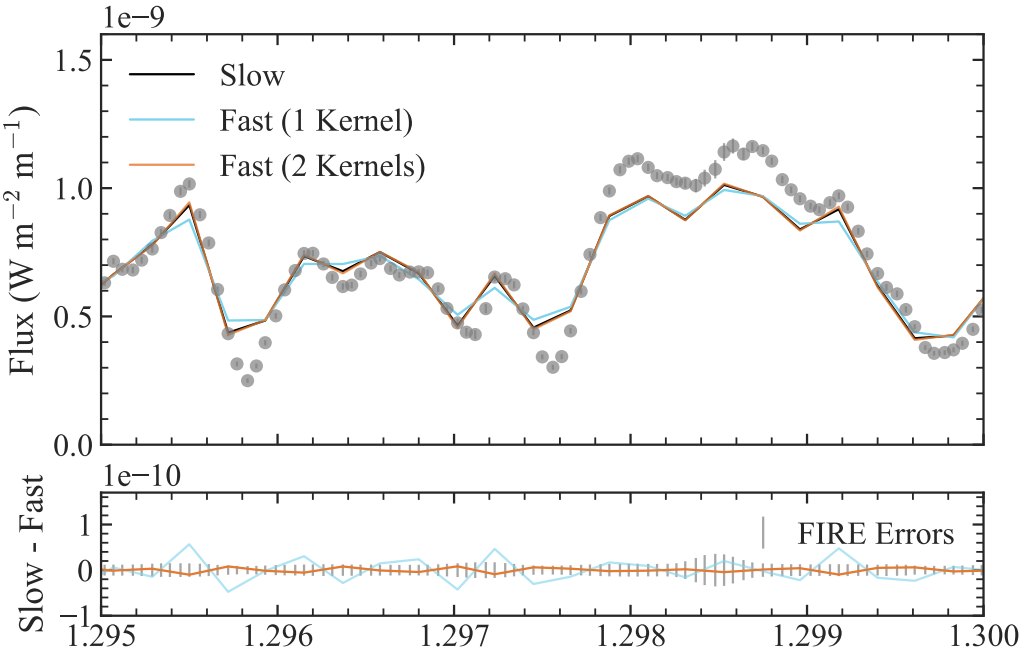

Figure 3.2: Comparison of different rotational broadening methods. The top panel shows modeled emission spectra using different rotational broadening methods compared to a snippet of the FIRE spectrum of UGPS 0722 shown in the grey data points. The bottom panel shows the difference between the model broadened with a wavelength-dependent kernel ("Slow") and those using either 1 or 2 broadening kernels for the spectrum ("Fast"), and the data error bars in this region. At least two broadening kernels, using the median wavelengths of the blue and red halves of the spectrum, are required to reduce the difference with the slower, more accurate method to smaller than the error bars on the FIRE spectrum.

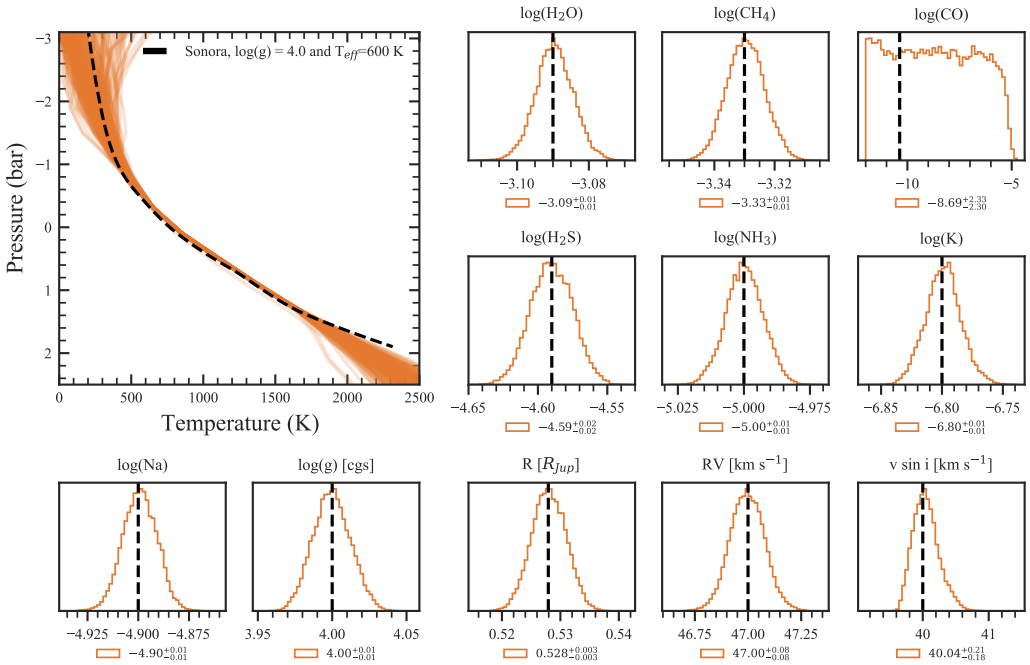

Figure 3.3: Retrieved TP profiles and posteriors of certain parameters for a "fake" FIRE spectrum based on the Sonora Bobcat model with an effective temperature of 600 K and surface gravity log(g)=4.0.

resolution, interpolated onto the wavelength grid of the FIRE spectrum, and given the same error bars as the FIRE spectrum of UGPS 0722. As such, we assume a $(R/D)^2$ value of 0.0158 (corresponding to a radius of ∼0.528 R_{Jup} for an object at the distance of UGPS 0722) which is needed to give the same peak flux to error ratio as the FIRE spectrum of UGPS 0722. The results from a CHIMERA retrieval on this test dataset compared to the input values are shown in Figure 3.3. We see that we are able to recover the input values with high accuracy and precision (with the exception of CO as it is unconstrained due to the low input mixing ratio), particularly with an unprecedented uncertainty of ∼ 0.01 dex on the chemical abundances and surface gravity, ∼10× more precise than constraints from spectra at R∼100 (Line et al. 2017; Zalesky et al. 2022).

3.3 Results

3.3.1 Initial Fire Retrieval vs. SpeX

Initially, we used the entire order-stitched and flux-calibrated FIRE spectrum UGPS 0722, with a few spurious data points effectively ignored by greatly inflating their error bars. However, in regions of high telluric absorption, the error bars on the spectrum were artificially underestimated (almost 14 orders of magnitude more precise than elsewhere). To prevent these data points from incorrectly driving our results, the error bars in these regions are inflated to a high enough value that these data points functionally do not contribute to our retrieval analysis. We also mask out those regions of strong telluric absorption in the SpeX spectrum as well to allow for a direct comparison.

Figure 3.4 shows the retrieved TP profiles and posterior distributions for selected parameters from our initial analysis on the UGPS FIRE spectrum compared to results from the SpeX spectrum. Though the FIRE spectrum potentially offers more precision than the SpeX results, we find our MCMC chains have trouble converging, with bimodal posteriors, unphysical values for certain parameters like the surface gravity, and very jagged TP profiles.

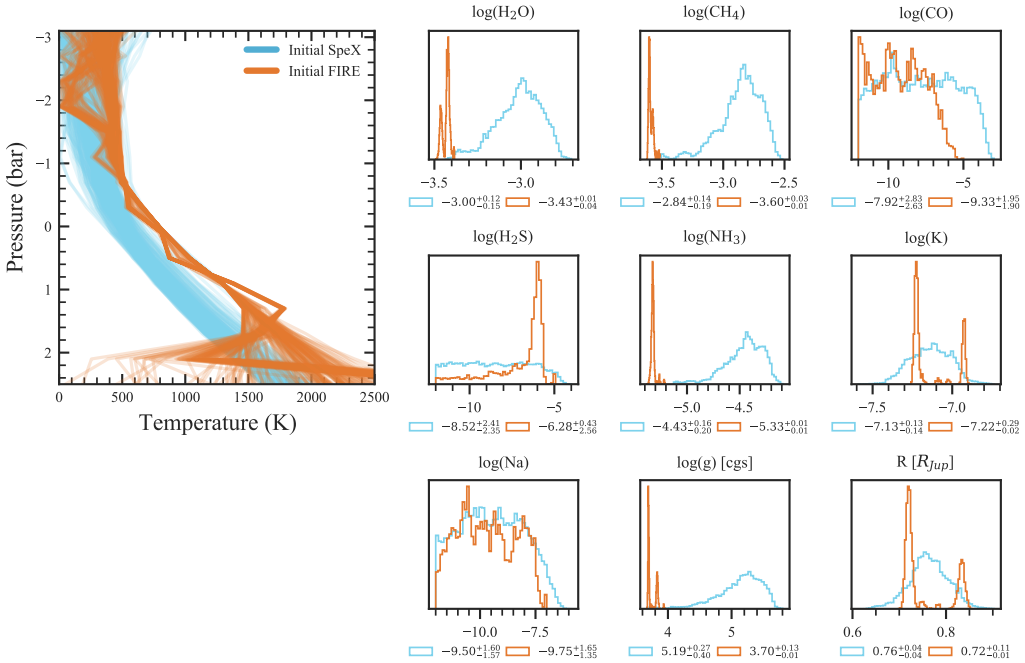

Figure 3.4: Retrieved TP profiles and posterior distributions for selected parameters for initial retrievals on the SpeX and FIRE spectra of U0722.

We suspected our forward model was too flexible, which was leading to overfitting and unphysical results. We reduced the number of parameters in our model by fixing the second TP profile smoothing hyperparameter β and the cloud parameters to specific values. Line et al. (2017) found letting β vary had a negligible effect compared to the nominal fixed value of $\beta = 5 \times 10^{-5}$ used by Line et al. (2015). As previous work

(Line et al. 2015, 2017) showed little evidence for optically thick clouds in T dwarfs, we set the cloud opacity parameters log(Cloud VMR), log(P_c), f_{sed} = [-15, 2, 10], consistent with an optically thin cloud deck.

The effect of fixing β and the cloud parameters is shown in Figure 3.5 in orange. The TP profiles are smoother and more precisely constrained, while we no longer see bimodal posteriors for the plotted parameters. We note a potential detection of H_2S in this object, although the posterior on the H_2S abundance has a long lower tail. We will explore letting the cloud parameters vary again in Section 3.3.8.

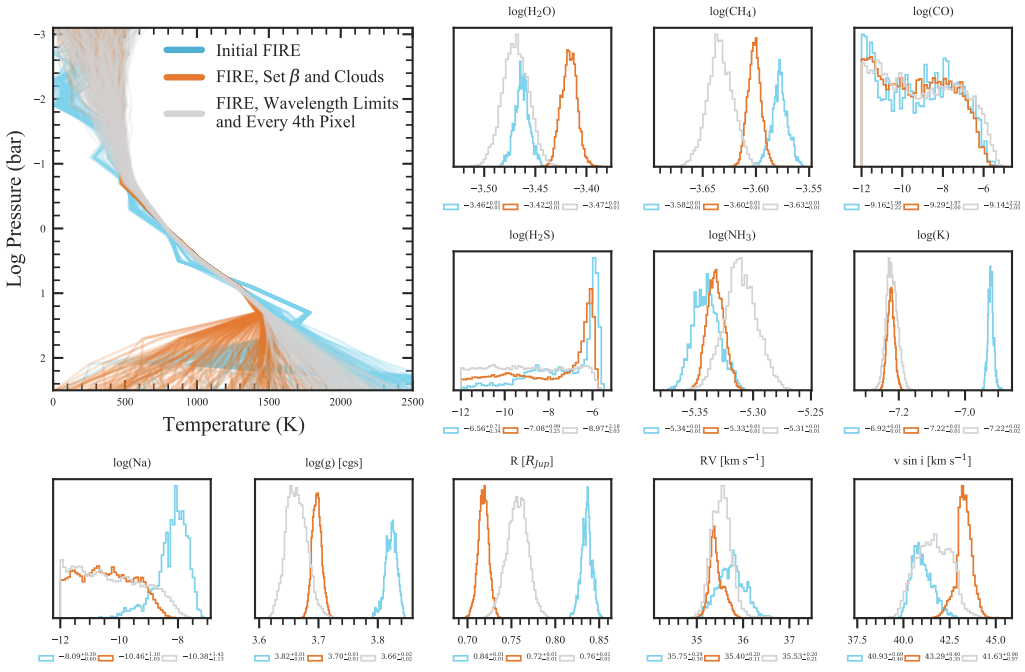

Figure 3.5: Effect on the retrieved TP profiles and selected posteriors of fixing the smoothing hyperparameter β and cloud parameters to set values (orange). In Section 3.3.2, we then limited the input spectrum to 0.9-2.35 μm and took every fourth pixel to limit the analysis to one data point per resolution element (grey).

3.3.2 Effect of Resolution Element and Wavelength Limits

Next, we decided to more mimic the analysis of B11 and limit the FIRE spectrum to 0.9 - 2.35 μm when comparing to models, effectively getting rid of the noisiest regions of the spectrum at the beginning and end. Additionally, like SpeX, the FIRE spectrum is oversampled compared to a spectral resolution element, so we take every 4th pixel of the spectrum to ensure independent data points (e.g. Line et al. 2017; Kitzmann et al. 2020).

Figure 3.5 shows the effect of these two changes in grey. While the retrieved TP profiles are very similar to the previous results at pressures less than $\sim$ 15 bars, the deep atmosphere is much warmer. The molecular abundances often shift slightly, but with the exception of H_2O the new posteriors are within 1σ. Our precision on almost all parameters also decreases, due to the substantial decrease in the number of included data points.

3.3.3 Effect of Updated Line Lists

In an effort to improve our best model fit to the observed spectrum, we investigated the effect of changing the sources of line lists used for CH_4 and NH_3. For NH_3, we upgraded to the more recent CoYuTe (Coles et al. 2019) ExoMol line list instead of the older BYTe (Yurchenko et al. 2011) list we were using previously. For CH_4, we replaced the ExoMol 10to10 list (Yurchenko & Tennyson 2014) with the recent HITEMP line list published by Hargreaves et al. (2020) which combined the more accurate ab initio line lists of Rey et al. (2017) with HITRAN2016 data (Gordon et al. 2017).

Comparisons of these "old" and "new" line lists for CH_4 and NH_3 at a specific pressure and temperature are shown in Figure 3.6. The two CH_4 opacities on the left show clear deviations beyond just shifts to line positions, especially blueward of ~ 1.62 μm. Hargreaves et al. (2020) demonstrate the better match of their CH_4 line list to experimental data for this wavelength region than the ExoMol CH_4 line list. In contrast, while minor differences are evident between the two NH_3 line lists in the right panel, they have similar overall values across the wavelength region of the spectrum. The effect of these changed line lists on our retrieved parameters is discussed below.

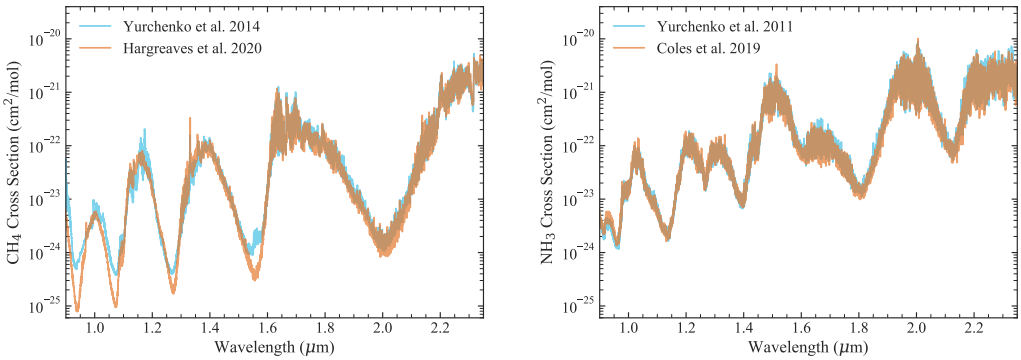

Figure 3.6: Comparison of old and new molecular cross sections at 725 K and 1 bar, and smoothed to R $\sim$ 6000. *Left*: Comparison of CH_4 cross sections from the ExoMol 10to10 (Yurchenko & Tennyson 2014) and HITEMP (Hargreaves et al. 2020) line lists. *Right*: Comparison of NH_3 cross sections from the older BYTe (Yurchenko et al. 2011) and newer CoYuTe (Coles et al. 2019) ExoMol line lists.

Low Resolution Retrievals

Figure 3.7 shows the effect of these updated line lists on the retrieved TP profile and selected posteriors for the SpeX spectrum. The retrieved TP profiles are consistently warmer than those obtained when using the Yurchenko & Tennyson (2014) CH_4 and Yurchenko et al. (2011) NH_3 line lists. Constraints on the abundances of H_2O, CH_4, and

NH_3 all shift to lower values, while the retrieved abundance of K increases by ~ 0.5 dex. The retrieved surface gravity also decreases, from log(g)=$5.19^{+0.27}_{-0.40}$ to log(g)=$4.43^{+0.27}_{-0.17}$ (cgs). Furthermore, the retrieved radius, assuming the parallax distance of 4.12 ± 0.04 pc (Leggett et al. 2012), decreases from $0.76^{+0.06}_{-0.04}$ to $0.5^{+0.03}_{-0.02}$ R_{Jup}, an unphysically small value (see Section 3.4.1 for further discussion). Notably, the dramatic decrease in both surface gravity and radius are driven by updating the CH_4 line list, as this effect occurs even when the NH_3 line list is kept the same.

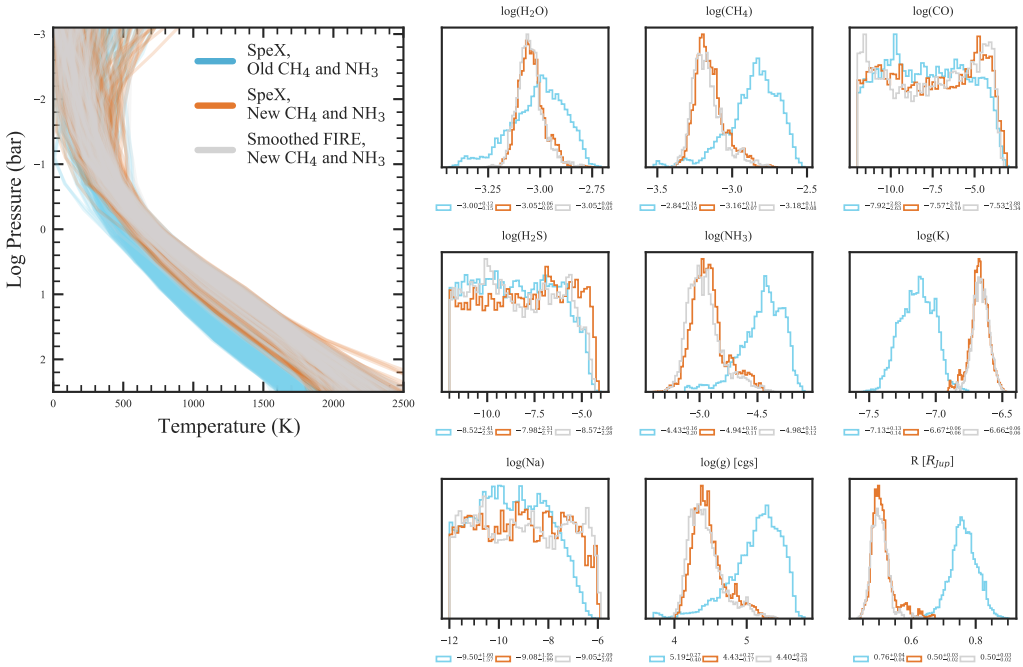

Figure 3.7: Effect on the retrieved TP profiles and selected posteriors of updating the CH_4 and NH_3 line lists to those of Hargreaves et al. (2020) and Coles et al. (2019), respectively, for the SpeX spectrum (orange). Results for the FIRE spectrum smoothed to the resolution of SpeX (grey) agree well for all parameters with those from the SpeX spectrum.

To assess if the FIRE dataset is consistent with the SpeX spectrum, we smoothed and sampled the FIRE data down to the SpeX resolution. Our retrieval results on this

smoothed FIRE spectrum are compared to the original SpeX results (both with the updated cross sections) in Figure 3.7. The retrieved constraints arising from the smoothed FIRE spectrum and the SpeX spectrum show remarkable agreement. This suggests that at low resolutions, observations at different times with completely different instruments produce extremely consistent results, given our retrieval model assumptions.

Medium Resolution Retrievals

With the increased spectral resolution of FIRE, we can better assess the accuracy of the line positions in various line lists. Figure 3.8 shows two narrow regions of the FIRE spectrum of U0722 where CH_4 and NH_3 are dominant in the left and right panels, respectively. For each molecule, we show model spectra generated with the updated line lists. In both cases, our newer line lists are better able to replicate the line positions of their respective molecules. Both the Hargreaves et al. (2020) and Coles et al. (2019) line lists incorporated empirical energy levels where available, as opposed to solely computed ones, leading to improved line position accuracy.

Unsurprisingly, improving the fit to line positions in our model does affect our retrieved atmospheric parameters. Figure 3.9 shows how updating the line lists of CH_4 and NH_3 affects our retrieved TP profiles and posteriors in orange. While the TP profiles are relatively similar deeper than $\sim$ 1 bar, the scenario with updated line lists prefers the atmosphere to be as cold as possible around 0.2 bars. Our retrieved posteriors for all molecular abundances as well as potassium do shift to higher values. The surface gravity also increases, from a median log(g) = $3.66\ ^{+0.02}_{-0.02}$ to log(g) = $4.08\ ^{+0.03}_{-0.03}$(cgs), a more plausible value. However, the radius decreases just like for the SpeX retrieval

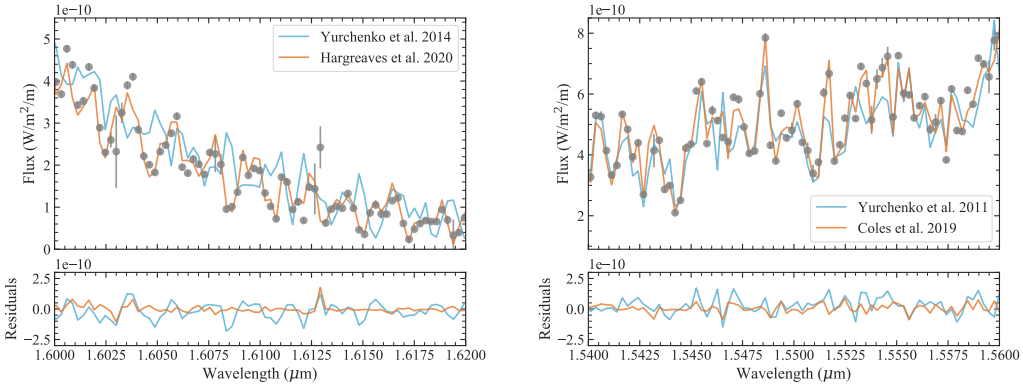

Figure 3.8: Comparisons of median model spectra for retrieval results using old and new molecular line lists, compared to the FIRE spectrum of U0722 in narrow regions of the spectrum where CH_4 and NH_3 are expected to dominate on the left and right, respectively. *Left:* Models with Yurchenko & Tennyson (2014) and Hargreaves et al. (2020) CH_4 line lists; the Hargreaves et al. (2020) line list does a significantly better job at matching the CH_4 lines in this region. *Right:* Models with Yurchenko et al. (2011) and Coles et al. (2019) NH_3 line lists; the Coles et al. (2019) line list improves the fit to NH_3 lines in this region.

in Section 3.3.3, from $0.76^{+0.01}_{-0.01}$ to $0.53^{+0.01}_{-0.01}$ R_{Jup}, an unphysically small size, which we discuss more in Section 3.4.1. The retrieved radial velocity and v sin i are relatively unaffected by our choice of CH_4 and NH_3 line lists, indicating these measurements may be primarily driven by H_2O lines in the spectrum.

Notably, we retrieve bounded constraints on the H_2S and CO abundances; CO constraints were unbounded when using the older line lists. Figure 3.10 shows model spectra for the median retrieved parameters, with and without H_2S, where we expect H_2S opacity to have an effect. Both H_2S and CO have the greatest effect on our model spectra between $\sim 1.56 - 1.60\mu$m where there is a window in the combined opacity of H_2O and CH_4. Including H_2S does improve the model fit in this region of the spectrum, but mostly as an overall shift in strength of features. However, around 1.59 μm there is what appears to be an H_2S line that is blended with another feature but clear in the

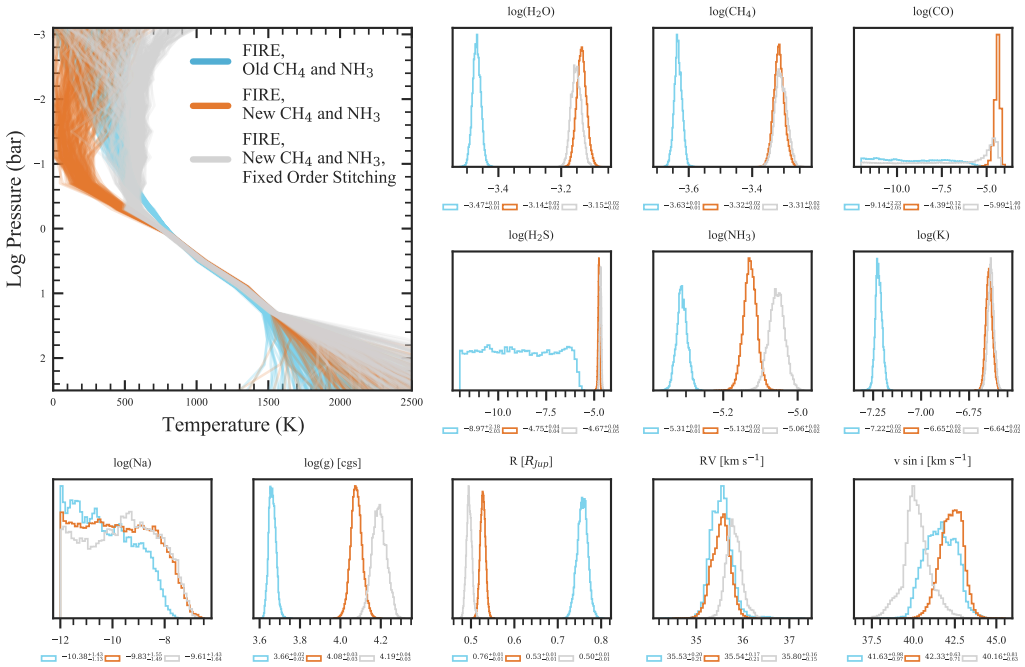

Figure 3.9: Effect on the retrieved TP profiles and selected posteriors from the FIRE spectrum when updating the CH4 and NH3 line lists to those of Hargreaves et al. (2020) and Coles et al. (2019), respectively (orange). The retrieved TP profiles and selected posteriors resulting from removing regions of the data where order stitching was not successful (Section 3.3.4) are shown in grey.

residuals shown on the bottom. Tannock et al. (2022) reported an H_2S detection in a high signal-to-noise, R $\sim$ 45,000 spectrum of a T6 dwarf, where they show a strong H_2S feature at this exact location around 1.59 μm. Thus, our constraint on the H_2S abundance is consistent with this feature, though it is dependent on a relatively small number data points ($\sim$3 points for the 1.59 μm feature and $\sim$ 20 others). Figure 3.11 shows models with and without CO, for the region of the spectrum where the model spectra are most different from each other. While the inclusion of CO does improve our model fit in this region, there is not a clear CO feature to point to as the source of our CO constraint. Thus, while we do have a bounded posterior for the CO abundance, it is perhaps a less trustworthy detection.

3.3.4 Issues with Order Stitching

FIRE observations in cross-dispersed mode are spread over 21 different orders. These orders have some overlap in wavelength coverage on either end. The final stitched spectrum published by Bochanski et al. (2011) combined these orders into a single spectrum by averaging the regions where the orders overlapped. However, in some cases when one order was noisier than the other, this averaging can lead to data artifacts. We first noticed this issue when inspecting the spectrum around 2.1 μm, where a jump or step in the data appears that is not possible to reproduce with our forward models, as shown in the top panel of Figure 3.12. Additional examples of overlap regions potentially subject to order stitching problems are shown in the lower two panels. While neither panel shows a step similar to the one seen at 2.09 μm, both cover regions where there is substantial disagreement between the two component orders leading to perhaps

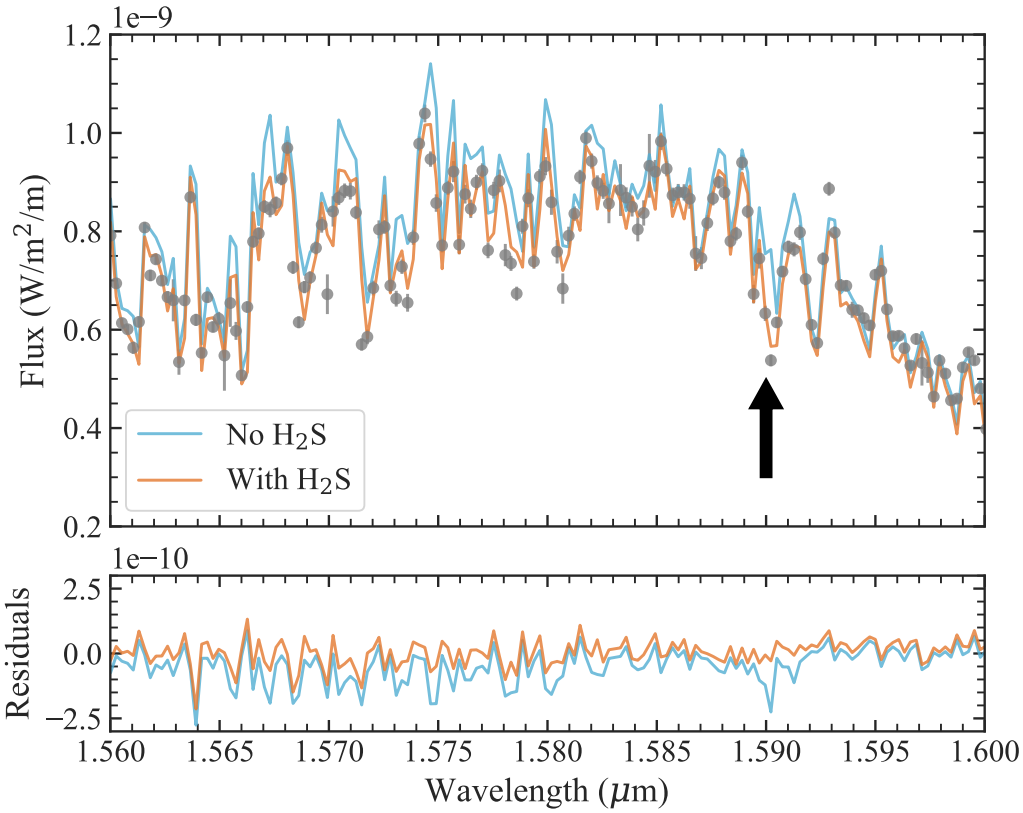

Figure 3.10: Model spectrum from the median retrieved parameters generated with (orange) and without (blue) H_2S, compared to a snipppet of the FIRE spectrum where H_2S opacity is expected. Some features are better fit with the inclusion of H_2S. The black arrow indicates a blended H_2S line consistent with the H_2S detection of Tannock et al. (2022).

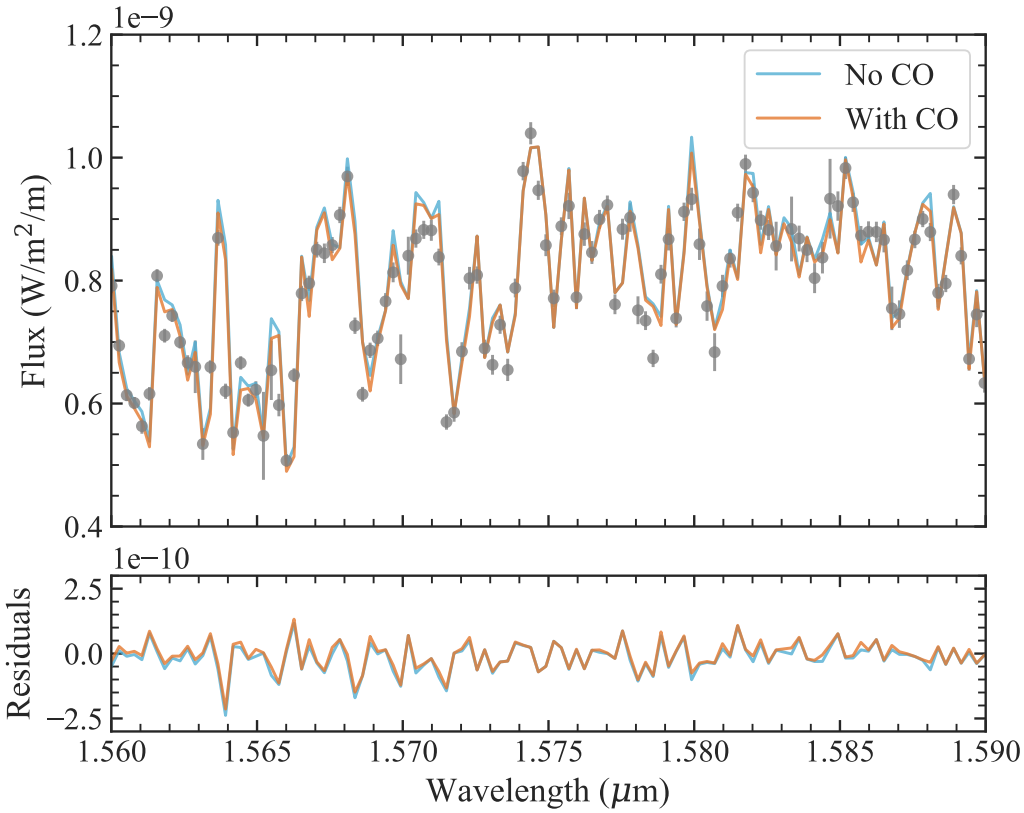

Figure 3.11: Model spectrum from the median retrieved parameters generated with and without CO, compared to a snipppet of the FIRE spectrum where some CO opacity is expected. While including CO does slightly improve the fit to the data, the effect is slight.

unphysical features in the stitched spectrum, particularly towards the middle of the overlapping areas.

To avoid these potential order stitching issues from biasing our retrieved results, we artificially inflated the error bars in order overlap regions where the final stitched product differed from either input order spectrum by more than 10%, effectively removing these data points from our analysis. 3.9 shows the result of removing these order stitching artifacts on our retrieval results in grey. Though the region of the atmosphere shown in Figure 3.12 is near the peak of K band and thus probes hotter parts of the atmosphere, other problematic order overlap regions masked by this process were on the edges of peaks in the spectrum and therefore contributed spuriously to constraints on the TP profile of the upper atmosphere. Our molecular and alkali abundances change slightly, with a less precise constraint on the amount of CO. While our median retrieved surface gravity increases to a slightly more plausible value of log(g)= $4.19\ ^{+0.04}_{-0.03}$ from log(g) = $4.08\ ^{+0.03}_{-0.03}$(cgs), our median radius shrinks even more to $0.50^{+0.01}_{-0.01}$ R_{Jup}. Finally, our retrieved radial velocity and v sin i posteriors also slightly shift as well.

3.3.5 Retrieving on Subsections of the Spectrum

While our stitched FIRE spectrum of U0722 covers y - K bands, we wanted to investigate the constraining power of different sets of spectral bands. In particular, Hargreaves et al. (2020) retains the completeness limits of the input line lists from Rey et al. (2017), giving a temperature-dependent maximum wavenumber limit for which the CH_4 line list can be considered complete, or including all lines strong enough to

affect the resulting opacity. This limit is 10700 cm^{-1} or 0.93 μm for 1300 K, and 9500 cm^{-1} or 1.05 μm for 1400 and 1500 K. Thus, the Hargreaves et al. (2020) CH_4 line list is not complete for the deeper, hotter temperatures probed by the y band. Motivated by this potential completeness problem, we retrieved on the J - K band data only, followed by a retrieval on solely H - K bands.

Comparisons of the retrieved TP profiles and select posteriors are shown in Figure 3.13. The TP profiles get cooler as the shorter wavelength data is progressively removed from the analysis. As the flux in y and J bands comes from deeper in the atmosphere, we do not constrain the temperatures to as deep of pressures without these data, as indicated by the "fanning out" of the TP profiles in these deeper layers. The H_2O and CH_4 abundances shift to higher values when just looking at H and K bands. While our constraint on the CO abundance becomes more precise for the J-K retrieval, there is still a long tail towards low values. The H_2S and NH_3 posteriors shift slightly with the exclusion of the y band data. While we lose all constraints on the K abundance for just H & K, we have a very precise and high constraint on the Na abundance when looking at J-K bands. Our retrieved surface gravity is also higher for the J-K retrieval than the other two, with a median of $\log(g)=4.31^{+0.06}_{-0.04}$. We retrieve a larger radius as we remove each bluer band of data, perhaps reflecting the cooler TP profiles retrieved for these cases as well. Finally, removing the J band data causes quite a shift in the retrieved radial velocity and v sin i values, pointing to the importance of the strong water lines in J band to our constraints on these values for the full spectrum.

Given that the Hargreaves et al. (2020) line list is not complete for y band at

the temperatures found in this object, the J-K retrieval is perhaps a compromise between CH_4 line completeness while retaining some flux from deeper in the atmosphere. However, the anomalously high Na abundance does call into question the physical plausibility of these results.

3.3.6 Effect of Alkali Opacities

Another change we made to our framework was to update the opacities used for the alkali metals Na and K. In particular, their strong lines at ~ 0.59 and 0.77 μm can be very broadened and significantly impact the near infrared spectrum of a brown dwarf. Prescriptions for these line profiles can vary quite a bit. We first used older alkali opacities based on the unified line-shape theory (Allard et al. 2007a,b), as used in the Sonora Bobcat grid (Marley et al. 2021); example cross-sections of Na and K for 725 K and 1 bar are shown in Figure 3.14, which basically become flat continuum opacity sources after a certain wing cutoff point. The high retrieved Na abundance for the J-K retrieval in Section 3.3.5 above can then be understood as an additional source of continuum opacity used to reduce J band flux which is not penalized when the y band is excluded. These alkali opacities were shown by Gonzales et al. (2020) to produce more physically reasonable alkali abundances in their retrieval study of a d/sdL7+T7.5p binary than those from Burrows & Volobuyev (2003). In contrast, newer cross sections based on the recent theoretical advancements of Allard et al. (2016, 2019) have more complicated shapes and significantly lower cross sections redward of ~ 1.2 μm.

These differences demonstrated in Figure 3.14 between the older and newer

line profiles can greatly affect our retrieved parameters. To isolate the differences, we retrieved on the SpeX data with just updating the Na cross sections, just updating K, and then updating both simultaneously. The retrieved TP profiles and selected posteriors for the different alkali treatments for the SpeX data are shown in Figure 3.15. Updating the Na opacity on its own does not particularly affect our retrieved results, perhaps unsurprisingly since the older K cross sections have so much more opacity. Updating to the new K causes a large change to our retrieved TP profiles, causing a very cold upper atmosphere with an inversion and a hotter, more precisely-constrained profile from ∼1 - 10 bars. The retrieved surface gravity and radius also decrease. Finally, updating Na and K at the same time is mostly similar to when just using the new K, except for a very high amount of retrieved Na.

Figure 3.16 shows the effect of updating the alkali cross sections on our retrieved TP profiles and posteriors of selected parameters for the FIRE data of U0722. Similarly to the SpeX retrieval, the retrieved TP profile is hotter from ∼1 - 10 bars and goes to 0 K (unphysical) at ∼0.1 bars before inverting back to higher temperatures. The abundances of many species shift to higher values, particularly Na which again has an extremely high abundance. Additionally, the CO posterior loses its long low tail, leading to a higher median abundance. We also retrieve a lower surface gravity, concordant with the SpeX results, while the radius increases slightly.

Looking at a spectrum generated with the median retrieved parameters compared to one with significantly less Na, we see that the only discernible differences occur from ∼0.9 - 0.98 μm shown in Figure 3.17. The gaps in the FIRE data shown

were regions where order stitching was found to be an issue as discussed in Section 3.3.4. Although the high Na model does get closer to fitting the data in this region, it is still not a particularly good fit by eye, completely missing many of the data points. Furthermore, this is one of the noisiest regions of the data. Thus, the high retrieved Na abundance is likely a spurious result driven by low signal-to-noise data in these regions.

We ran another retrieval on the FIRE data with the new alkali cross sections, but without any data blueward of 1 μm. The results are shown in Figure 3.16. The previous high Na constraint disappears as expected. While other posteriors shift as well, the constraints on the other species change only slightly. However, the inverted TP profile and even lower surface gravity compared to the retrieval with the old alkali cross sections are a cause for concern. Therefore, the old alkali cross sections are preferred as they give us more physical results. Further studies of the alkali line profiles and their effect on retrievals in particular would help provide context for these results and guidance for future medium resolution retrievals.

3.3.7 Setting the Radius to 1 Jupiter Radius

Given the unphysically small retrieved radius for U0722, we explored the impact of fixing the retrieved radius to 1 Jupiter radius on the TP profile and abundance constaints. Figure 3.19 shows the retrieved TP profiles and selected posteriors with this fixed radius in orange compared to when the radius is allowed to vary for the retrieval described in Section 3.3.4. The retrieved TP profiles overlap with the previous results for $\sim$2-4 bars but with a slightly different slope, as they are hotter above and cooler below this region. All abundance posteriors shift, including the disappearance of the

long low tail for CO, except for H_2S which remains relatively unchanged. In particular all abundance shifts are to lower values, perhaps balancing out the cooler temperatures in the deep atmosphere where the flux in y and J bands originates. The radial velocity posterior is strangely trimodal; however, one peak does correspond to the previous value. The $v \sin i$ posterior does shift as well. Importantly, the surface gravity decreases to an unphysically small median value of log(g)= 3.45. Figure 3.18 in the shows the correlations between parameters for the retrieval discussed in Section 3.3.4. Gravity is notably positively correlated with the abundances of major absorbers (H_2O, CH_4, NH_3) as well negatively correlated with the radius (through the scaling factor $(R/D)^2$). As gravity increases, the column optical depth decreases, leading to more flux particularly in the peak of each band (see Figure 2 of Line et al. 2015). Therefore, when the radius is fixed to the larger value of 1 R_{Jup}, the retrieval converges on a smaller gravity value to balance out the increase in flux (which is also consistent with the lowered abundances). Due to this questionably low surface gravity, we do not use this fixed radius retrieval to compare to SpeX and grid models in Section 3.4.

We next considered fixing the surface gravity simultaneously with the radius, choosing log(g)=4.5 consistent with a recent grid model study of U0722 (Leggett et al. 2021). The resulting TP profile and posteriors are shown in Figure 3.19 in grey. Since the gravity can no longer be decreased to account for the increased flux from a 1 R_{Jup} object, the retrieved TP profile is significantly colder than the other two plotted retrievals for the entire region of the atmosphere where it is well-constrained, about 0.5 to 50 bars. We will compare this TP profile to grid model predictions in Section 3.4. All abundance

posteriors shift significantly compared to when the radius and surface gravity are allowed to vary, though the direction of this shift varies for different species. The radial velocity and v sin i posteriors change slightly as well, though the former does not exhibit the same trimodal behavior as when the radius alone is fixed. While these constraints seem more plausible than those obtained when only the radius was fixed to a certain value, the fit to the data does suffer compared to when the radius and gravity are allowed to vary, as shown in Figure 3.20. Furthermore, our choice of fixed radius and surface gravity, while guided by previous studies of this object, are still relatively arbitrarily chosen. As the benefit of a retrieval analysis is to obtain constraints with fewer a priori assumptions than fitting the data to grid models, we do not use this fixed radius and gravity retrieval as our "preferred" FIRE retrieval in Section 3.4 for comparing to SpeX and grid model results.

3.3.8 Cloudy Retrieval

In Section 3.3.1 we fixed our cloud parameters to be consistent with an optically thin cloud that would not affect the emission spectrum when it appeared our model was perhaps too flexible. After incorporating the preceding changes we found improved our results (fixing β, changing the wavelength limits to match B11, sampling one data point per resolution element, updating the CH_4 and NH_3 opacities, and ignoring regions victim to poor order stitching), we allowed the cloud parameters to vary once again. Figure 3.21 shows the resulting TP profiles and posteriors in grey. The cloud parameters are unconstrained, except for a potential upper limit on the cloud volume mixing ratio. Other parameters are relatively unaffected, suggesting the inclusion of cloud opacity

has little impact. This lack of evidence for optically thick clouds in the atmosphere of U0722 are consistent with expectations for late T dwarfs (e.g. Kirkpatrick 2005) as well as other T dwarf retrieval studies at lower spectral resolution (e.g. Line et al. 2017; Zalesky et al. 2022).

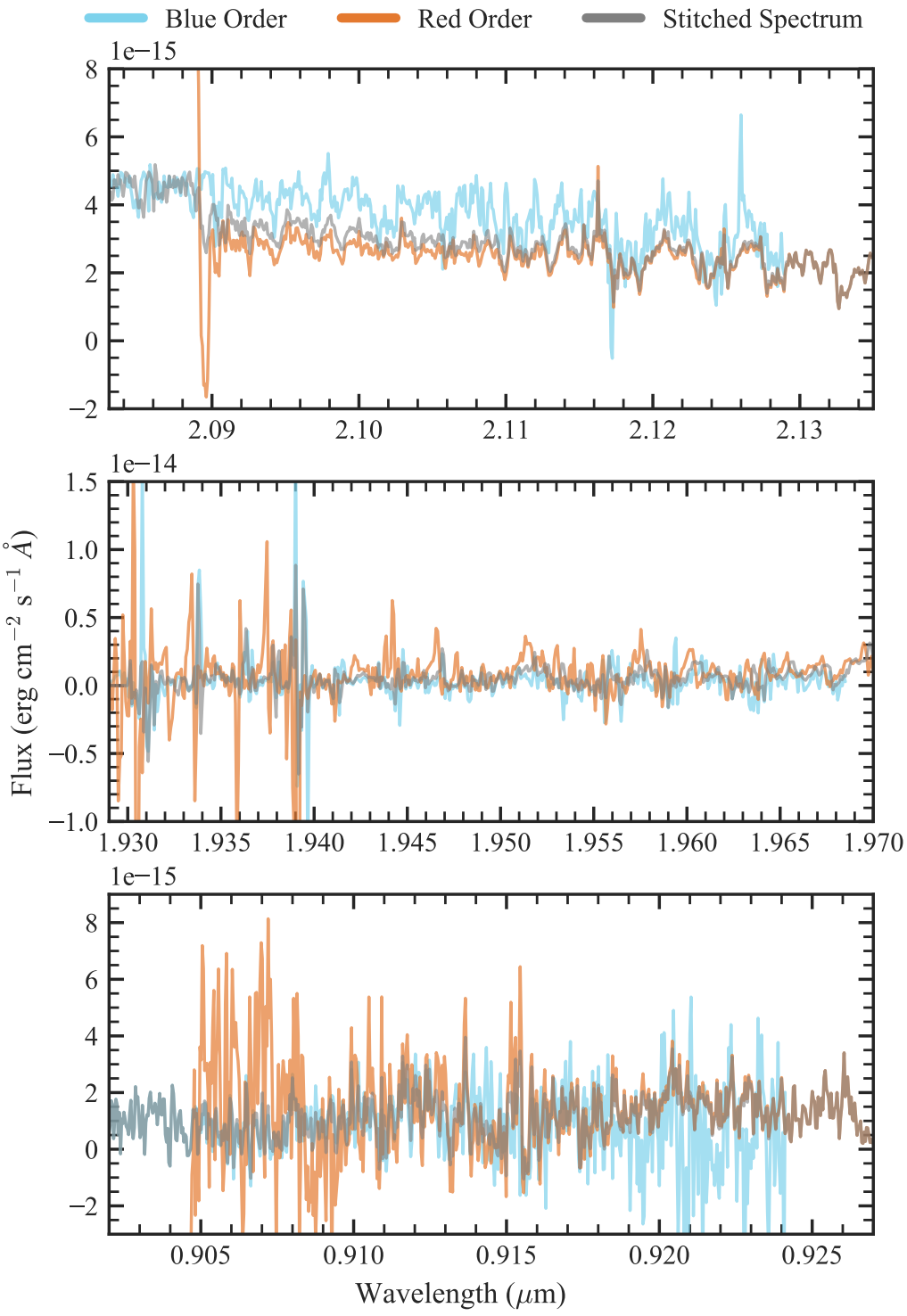

Figure 3.12: Example order overlap regions of the stitched FIRE spectrum (grey) that were removed due to issues with order stitching, compared to the component orders (blue and orange).

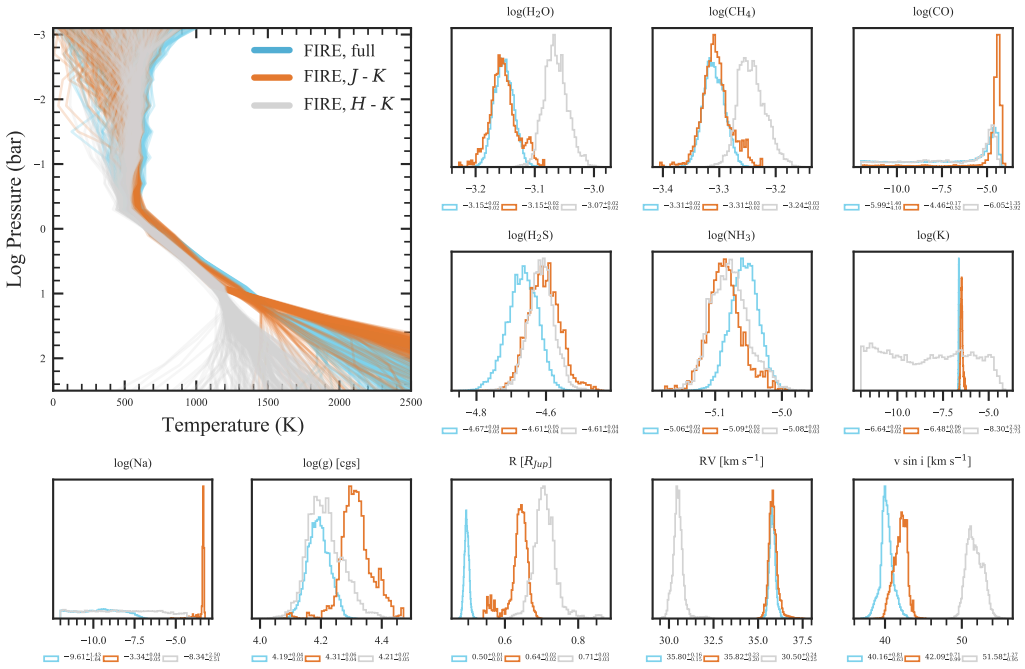

Figure 3.13: Effect on the retrieved TP profiles and selected posteriors when performing the retrieval on the full wavelength range, J-K, or just H and K bands.

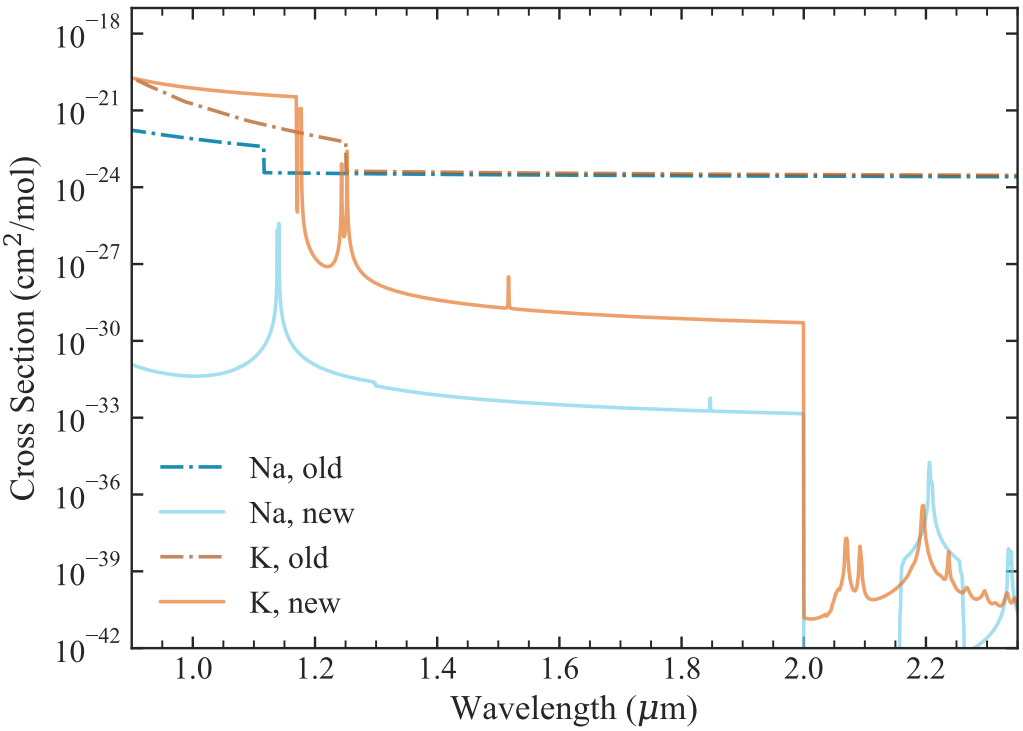

Figure 3.14: Comparison of old (dash-dot) and new (solid) alkali cross sections at 725 K and 1 bar, and smoothed to R $\sim$ 6000. The older alkali cross sections are from Freedman et al. (2014), while the newer ones are based on Allard et al. (2016) and Allard et al. (2019) for K and Na, respectively.

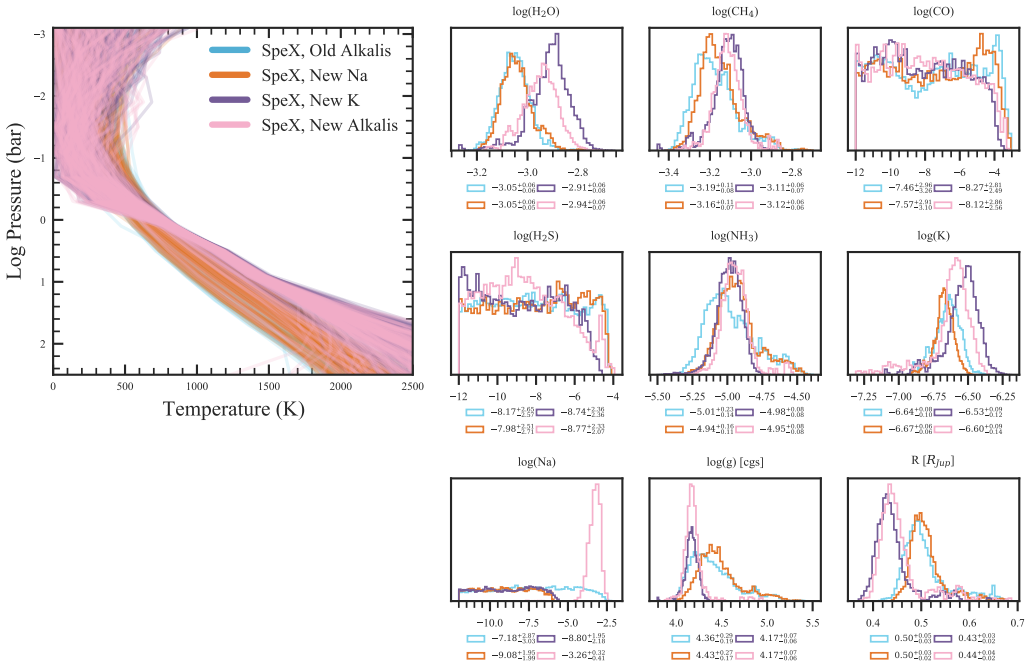

Figure 3.15: Effect of updating alkali cross sections on retrieved TP profiles and selected posteriors using the SpeX spectrum.

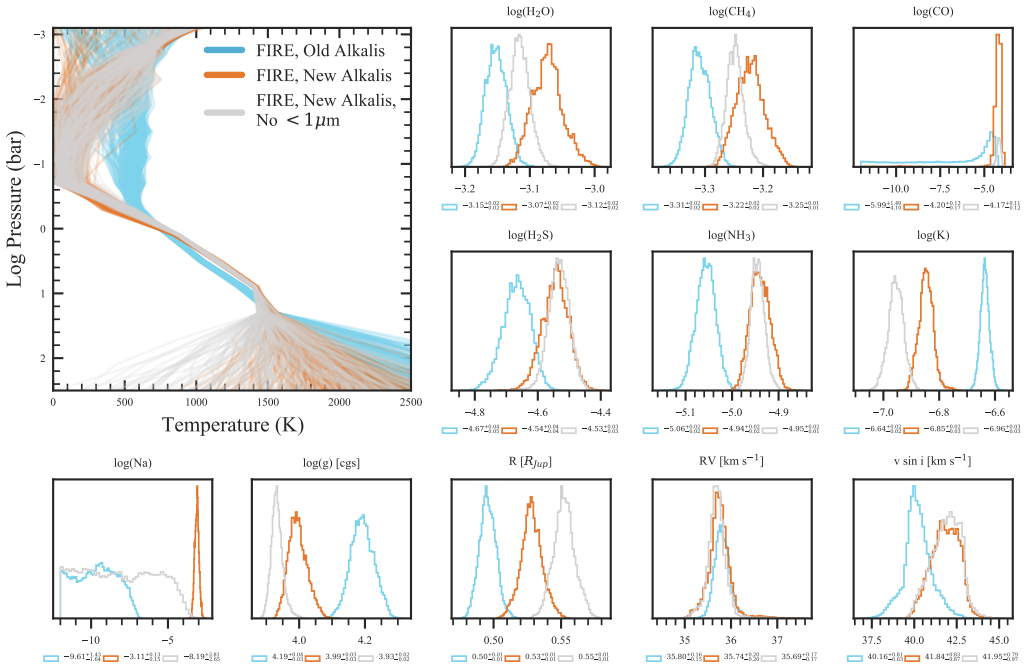

Figure 3.16: Effect on the retrieved TP profiles and selected posteriors for the FIRE spectrum when updating our alkali cross sections (orange). As our Na constraint appears to be only from a small snippet on the blue end of the FIRE spectrum, removing any data $< 1\mu$m leads to an unconstrained Na abundance (grey).

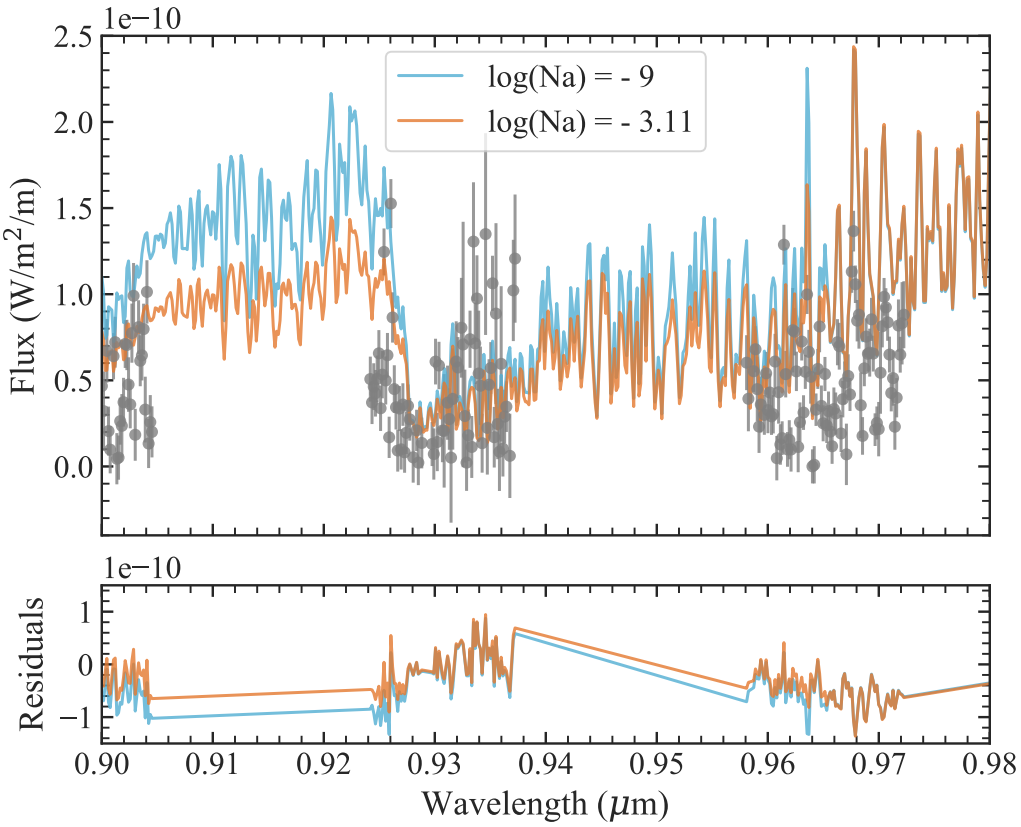

Figure 3.17: Model spectra from the median retrieved parameters, both using the new alkali cross sections, generated with and without the retrieved high Na abundance. This wavelength region is the only one where the increased Na abundance leads to a notable difference in the model spectra.

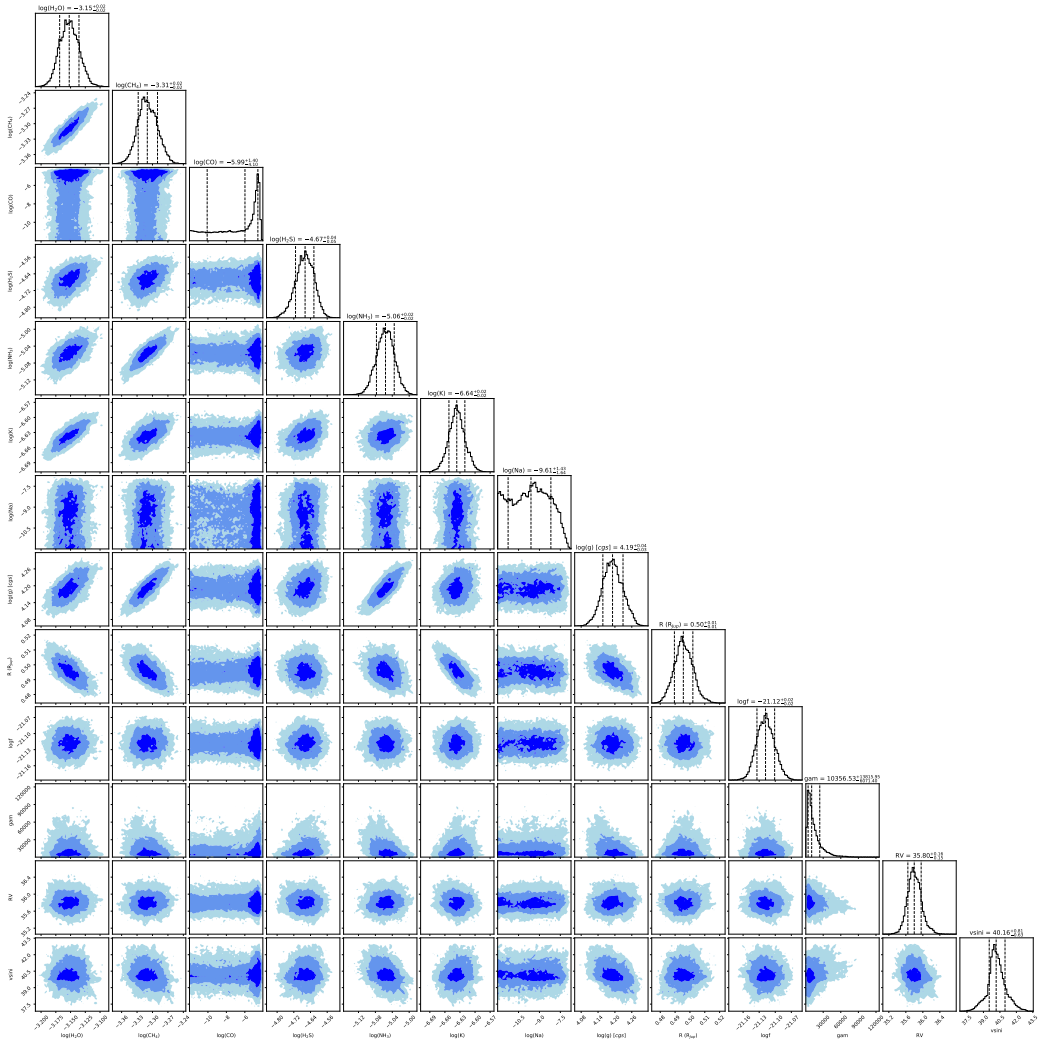

Figure 3.18: Corner plot summarizing the posterior of our preferred FIRE retrieval for the listed parameters. Correlations between parameters are shown in the two-dimensional histograms. Marginalized posteriors for each parameter are shown along the diagonal, with the dashed lines indicating the 16th, 50th, and 84th percentiles. The median and $\pm 1\sigma$ values for each parameter are shown above the histograms.

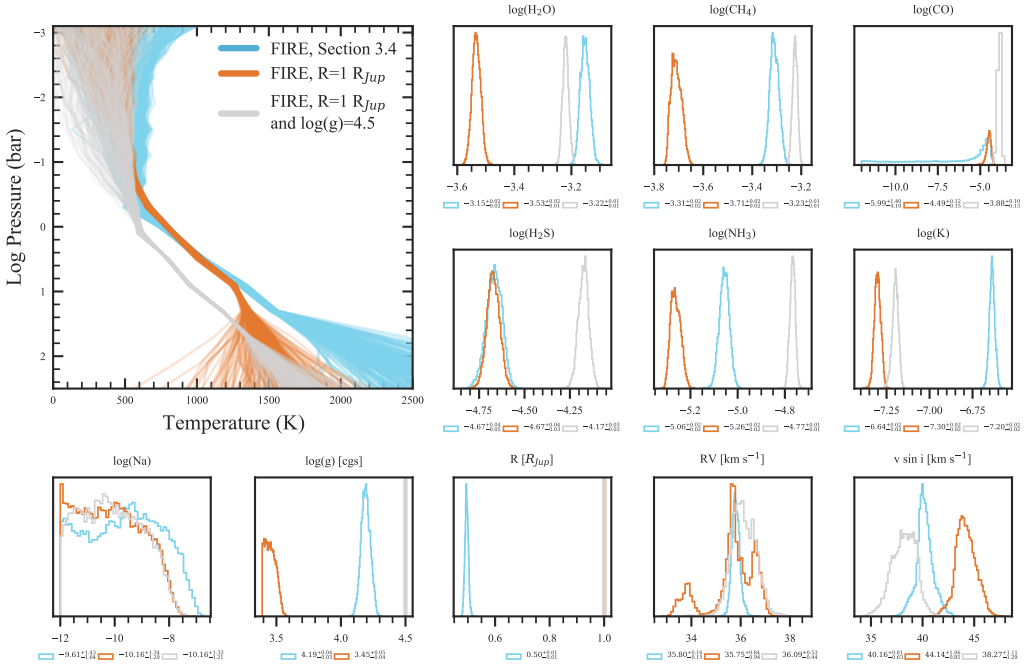

Figure 3.19: Effect on the retrieved TP profiles and selected posteriors of fixing the radius to 1 R_{Jup} (orange), and then setting the surface gravity to log(g)=4.5 as well. Almost all parameters are significantly affected.

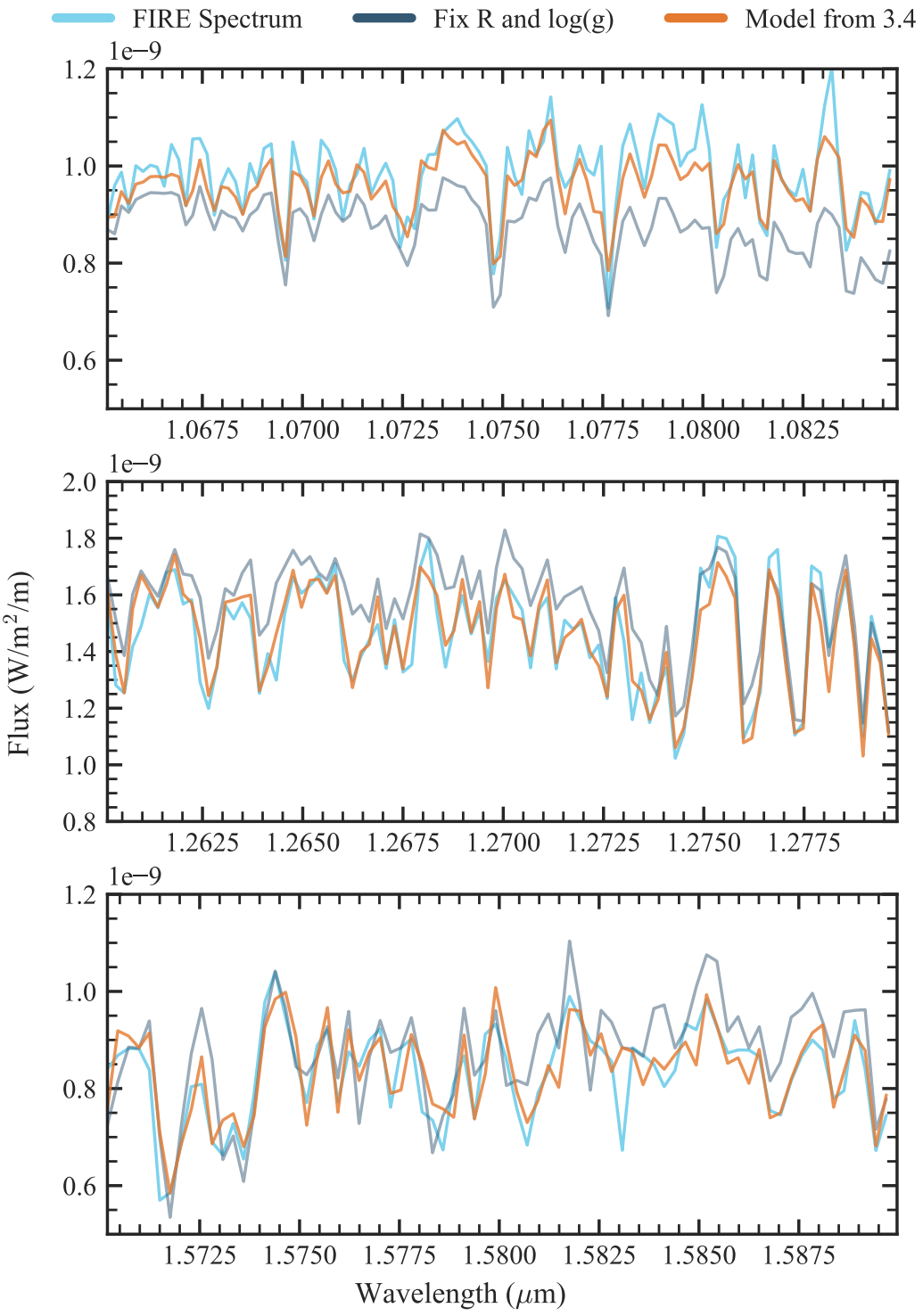

Figure 3.20: Select regions of the model spectrum from the median retrieved parameters when the radius and log(g) are fixed to 1 R R_{Jup} and 4.5, respectively, compared to the median model when both are allowed to vary (from Section 3.3.4) and the FIRE spectrum of U0722. The fit to the data is worse when the radius and gravity are not allowed to vary in the retrieval.

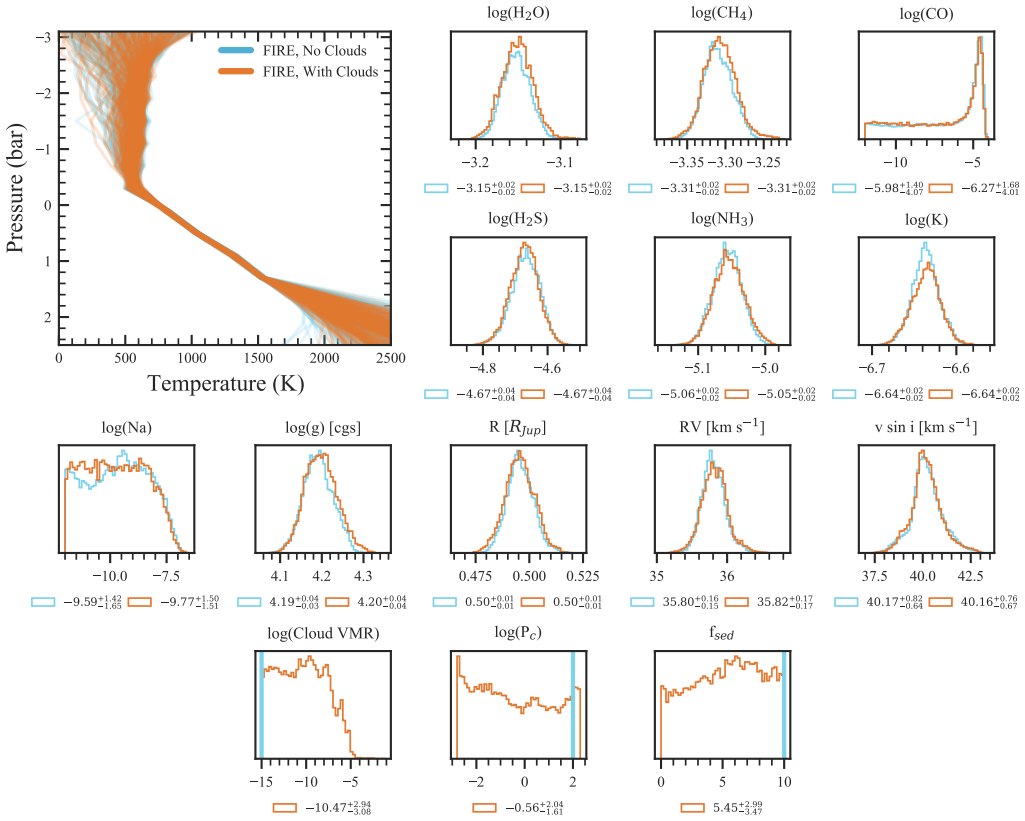

Figure 3.21: Effect on the retrieved TP profiles and selected posteriors of allowing the cloud parameters to vary (orange), instead of being fixed to values corresponding to optically thin clouds (blue). We find little evidence for optically thick clouds in the atmosphere of U0722.

3.4 Discussion and Conclusions

3.4.1 SpeX vs FIRE

We choose the FIRE retrieval from Section 3.3.4, with pieces of the spectrum affected by order stitching removed and all the preceding changes, as our "preferred" FIRE retrieval. While Sections 3.5 - 3.8 explore various other tests we performed, the retrieval from Section 3.3.4 uses the entire wavelength range while providing more physical constraints than those gained when using the new alkali opacities or fixing the radius for example. Table 3.4.1 lists each change to our retrieval framework we tested, the section of the paper where it is discussed, and whether or not it was applied for our preferred retrieval. Figure 3.22 shows the FIRE spectrum compared to the median model spectrum from the initial retrieval described in 3.3.1 and the median model spectrum from this final preferred FIRE retrieval. Red lines at the top of each panel indicate data points removed from our analysis due to spurious flux values and high telluric absorption (Section 3.3.1) or suspected problems with order stitching (Section 3.3.4). In Figure 3.22, the model from our final retrieval fits the FIRE spectrum much better than for our initial retrieval, particularly the peak of y band and the CH_4 features in H band, as discussed in Section 3.3.3. However, though the posteriors of the retrieved parameters are quite different, there are large sections of the spectrum where both models reproduce the observed spectrum relatively well, as should be expected for a data-driven model fitting method. Most of the tests of our framework outlined in Section 3.3, other than updating the line lists, were motivated by intuition or unphysical results rather than poor fits to the data. As such, we do not plot the median models from all our different

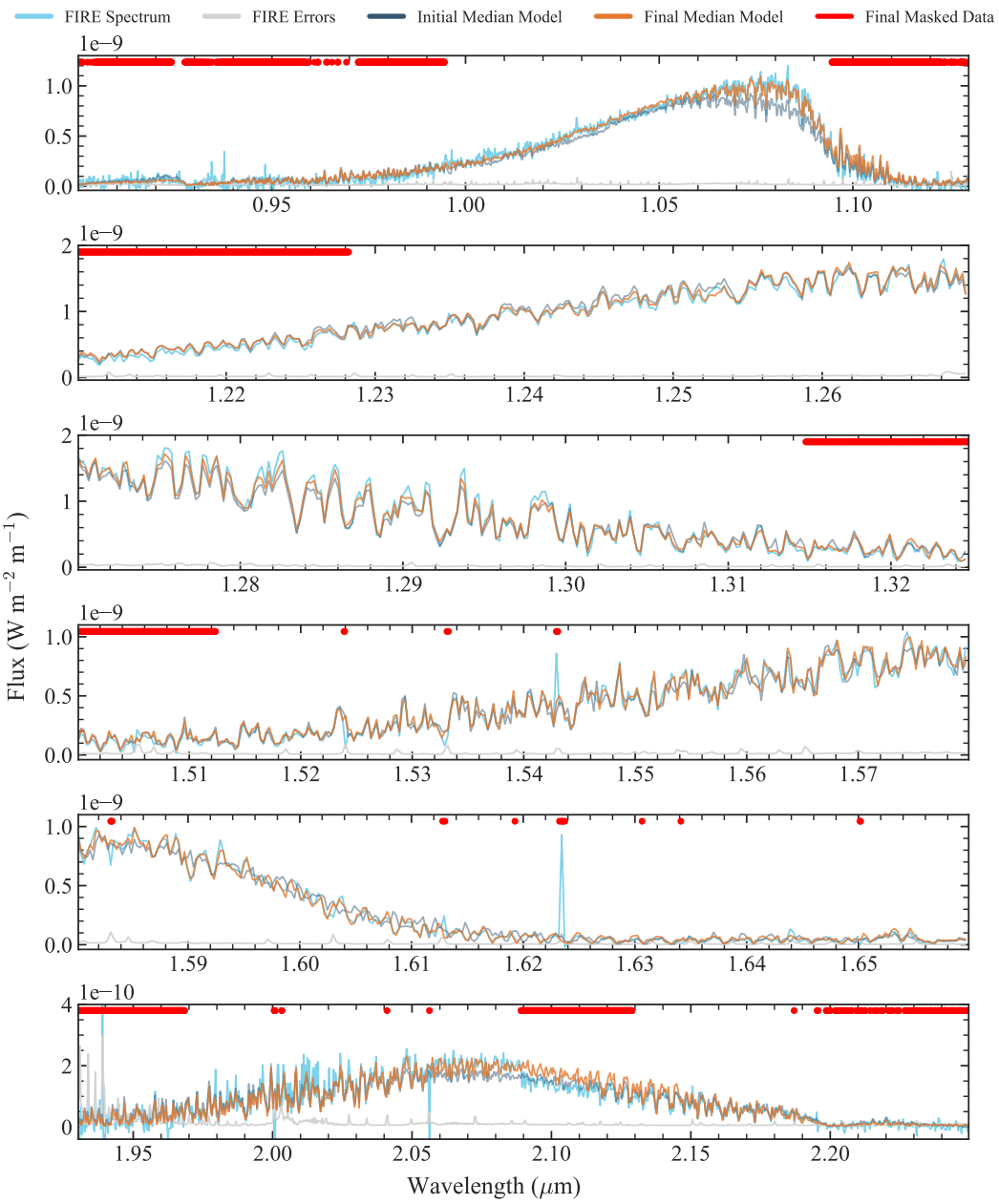

Figure 3.22: Comparison of the FIRE spectrum (light blue) with the median model of our initial retrieval (navy) and the median model of our "final" preferred FIRE retrieval from Section 3.3.4 (orange). The FIRE errors are shown in gray. Red lines at the top of each panel indicate sections of the FIRE spectrum that were removed from our final analysis as described in Sections 3.3.1, 3.3.2, and 3.3.4. Our final preferred median model spectrum does a better job fitting the FIRE data, particularly the peak of y band and the CH_4 features in H band.

retrieval runs in the interest of brevity and clarity.

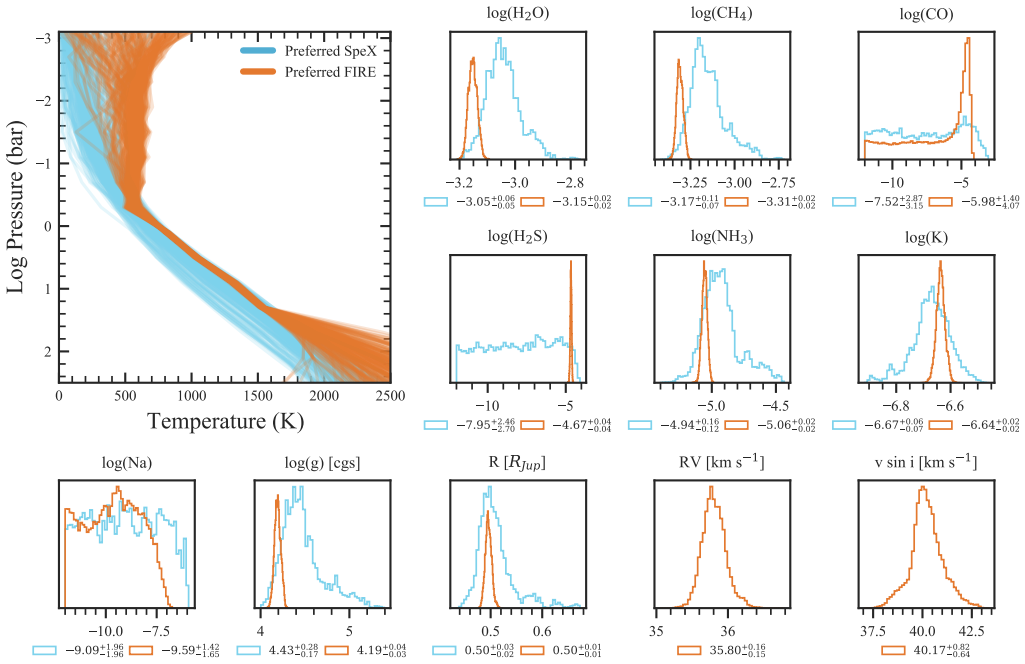

Figure 3.23: Retrieved TP profiles and selected posterior distribution for selected parameters for SpeX and FIRE spectra of U0722 after making the changes discussed in Section 3.3.

Figure 3.23 shows how much the constraints on our retrieved posteriors improve when using the R $\sim$ 6000 FIRE spectrum compared to the R $\sim$ 100 SpeX spectrum. The "preferred" SpeX retrieval here uses the same updated line lists as described in Section 3.3.3. The H_2O, CH_4, and NH_3 abundance posteriors with FIRE are $\sim$3-6$\times$ more precise than those from SpeX. Similarly, we can constrain the surface gravity to within about 0.04 dex, about 5$\times$ more precise than SpeX. Furthermore, between $\sim$0.5 to 20 bars, the TP profile is constrained within 100 K compared to the much wider 500 K spread for SpeX. Finally, our retrieval on the medium resolution FIRE spectrum allows constraints on parameters such as H_2S abundance, CO abundance, radial velocity, and

Table 3.3: Changes to our retrieval framework tested for application to the FIRE spectrum of U0722.

Change	Section	In preferred retrieval?
Add radial velocity and v sin i	3.2.2	yes
Mask regions of total telluric absorption	3.3.1	yes
Remove second T-P smoothing parameter	3.3.1	yes
Fix cloud parameters to optically thin values	3.3.1	yes
Limit data to 0.9-2.35 μm	3.3.2	yes
Take every 4th data point to not oversample the FIRE resolution element	3.3.2	yes
Update NH_3 and CH_4 opacities	3.3.3	yes
Mask data points affected by issues with orders stitching	3.3.4	yes
Limit analysis to subsections of the spectrum, J-K and H-K	3.3.5	no
Update alkali opacities	3.3.6	no
Fix radius to 1 R_{Jup}	3.3.7	no
Fix log(g)=4.5 and R = 1 R_{Jup}	3.3.7	no
Allow cloud parameters to vary	3.3.8	no

v sin i which are not constrained with the SpeX spectrum. However, while the preferred FIRE retrieval yields very precise constraints, they may not be accurate descriptions of the characteristics of U0722 and the uncertainties do not include any systematic effects, which we will discuss further below.

Table 3.4 lists physical parameters of U0722 for both retrievals, as well as from previous studies which will be discussed below. To calculate a number of these quantities and their uncertainties from the parameters in our retrieval framework, we take 5000 random samples of our posterior. With these precise constraints on the molecular abundances, we can consider the metallicity and C/O ratio as most of the metal content in these cool brown dwarf atmospheres is contained in H_2O and CH_4, with some contribution from CO and NH_3. We calculate these quantities from our retrieved

abundances following Equations 1 and 2 from Zalesky et al. (2022) and assuming solar abundances from Lodders (2010). To account for condensation processes that can deplete atmospheric oxygen, we multiply our H_2O abundance by 1.3 to better approximate the intrinsic metallicity and C/O as in Zalesky et al. (2022). Our retrieved abundances yield [M/H] = -0.10$^{+0.02}_{-0.02}$ dex and C/O = 0.54$^{+0.01}_{-0.02}$ from the FIRE retrieval, with ∼3-4× the precision than from the SpeX retrieval. For comparison, Zalesky et al. (2022) on average constrain [M/H] and C/O to within 0.2 dex with 50 T dwarf spectra at R∼100, although the precision varies among the objects. Though we have achieved precise constraints on these bulk properties, Calamari et al. (2022) carried out a retrieval study of GI 229B and showed the 1.3 oxygen scaling factor lead to a calculated C/O that was unexpectedly inconsistent with measurements of the primary star. They suggest better understanding of the potential oxygen sinks in brown dwarf interiors could refine the best way to connect measured atmospheric C/O to the bulk value.

For each sample of our posterior, we also generate a low-resolution spectrum over 0.3 to 250 μm, which we integrate and use to compute the bolometric luminosity L_{Bol} and effective temperature T_{eff}. Leggett et al. (2012) report a luminosity range of $\log(L_{Bol}/L_{Sun})$ = -6.05-6.17 from observed spectra of U0722 over ∼ 0.7 - 4 μm. The calculated $\log(L_{Bol}/L_{Sun})$ from the FIRE results of -6.23$^{+0.20}_{-0.09}$ is consistent with this literature value, but the luminosity from our SpeX results $\log(L_{Bol}/L_{Sun})$ = -6.42$^{+0.08}_{-0.05}$ is significantly lower. We also note that the luminosity constraints from the SpeX retrieval are more precise than those from the FIRE retrieval. While between 0.5 - 20 bars the TP profile is much better constrained by the FIRE retrieval, outside of this range the

temperatures vary considerably and are hotter than the corresponding SpeX values, leading to a calculated luminosity that is both higher and less well-constrained. The effective temperatures calculated from the luminosities and radius values unsurprisingly show the same behavior.

However, both our SpeX and FIRE retrievals do result in an unphysically small radius of about 0.5 R_{Jup}, potentially calling the accuracy of our other constraints into question. The parameter actually constrained by CHIMERA is the radius-to-distance scaling factor $(R/D)^2$; however, U0722 has a well-constrained distance from parallax measurements (4.12 ± 0.04 pc, Leggett et al. 2012) that is most likely not the source of our impossibly small radius. From the Sonora Bobcat evolutionary tracks (Marley et al. 2021), the minimum possible radius for even a 10 Gyr object at subsolar metallicity is 0.75 R_{Jup}. Furthermore, this small radius combined with our median retrieved $v \sin i$ would imply an unreasonably fast rotation period of about 1.55 hours. Figures 3.7 and 3.9 show this radius problem particularly gets worse when updating the CH_4 and NH_3 cross sections which are necessary to accurately reproduce the line positions seen in the FIRE spectrum. One potential source of error could be the completeness of the Hargreaves et al. (2020) CH_4 line list in y band as discussed in Section 3.3.5. Furthermore, even with the previously used Yurchenko & Tennyson (2014) line list we were retrieving a smaller radius than expected (0.76 R_{Jup}), indicating additional issues that are perhaps only exacerbated by the change to the newer CH_4 line list.

Further work is needed to assess whether our small radius could be attributed to completeness issues with the CH_4 line list from Hargreaves et al. (2020), uncertainties

Table 3.4: Parameters of U0722 calculated from this work and previous studies.

Parameter	FIRE Retrieval (this work)	SpeX Retrieval (this work)	BT-Settl Model Grid Fit Bochanski et al. (2011)	Tuned ATMO Model Grid Fit Leggett et al. (2021)
Wavelength Range (μm)	0.9 - 2.35	0.9 - 2.35	0.9 - 2.35	0.6 - 5.1
Spectral Resolution	6000	100	6000	180-500[f]
log(g) (cgs)	$4.19^{+0.04}_{-0.03}$	$4.43^{+0.28}_{-0.17}$	$4.0^{+0.3}_{-0.3}$	4.5
Radius (R_{Jup})	$0.5^{+0.01}_{-0.01}$	$0.5^{+0.03}_{-0.02}$	$1.14^{+0.46}_{-0.33}$ [a]	1.12[g]
Distance (pc)	Fixed at 4.12	Fixed at 4.12	4.6 (restricted)[b] 49 (unrestricted)	Fixed at 4.12
Mass (M_{Jup})	$1.5^{+0.1}_{-0.1}$	$1.9^{1.2}_{-0.6}$	5.24[c]	15[g]
C/O	$0.54^{+0.01}_{-0.02}$	$0.55^{+0.08}_{-0.06}$	0.55[d]	0.55[h]
[M/H] (dex)	$-0.10^{+0.02}_{-0.02}$	$-0.02^{+0.07}_{-0.06}$	0.0[d]	0.0[h]
$\log(L_{Bol}/L_{Sun})$	$-6.23^{+0.20}_{-0.09}$	$-6.42^{+0.08}_{-0.05}$	-6.11 (restricted)[e] -5.52 (unrestricted)	-5.99[e]
T_{eff} (K)	711^{+84}_{-35}	638^{+32}_{-15}	500^{+50}_{-50} (restricted) 700^{+50}_{-50} (unrestricted)	540

[a] Calculated from reported log(g) and mass.

[b] Bochanski et al. (2011) perform two fits, one with distance as a free parameter and one where the model-derived distance must be within 5σ of the parallax measurement from Lucas et al. (2010).

[c] Determined from evolutionary models of Baraffe et al. (2003) and the best fit T_{eff} and log(g).

[d] Considered models from the BT-Settl model grid (Allard & Freytag 2010) assuming solar metallicity and C/O using solar abundances from Asplund et al. (2009).

[e] Calculated from radius and T_{eff}.

[f] Used flux-calibrated SED with datasets from multiple instruments published by Lucas et al. (2010); Leggett et al. (2012); Miles et al. (2020).

[g] Determined from evolutionary models of Phillips et al. (2020).

[h] Considered models from the ATMO grid (Phillips et al. 2020) assuming solar C/O and with [M/H] = -0.5, 0.0, and +0.3 dex using solar abundances reported by Asplund et al. (2009) and updated by Caffau et al. (2011).

on how to treat alkali opacities, poor photometric calibration, or some other unseen flaw in our modeling framework. Recently, multiple retrieval studies have found radii smaller than expected from evolutionary models for both L dwarfs (Gonzales et al. 2020; Burningham et al. 2021; Xuan et al. 2022) and T dwarfs (Kitzmann et al. 2020; Lueber et al. 2022) across different retrieval frameworks and instruments with varying spectral resolutions. Furthermore, Y. Zhang et al. (2021a) performed a uniform comparison of 55 late T dwarf spectra with the Sonora Bobcat grid (Marley et al. 2021) of forward models using the Bayesian framework Starfish, finding small radii for a number of the studied objects indicating this issue is not solely found in retrieval analyses. Notably, Y. Zhang et al. (2021a) fit a SpeX spectrum of U0722, getting T_{eff}= 680 ± 26 K, log(g)=3.6 ± 0.3 dex, [M/H]= -0.06 ± 0.2 dex, and R = 0.43 ± 0.04 R_{Jup}, yielding even more unphysical values of the surface gravity and radius than in this work. More retrieval studies for large samples of brown dwarf spectra, particularly including mid-infrared data for the coolest objects and high-quality observations from JWST, will hopefully illuminate the source of this small radius problem. In addition, the growing sample of transiting brown dwarfs from the TESS mission (e.g. Šubjak et al. 2020; Carmichael et al. 2022) can provide independent tests of the radii predicted by evolutionary models, though their irradiated nature may cause difficulty in making comparisons.

3.4.2 Comparison to Bochanski et al. Results

We can compare the results from our preferred retrieval on the FIRE spectrum of U0722 to the original analysis of the dataset presented by B11. By comparing the spectrum to line lists, they were able to identify features of H_2O, CH_4, and NH_3, as

well as broad absorption from K. Similarly, we are able to place constraints on the abundances of all of these species to within ± 0.02 dex, indicating the impact of these species on the spectrum even if the retrieved abundances are not exactly accurate. In addition, we are also able to constrain the H_2S abundance due to a few distinct H_2S features in the spectrum (see Section 3.3.3) unidentified in the previous study.

B11 fit the FIRE spectrum of U0722 with BT-Settl models of Allard et al. (2011) based on the fitting procedure outlined by Cushing et al. (2008). The large differences we see in retrieved posteriors when looking at subsections of the spectrum in Section 3.5 reflect similar variance across the model fits of B11 of data in different bandpasses. However, the authors find significant differences between the best fitting models and the data in many places across the spectrum. Furthermore, there are notable discrepancies in our retrieved physical values from those of B11 when considering their full spectrum fit (most analogous to our results) as shown in Table 3.4. While their log(g) $4.0^{+0.3}_{-0.3}$ is consistent, they report a larger mass of 5.24 M_{Jup} from evolutionary models, indicating a much larger radius value of $1.14^{+0.46}_{-0.33}$ R_{Jup}. Due to the large uncertainty on U0722's parallax at the time, B11 allow distance instead of the radius to vary when fitting the $(R/d)^2$ scaling factor. When allowing this distance to freely vary, their best fit to the entire spectrum also prefers a hotter object with effective temperature 700 ± 50 K, consistent with the calcualted T_{eff} from our FIRE retrieval but with a far larger distance than the literature value (49 pc vs. 4.12 pc). Our retrieval functionally achieves the same effect with a small $(R/d)^2$ scaling factor instead attributed to a small radius given the reliable parallax measurement. However, when the distance is required

to be within 5σ of the parallax measurement from Lucas et al. (2010), the authors get a much colder T_{eff} of 500 ± 50 K.

Finally, while their measured v sin$i$ of 40 ± 10 km s^{-1} agrees with our results, their radial velocity measurement of 46.9 ± 2.5 km s^{-1} is significantly higher than our result of 35.80 ± 0.15 km s^{-1}. Given that the radial velocity was measured in part with models using significantly older line lists for basically all molecules present in this object's spectrum, such an inconsistency is perhaps expected. Future work to calculate if an updated RV measurement would change the original determination by B11 of a thin disk Galactic orbit could provide interesting context to U0722's potential age and evolutionary trajectory, though the change in radial velocity may not be enough to matter. We use the tool Bayesian Analysis for Nearby Young AssociatioNs Σ (BANYANΣ, Gagné et al. 2018) to determine the probability of U722 being a member of any well-characterized young associations within 150 pc, inputting the previously measured proper motion (Faherty et al. 2009) and parallax (Faherty et al. 2012) as well as the radial velocity measured in this work. BANYANΣ gives a 99.9% likelihood that U0722 is a field brown dwarf. Furthermore, for both velocity parameters our reported precision from `emcee` is significantly higher than those reported for the measurements by B11. Both the radial velocity and v sin i were calculated by cross-correlating the 1.27 - 1.31 μm section of FIRE spectrum with a template, either a grid model spectrum or another observation of a T dwarf, which may or may not be a good fit to the data in question. In contrast, the log-likelihood based MCMC approach reported here both considers significantly more data points across the whole spectrum and has been shown

to produce smaller error bars than cross-correlation methods (Brogi & Line 2019).

3.4.3 Comparison to Grid Models

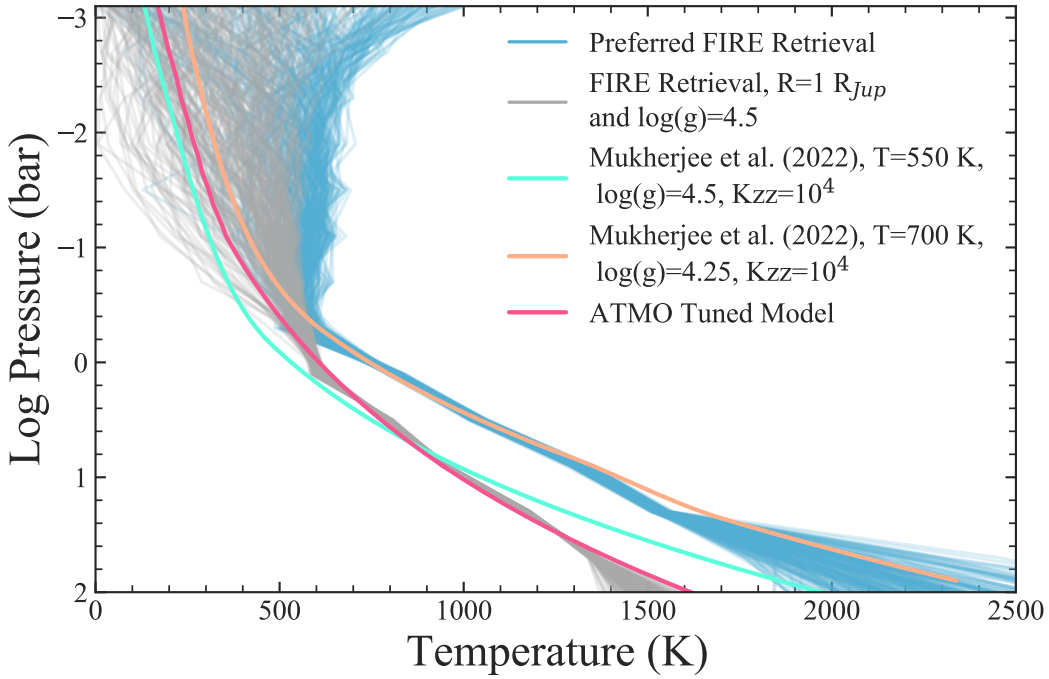

Figure 3.24: TP profiles from our preferred FIRE retrieval (blue) and the fixed radius and surface gravity retrieval (grey) to the tuned ATMO model (pink) and two disequilibrium forward models from Mukherjee et al. (2022). The tuned ATMO model is significantly colder than the retrieved TP profiles from our preferred FIRE retrieval, and has a different gradient in accordance with the adjusted adiabat discussed by Leggett et al. (2021). However, the retrieved TP profiles when fixing the radius and surface gravity to set values is in excellent agreement with the tuned ATMO model.

Given the many advances in line lists over the past decade, it is instructive to look at more recent comparisons of U0722 spectra with grid models. Miles et al. (2020) find that the low-resolution (R $\sim$ 300) M band spectrum of U0722 indicates disequilibrium amounts of CO from vertical mixing, consistent with our tentative detection of CO in the FIRE spectrum. Leggett et al. (2021) compare the flux-calibrated 0.6-5.1

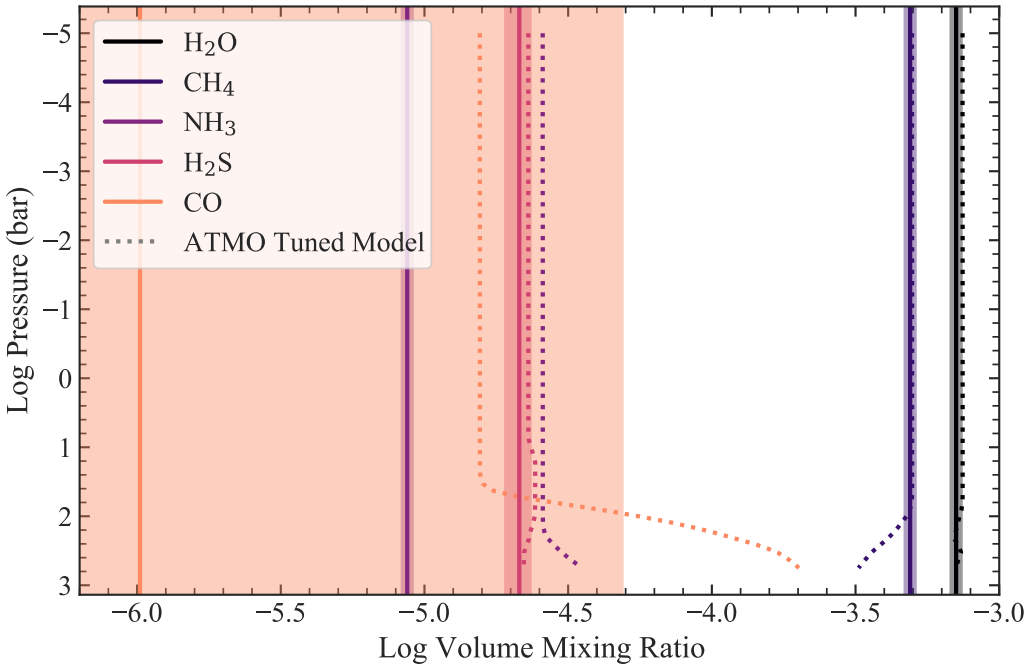

Figure 3.25: Molecular volume mixing ratios from the tuned ATMO model (dotted lines) as a function of atmospheric pressure compared to the median and 1σ posteriors from our FIRE retrieval (solid lines and shaded regions). With the exception of NH_3, the abundances are quite similar.

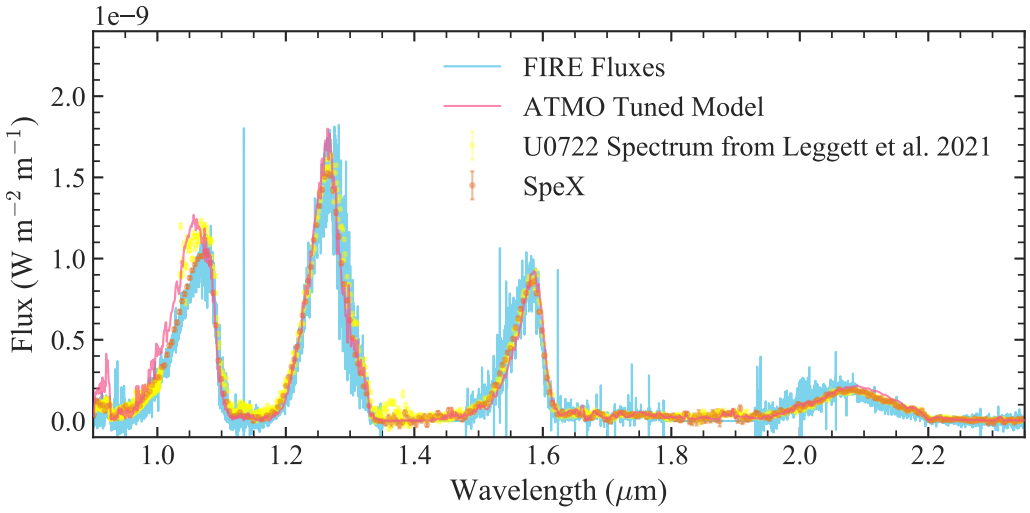

Figure 3.26: Comparison of the FIRE (blue) and SpeX (orange) spectra of U0722 analyzed in this work to the spectrum (yellow) and tuned ATMO model (pink) used in Leggett et al. (2021). There are notable discrepancies in the peak of the y band.

μm spectrum of U0722 created from multiple published observations (Lucas et al. 2010; Leggett et al. 2012; Miles et al. 2020) with the ATMO 2020 grid of models, finding that the models with and without disequilibrium chemistry still have trouble fitting the data well. The authors improve this fit by "tuning" the gradient of the TP profile away from the standard adiabat. As such, we compare our retrieved results to this adiabat-adjusted model in Table 3.4, which has an effective temperature of 540 K, log surface gravity (cgs) of 4.5, solar metallicity, log Kzz (cm^2 s^{-1})=7, and an adiabatic index of 1.27.

Figure 3.24 shows our retrieved TP profiles from the FIRE spectrum of U0722, compared to the abundances of the tuned ATMO model (Tremblin 2021, private communication), as well as two forward grid models with disequilibrium chemistry from Mukherjee et al. (2022). The tuned ATMO TP profile has a steeper gradient than either of the other grid models, reflecting the adjusted adiabat. Our retrieved TP profiles from the preferred FIRE retrieval are significantly hotter than that of the tuned ATMO model, more closely resembling that of a hotter 700 K object from the Mukherjee et al. (2022) grid, consistent with our calculated T_{eff}. The difference in temperature is consistent with the differences in radii- the tuned ATMO model assumed a radius of 1.12 R_{Jup} from the evolutionary models of Phillips et al. (2020), more than double that of our retrieved value. Thus, a cooler object would be necessary to achieve a similar amount of flux. In fact, when we fixed the radius to 1 R_{Jup} and surface gravity to log(g)=4.5, as discussed in Section 3.3.7, the retrieved TP profiles are consistent with the tuned ATMO model as shown by the grey curves in Figure 3.24. This agreement is reasonable, as

Leggett et al. (2021) similarly set R and log(g) to values from evolutionary model before tuning the TP profile to match the observed data.

Figure 3.25 compares our retrieved molecular abundances, shown by the solid lines and shaded 1σ regions, to the mixing ratios in the tuned ATMO model as a function of pressure in the atmosphere. Unlike the tuned ATMO model which assumes disequilibrium chemistry governed by the eddy diffusion parameter $\log(K_{zz})$, our volume mixing ratios for each species are allowed to vary independently and are not tied to one another by any assumptions or parameterizations of the chemical timescales involved. Our retrieved values for CO, CH_4, and H_2S are all in agreement with the ATMO abundances above 100 bars, and our H_2O value posterior is only 0.003 dex away from the ATMO model value. However, our NH_3 posterior is $\sim$0.5 dex lower, perhaps reflecting the differences in effective temperature and surface gravity between our retrieval results and the tuned ATMO model. Given a measured CO abundance, we can estimate $\log(K_{zz})$ by comparing to chemical equilibrium abundances from the Sonora Bobcat structure models (Marley et al. 2021) of similar T_{eff} and log(g) as described by Miles et al. (2020). Since our CO abundance has large uncertainties, our results could imply no vertical mixing for the lowest amount of CO up to $\log(K_{zz}) \sim 3.3$ cm^2 s^{-1} for the maximum amount of CO. The comparatively larger $\log(K_{zz}) = 7$ cm^2 s^{-1} from the tuned ATMO model is needed to get a similar CO abundance for a much colder object with higher surface gravity. While our retrieved surface gravity and radius are unphysical, our molecular abundances are plausible and mostly consistent with grid model predictions. The similarity in molecular abundances is also reflected in the consistency

of the C/O ratios and metallicities reported in Table 3.4.

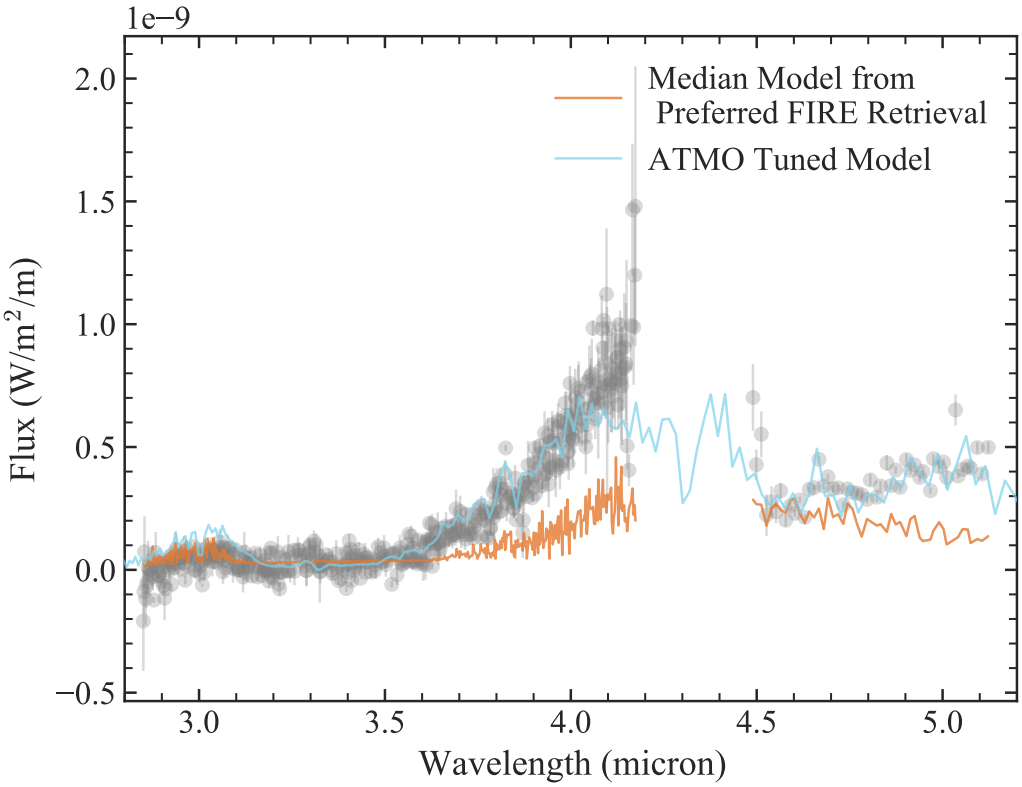

Figure 3.27: Comparison of the median model of our preferred FIRE retrieval and the ATMO tuned model to the L and M band spectra included in the analysis of Leggett et al. (2021). The FIRE retrieval clearly does not reproduce the measured flux of U0722 at longer wavelengths, whereas the ATMO tuned model gets closer at matching the observed slopes of these regions of the spectrum.

Differences in the data considered perhaps help explain why our retrieval prefers a hotter, smaller object than the tuned ATMO model when the retrieval is solely driven by the data (rather than any assumed radius or gravity value). We note that the NIR portion of the U0722 spectrum used in Leggett et al. (2021) is slightly inconsistent with that of the FIRE and SpeX spectra examined in this work. Figure 3.26 shows all three datasets, as well as the tuned ATMO model; the peak y band flux in

particular of the Leggett et al. (2021) is offset in both strength and wavelength. While the source of this discrepancy is unclear, it undoubtedly contributes to differences in our fitted or retrieved values for U0722. However, a more important distinction is the inclusion of longer wavelength data for U0722 in the analysis of Leggett et al. (2021).

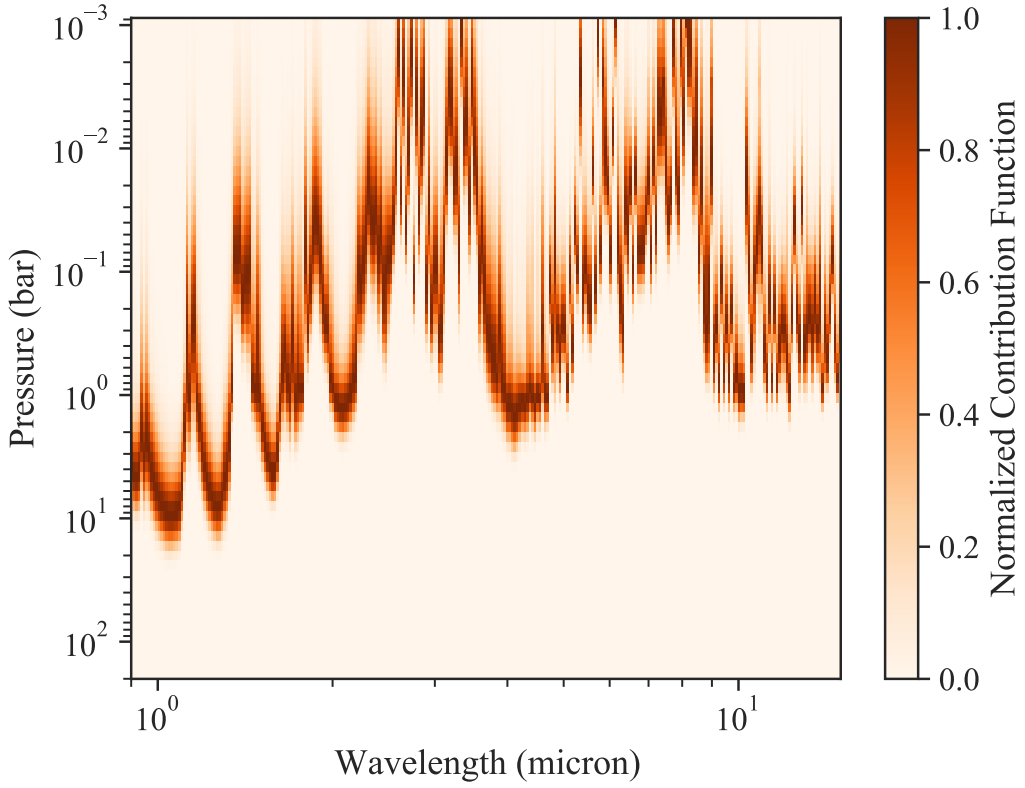

Figure 3.28: Normalized contribution functions for a model generated from the median results of preferred FIRE retrieval (which covered 0.9-2.5 μm) extrapolated out to longer wavelengths.

The authors included L and M band spectra from Leggett et al. (2012) and Miles et al. (2020), respectively. Figure 3.27 shows these datasets compared to the median model from our preferred FIRE retrieval extrapolated out to these wavelengths, as well as the tuned ATMO model. Our model clearly underpredicts the observed flux

of U0722 and does not reproduce the observed slope in the M band data. Figure 3.28 shows the normalized contribution functions for a model using the median parameter values from our preferred FIRE retrieval, generated at lower resolution and out to ~ 15 μm. The L and M bands probe the upper atmosphere, and we note that if we were to perform a retrieval on these datasets we would need to extend the atmosphere in our radiative transfer model to pressures below 10^{-3} bars, the current top of the atmosphere in this framework. Notably, the TP profile from our preferred FIRE retrieval is not well constrained at these low pressures in our retrieval, perhaps contributing to the model's failure to reproduce these data points. Furthermore, the discrepancy in M band could be due to less CO present in the median model than is needed to fit the data, as it is a major opacity source in this wavelength region. Figure 3.25 shows that the median CO abundance from our preferred FIRE retrieval is more than a dex less than the amount of CO in the tuned ATMO model. In combination with the unphysically small radius, the inability of our preferred FIRE retrieval to produce fluxes in accordance with longer wavelength observations points to our precise constraints on the atmosphere of U0722 being inaccurate and not necessarily representative of the true physical properties of this object. Future work on combining medium-resolution spectra with broader wavelength coverage data at lower resolution may provide further insight into the best way to obtain more plausible results from an atmospheric retrieval analysis.

3.5 Conclusions

In this work, we have applied the CHIMERA atmospheric retrieval framework to a high signal-to-noise, medium-resolution (R $\sim$ 6000) FIRE spectrum of a T9 dwarf. Key takeaways from this work are as follows:

1. *Limitations of the dataset must be taken into account*: In Section 3.3.2, we show that ensuring only one data point per resolution element is sampled as well as cutting out very noisy regions of data at either end of the spectrum can affect our retrieved posteriors. More dramatically, areas of the spectrum where orders were stitched poorly can negatively bias the retrieval analysis as discussed in Section 3.3.4. Future improvements to order stitching methods, or new ways to account for potential stitching issues within a retrieval framework, could help alleviate this problem in future analysis of data from echelle spectrographs.

2. *Using different opacity sources may lead to very different results*: Updating the line lists for CH_4 and NH_3 to those from Hargreaves et al. (2020) and Coles et al. (2019), respectively, greatly improved the ability of the forward models to match the line positions in the data, as shown in Figure 3.8. Almost all retrieved posteriors were affected by this change, even for the retrieval on the R $\sim$ 100 SpeX spectrum as shown in Figures 3.7 and 3.9. For example for the FIRE retrieval, changing the line lists lead the median abundances of H_2O and CH_4 to increase by $\sim$ 0.3 dex and the surface gravity log(g) to increase by $\sim$0.4 dex. However, the updated line lists also resulted in a radius decreased by about 30% to an unphysical 0.5 R_{Jup}. We also tested different treatments of Na and K opacities

in Section 3.3.6, again finding largely disparate results depending on which cross sections were used. While we do recommend the Hargreaves et al. (2020) CH_4 line list due to its ability to match the line positions in our FIRE spectrum, more comparison with other line lists with regards to completeness as well as treatment of the alkali wings are needed to fully utilize this kind of high-quality data.

3. *Medium-resolution retrievals offer very precise constraints, but they may not be accurate*: As shown in Figure 3.23, the constraints on the temperature-pressure profile and abundances from our FIRE retrieval of U0722 are significantly more precise than those from the SpeX spectrum. In particular, we are able to retrieve the abundances of H_2S and tentatively CO which is not possible with the lower resolution spectrum. However, while we do get these precise, stellar-like constraints on atmospheric abundances ($\sim$0.02 dex), the radius is far too small to be physically plausible. This small size is in accordance with our retrieved TP profile being hotter than previous analyses of this object, yielding a similar overall observed flux. Thus, this study joins a growing number of modeling analyses of brown dwarf spectra that have yielded smaller radii than allowed by our understanding of brown dwarf evolution. Furthermore, extrapolating a median model from our retrieval cannot to L and M band cannot reproduce observations of U0722 at these wavelengths, indicating the constraints from the medium-resolution FIRE spectrum alone do not accurately describe the conditions of this object.

This work is a first foray into the challenges and benefits of applying atmospheric retrieval tools to medium-resolution spectra of brown dwarfs. With the launch

of JWST and future ground-based studies, more work is needed to assess how we can improve our current modeling frameworks to address these challenges and unlock the potential for trustworthy, precise constraints on substellar atmospheres from retrievals of medium-resolution spectra.

Chapter 4

High-Precision Atmospheric Constraints for a Cool T Dwarf from JWST Spectroscopy

The following work will soon be submitted to Nature Astronomy; as a result, this chapter is organized differently than the preceding chapters in accordance with the journal's submission guidelines.

4.1 Introduction

Brown dwarfs, intermediate in mass between gas giants and low-mass stars, act as critical tests of our knowledge of substellar atmospheres. Since brown dwarfs and directly imaged exoplanets span a similar range in effective temperature (Faherty et al. 2016), understanding the emergent spectra of brown dwarfs can inform our inter-

pretation of planetary spectra. Comparison of observed brown dwarf spectra to grids of forward models allow us to assess our understanding of the dominant processes that sculpt the atmosphere. For example, stronger or weaker features from molecules like CO and NH3 than expected in chemical equilibrium have been observed for a number of brown dwarfs (e.g., Saumon et al. 2007; Miles et al. 2020), demonstrating the need for including vertical mixing in models to accurately describe these atmospheres.

Data-driven Bayesian inverse or "atmospheric retrieval" methods have allowed for abundance measurements for a number of important molecules like H_2O, CH_4, CO, NH_3 (e.g., Line et al. 2017; Burningham et al. 2017). Metallicities and elemental ratios like C/O can be calculated from these measured abundances, which when measured for a range of objects can be used to inform our understanding of formation pathways of planets and brown dwarfs (Mollière et al. 2022). Isotopologue ratios also can provide additional leverage for distinguishing amongst potential formation scenarios of exoplanets and brown dwarfs, particularly with the launch of JWST and upcoming instruments on ELTs (Mollière & Snellen 2019; Morley et al. 2019). For example, the ratio of $^{12}CO/^{13}CO$ has been measured for three extrasolar objects, initially indicating enhanced ^{13}CO relative to solar for planetary bodies compared to brown dwarfs, potentially due to accretion of ices with enhanced ^{13}CO from beyond the CO snow line (Y. Zhang et al. 2021a,b; Line et al. 2021). Expanding the sample of objects with measured $^{12}CO/^{13}CO$ ratios could enable a greater understanding of planetary versus brown dwarf formation pathways.

However, significant challenges have arisen in fitting models to observed brown

dwarf spectra. Fundamental parameters from fitting grid models to observations can vary strongly with wavelength range considered or amongst differing model families (e.g., Tannock et al. 2022; Lueber et al. 2023). Similarly, grid model fitting and atmospheric retrievals can yield very different parameters such as when applied to the same set of observations (Z. Zhang et al. 2021; Zalesky et al. 2022). Furthermore, disequilibrium chemistry models required to reproduce observed features from carbon- and nitrogen-bearing molecules in T and Y dwarfs predict strong PH_3 features, which have so far not been detected (Morley et al. 2018; Miles et al. 2020; Beiler et al. 2023), potentially suggesting a need for revisions to our understanding of disequilibrium and phosphorous chemistry.

The effort to solve these discrepancies could benefit from observations with higher spectral resolution and signal-to-noise, particularly out to longer wavelengths where the strongest features from CO, CO_2, PH_3, and NH_3 are expected. As such, the recent launch of JWST (Rigby et al. 2023) represents the next frontier for atmospheric studies. Recently published observations of brown dwarfs with JWST's Near Infrared Spectrograph (NIRSpec, Jakobsen et al. 2022) and Mid Infrared Instrument (MIRI, Rieke et al. 2015) demonstrate the high signal-to-noise and information-rich spectra obtainable for these objects (Miles et al. 2023; Luhman et al. 2023; Beiler et al. 2023). The aim of this work is to see if the unprecedented quality of JWST observations can allow for precision abundance measurements in combination with isotopologue ratio constraints, in order to help disentangle the formation scenarios of stars, brown dwarfs, and planets.

We present NIRSpec observations with the G395H filter (∼2.9 - 5.2 μm, R ∼ 2700) of the T8 dwarf 2MASS 0415-0935. This is the first brown dwarf retrieval study on NIRSpec data at its maximum native resolution of R ∼ 2700. We also explore the effect of including lower resolution observations of the same object with SpeX at the NASA Infrared Telescope Facility (IRTF) and the Infrared Spectrograph (IRS) of the Spitzer Space Telescope. We use the same retrieval framework successfully applied for low-resolution spectra of brown dwarfs (e.g., Line et al. 2017; Zalesky et al. 2022) and recently modified for medium-resolution spectra (Hood et al. 2023) - see Methods for more details.

4.2 Results

4.2.1 Good agreement between retrieval model and G395H data

Figure 4.1 shows the observed NIRSpec/G395H spectrum compared to the best fit model spectra from our retrieval on solely the JWST data, as well as from the retrieval on all three data sets or the "full SED" retrieval. Both models fit the observed spectrum well, and show only minor differences across these wavelengths. With the JWST data alone, we constrain the abundances of H_2O, CH_4, CO, CO_2, and NH_3 to within ∼ 0.15 dex, as shown in Figure 4.2. We are also able to constrain the TP profile, surface gravity, radius, radial velocity, and the ratio of $^{12}CO/^{13}CO$ (discussed further below). The posterior for the H_2S abundance is not well-constrained, with a long tail out to low values. We only achieve an upper limit on the PH_3 abundance and do not identify any clear PH_3 features in the observed spectrum. The NH_3 abundance

constraint comes from a small feature around 3 μm, previously tentatively identified (Beiler et al. 2023) and confirmed in this work (see Methods for more information).

4.2.2 Effect of additional wavelength coverage

Figure 4.2 shows the retrieved TP profiles and posteriors of selected parameters for four retrievals on different combinations of data sets: JWST NIRSpec/G395H data alone, JWST plus Spitzer/IRS, JWST plus IRTF/SpeX, and the full SED retrieval. Adding in either the Spitzer or SpeX data yields more precise constraints that also shift slightly towards higher gravity and metallicity. The inclusion of the SpeX data provides more additional precision than that gained with Spitzer; including the Spitzer observations has little effect if the SpeX data are also included. Adding in extended wavelength coverage also yields tighter TP profile constraints in the deep atmosphere, particularly the SpeX data, reflective of the near-infrared probing the hottest temperatures and highest pressures. For the full SED retrieval, the TP profile is constrained within $\pm$ 35 K for $\sim$0.4 - 40 bars. Furthermore, including the SpeX data in our analysis allows us to consider the alkali abundances, yielding a bounded posterior for K and an upper limit of log(Na) $\lesssim$ -4.

We can extrapolate the best fit model from each retrieval over the wavelengths for the full data set for comparison to the observed data for 2MASS 0415-0935, as shown in Figure 4.3. For the JWST and JWST plus Spitzer retrievals, we assume the median alkali abundances from the full SED retrieval, as the modeled near infrared flux would be greatly overestimated without any alkali opacity. All four models are almost indistinguishable over the NIRSpec/G395H wavelengths, and only minor differences

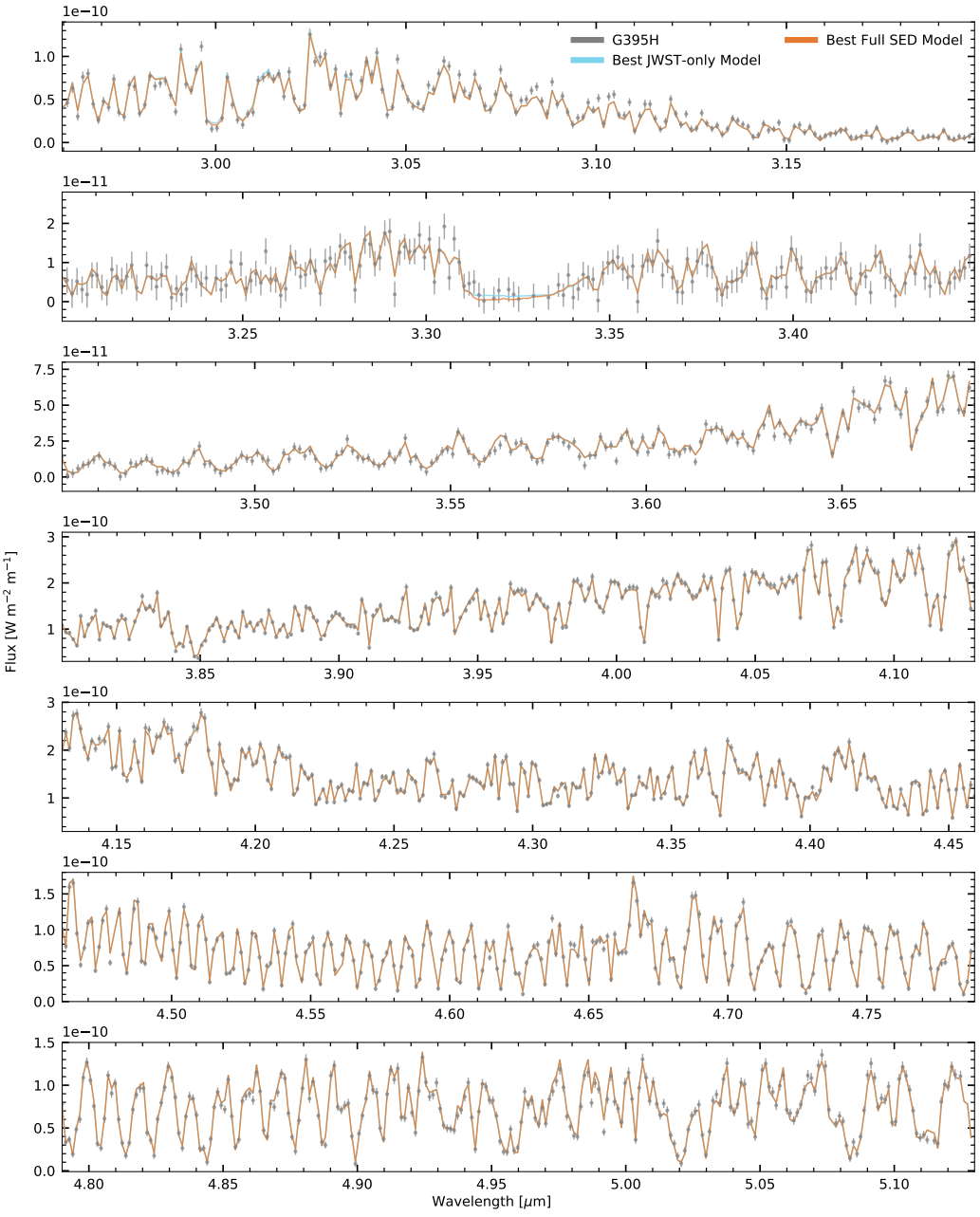

Figure 4.1: **Observed NIRSpec/G395H spectrum of T8 dwarf 2MASS 0415-0935 and the best-fit retrieval model.** The observed spectrum and error bars are shown in grey, the best-fitting model from a retrieval on just the JWST/NIRSpec data is shown in light blue, and the best-fitting model from a retrieval on all three datasets is shown in orange.

can be seen across the Spitzer/IRS region. The best fit models are most distinct in the near infrared, particularly in the peaks of y, J, and H band. These discrepancies are consistent with the strong effect the SpeX data has on the retrieved constraints shown in Figure 4.2. However, different assumed alkali abundances could potentially bring the JWST and JWST plus Spitzer models into better agreement with the observations.

4.2.3 Constraint on $^{12}C^{16}O/^{13}C^{16}O$

We include the $^{12}CO/^{13}CO$ isotopologue ratio as a free parameter in our retrieval model. We are able to get a bounded constraint on this ratio with the NIRSpec/G395H data, finding $^{12}CO/^{13}CO = 97.44^{+8.78}_{-8.32}$ for the retrieval on the full SED of 2MASS 0415-0935. To validate this constraint, we follow the methods of Y. Zhang et al. (2021a) and perform a full retrieval including ^{13}CO as well as a reduced retrieval without ^{13}CO. The best-fitting models of the full and reduced retrievals are shown in Figure 4.4a compared to the observed spectrum. We construct a ^{13}CO model by taking the difference between the best fit model of the full retrieval and the same model without ^{13}CO. The observational residuals of the reduced model are compared to this ^{13}CO model in Figure 4.4b; the residuals clearly overlap the ^{13}CO lines in multiple places. The cross-correlation function (CCF) between the residuals of the reduced model and the ^{13}CO model is shown in Figure 4.4c, as well as the scaled auto-correlation function (ACF) of the ^{13}CO model itself. The clear CCF peak at 0 km/s indicates a strong detection of ^{13}CO. We also calculated the Bayesian information criterion (BIC) of the best-fitting model for each retrieval to similarly determine if the inclusion of ^{13}CO is justified. The difference in BIC between the two models, ΔBIC = 357, indicates that

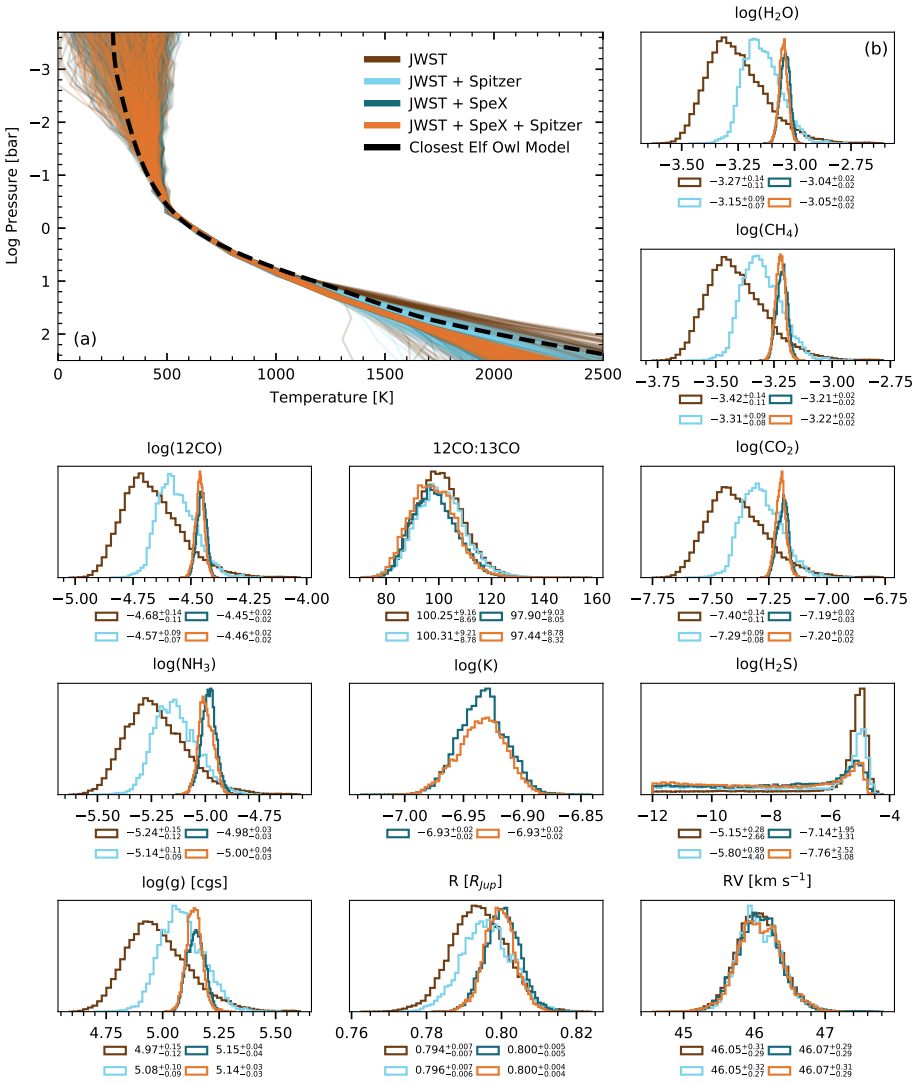

Figure 4.2: **Retrieval results for different combinations of observations of 2MASS 0415-0935.** (a) The retrieved TP profiles. The results from retrieving on the JWST/NIRSpec data only are in brown, JWST/NIRSpec and the Spitzer/IRS are in light blue, JWST/NIRSpec and the IRTF/ SpeX are in teal, and from including all three datasets are in orange. The black dashed line shows the TP profile from fitting the full SED to the Sonora Elf Owl grid (as discussed in Section REF). (b) The posterior distributions of selected parameters from each retrieval run, following the same colors as in panel (a). The legend lists the median value and 2σ uncertainties for each distribution. While the abundances of PH_3 and Na are also free parameters in our model, we only retrieve upper limits of log(PH_3) $\lesssim$ -7.5 for all cases and log(Na) $\lesssim$ -4 for the retrievals including the SpeX data.

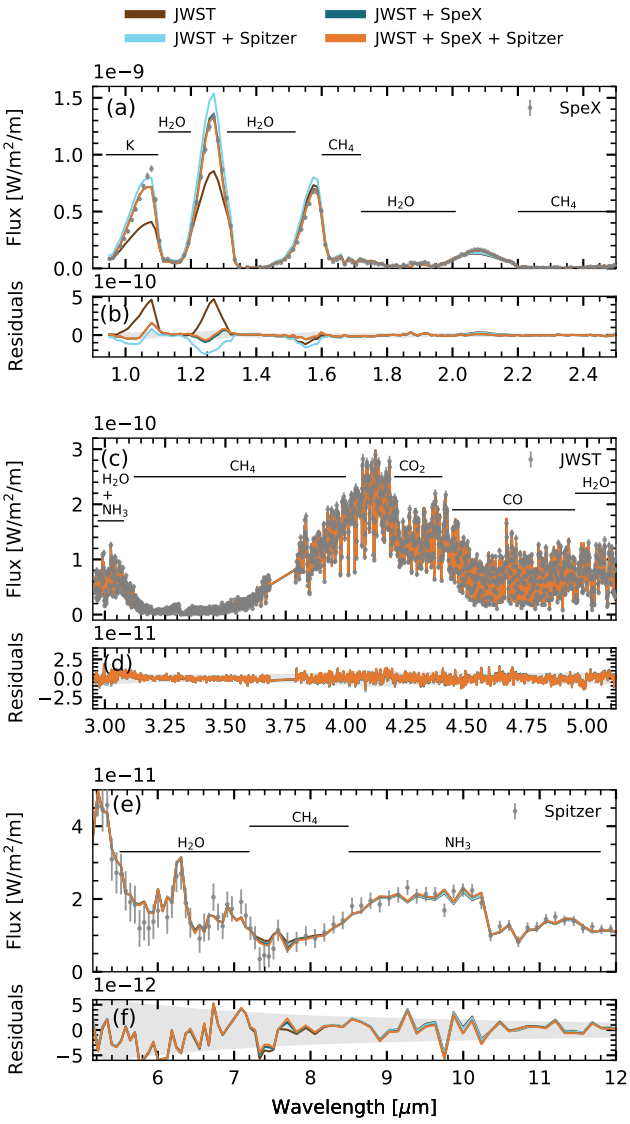

Figure 4.3: **Comparison of best retrieval models to IRTF/SpeX, JWST/ NIRSpec, and Spitzer/IRS observations of 2MASS 0415-0935.** (a), (c), (e) The models from each retrieval compared to the IRTF/SpeX, JWST/ NIRSpec, and Spitzer/IRS observations, respectively. The median models from retrieving on the JWST/G395H data only are in brown, JWST/G395H and the Spitzer/IRS are in light blue, JWST/G395H and the IRTF/SpeX are in teal, and from including all three datasets are in orange. While the Spitzer spectrum extends out to 20.5 μm, the models are indistinguishable past the wavelengths plotted here. (b), (d), (f) The model residuals from the IRTF/SpeX, JWST/NIRSpec, and Spitzer/IRS observations, respectively. The errorbars on the observed data are indicated by the shaded grey region.

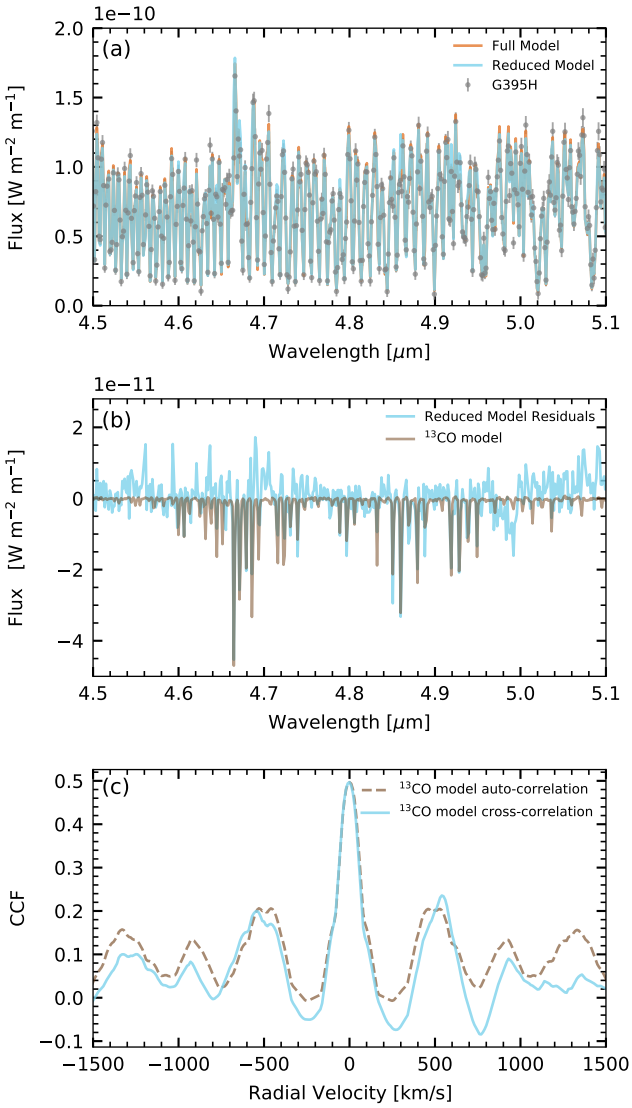

Figure 4.4: **CO features in JWST/NIRSpec (G395H) data and ^{13}CO cross-correlation detection.** (a) Portion of the G395H spectrum (grey data points) where CO is dominant, compared to the best fit model from a retrieval with both ^{12}CO and ^{13}CO in orange, and the best reduced model without ^{13}CO in blue. (b) Residuals for the reduced model from (a), compared to a ^{13}CO model (the difference between the best fit full model and the same model without ^{13}CO) in brown. The reduced model residuals clearly overlap with the ^{13} CO absorption lines. (c) The cross-correlation function between the reduced model residuals and the ^{13}CO model shown in blue. The auto-correlation function of the ^{13}CO model scaled to the peak of the cross-correlation function is shown by the brown dashed line.

including ^{13}CO is strongly preferred (ΔBIC > 10 indicates very strong evidence against the model with higher BIC; Kass & Raftery (1995)).

4.3 Discussion

4.3.1 Physical Parameters of 2MASS 0415-0935

We can calculate various additional physical parameters from our full SED retrieval results (see Methods), such as the bolometric luminosity L_{Bol}, effective temperature T_{eff}, mass, metallicity [M/H], and the C/O ratio, as listed in Table 4.1. Comparing our retrieved log(g) and calculated T_{eff} to the Sonora Bobcat evolution models (Marley et al. 2021) in Extended Data Figure 4.6, we can see our constraints are consistent with an age of 4.0 - 6.0 Gyr and a mass of $\sim$ 37 - 45 M_{Jup}.

Multiple previous studies have similarly studied the SED of 2MASS 0415-0935, albeit with different data sets and techniques. Table 4.1 additionally lists the calculated physical parameters from two such studies. Both Filippazzo et al. (2015) and Zalesky et al. (2022) find a lower effective temperature and larger radius than in the present work (though the error bars of Filippazzo et al. 2015 are significantly larger), which balance out to yield similar L_{bol}. While our retrieved radius is smaller than reported for 2MASS 0415-0935 in previous works, it does not decrease so much as to be physically implausible, an increasingly common issue in brown dwarf retrieval studies (e.g. Lueber et al. 2022; Hood et al. 2023). While Zalesky et al. (2022) get a very similar log(g) to our value, their slightly subsolar metallicity and markedly supersolar C/O are inconsistent with the constraints presented here. As the retrieval framework used in this work is a

modified version of that of Zalesky et al. (2022), these discrepancies possibly stem from differences in opacity data used or more likely just the inclusion of longer wavelength data with which we can probe a wider number of chemical species in the atmosphere.

4.3.2 Comparison to Grid of Forward Models

To further contextualize our results, we compare the results of our retrieval to the Sonora Elf Owl grid of forward models (Mukherjee et al. in prep) which includes the effects of disequilibrium chemistry. Chemical abundances in the visible atmosphere are governed by the interplay of chemical conversion and vertical mixing timescales - when the latter is shorter than the former, the species in question will be out of chemical equilibrium. For the Sonora Elf Owl models, the vertical mixing is parameterized with the vertical eddy diffusion coefficient K_{zz}, where a higher K_{zz} will lead to more vigorous mixing and a shorter mixing timescale. The strength of this vertical mixing can affect the abundances of many species considered in our retrieval, including H_2O, CH_4, CO, CO_2, NH_3, and PH_3.

We used a Bayesian grid fitting technique to compare all three datasets of 2MASS 0415-0935 to the Sonora Elf Owl grid (see Methods). The resulting constraints for the grid parameters are listed in Table 4.1. While the effective temperature and radius from the Sonora Elf Owl fit are similar to those from our full SED retrieval, the grid model fit prefers a significantly lower surface gravity, metallicity, and C/O. As shown in Extended Data Figure 4.6, the decreased gravity at this effective temperature implies a much younger ($\sim$0.4 - 0.6 Gyr) and less massive ($\sim$ 15 M_{Jup}) object when compared to Sonora Bobcat evolution models. The TP profile of the closest Elf Owl

Table 4.1: Parameters of 2MASS 0415-0935 calculated from this work and previous studies.

Parameter	Full SED Retrieval	Filippazzo et al. (2015)	Zalesky et al. (2022)	Sonora Elf Owl Fit
Wavelength Range (μm)	0.95 - 20.5	0.76 - 7.59[a]	0.95 - 2.5[b]	0.95 - 20.5
log(g) (cgs)	$5.14^{+0.03}_{-0.03}$	$4.83^{+0.51}_{-0.51}$	$5.10^{+0.15}_{-0.25}$	$4.51^{+0.02}_{-0.01}$
Radius (R_{Jup})	$0.800^{+0.004}_{-0.004}$	$0.95^{+0.16}_{-0.16}$	$0.94^{+0.06}_{-0.06}$	$0.80^{+0.01}_{-0.01}$
Mass (M_{Jup})	36^{+3}_{-3}	33^{+22}_{-22}	47.8[c]	8.4[c]
C/O	$0.53^{+0.01}_{-0.01}$		$0.96^{+0.09}_{-0.01}$	$0.362^{+0.002}_{-0.002}$
[M/H] (dex)	$0.28^{+0.02}_{-0.02}$		$-0.02^{+0.07}_{-0.10}$	$0.05^{+0.01}_{-0.01}$
$\log(L_{Bol}/L_{Sun})$	$-5.70^{+0.04}_{-0.01}$	$-5.74^{+0.01}_{-0.01}$	-5.71[d]	-5.72[d]
T_{eff} (K)	758^{+18}_{-3}	677^{+56}_{-56}	675^{+9}_{-5}	745^{+3}_{-3}

[a] Combination of optical and near-infrared spectroscopy with mid-infrared photometry (see Filippazzo et al. 2015 for references).

[b] The IRTF/SpeX spectrum at R$\sim$100.

[c] Calculated from the reported radius and log(g).

[d] Calculated from the reported radius and T_{eff}.

grid point is shown in Figure 4.2a compared to our retrieved TP profiles. When the IRTF/SpeX spectrum is included, the retrieved TP profiles deviate from the the adiabat of the Elf Owl model deeper than $\sim$ 10 bars.

The best fit spectrum from the Elf Owl grid fit is shown in Figure 4.5b, compared to the NIRSpec/G395H data and the best model from our full SED retrieval. The model residuals from the data shown in Figure 4.5c highlight that the Elf Owl model particularly struggles to reproduce the flux from $\sim$3.8 - 4.3 μm, the region of the spectrum mostly dominated by CO_2 and PH_3 (representative cross sections of each molecule are shown in Figure 4.5a in addition to Extended Data Figure 4.7). In particular, the model from the Elf Owl grid fit has too much PH_3 and too little CO_2 to match the data over these wavelengths.

The chemical abundances as a function of pressure for the closest Elf Owl grid model to the fitted parameters are shown in Figure 4.5d, compared to the constant-with-height abundances from our full SED retrieval. Overplotted in gray is the flux average contribution function for our best fit model. For the regions of the atmosphere we are probing, our retrieved abundances for H_2O, CH_4, NH_3, and CO are all higher than those in the Elf Owl grid model. The biggest discrepancies though are CO_2 and PH_3, the latter of which we only retrieve an upper limit for, consistent with where the model spectrum struggles to match the observed data. The difficulty in having enough CO_2 to match the observed features while reproducing the rest of the observed spectrum indicates the assumed chemical timescale for CO_2 may be incorrect or the vertical mixing may be faster where CO_2 quenches in the atmosphere. 2MASS 0415-0935 joins a number of T

and Y dwarfs for which PH_3 is expected but not detected (Morley et al. 2018; Miles et al. 2020; Beiler et al. 2023) suggesting a need for significant revisions to our understanding of phosphorous chemistry.

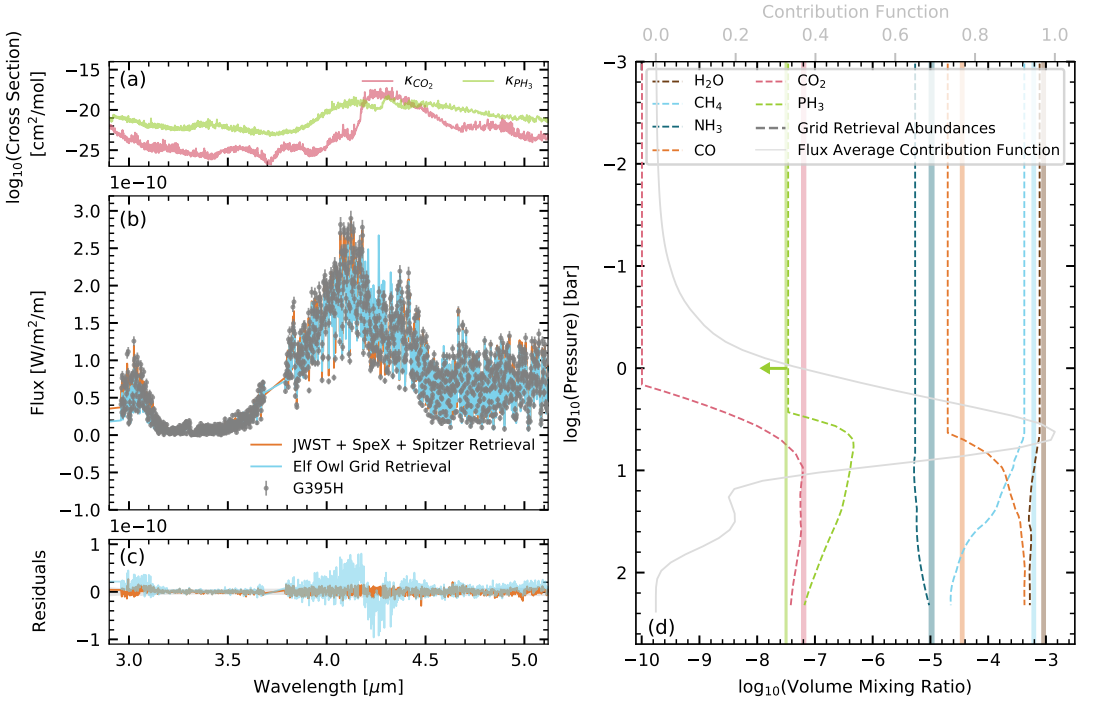

Figure 4.5: **Comparison to grid retrieval results from the Sonora Elf Owl grid.** (a) The absorption cross-sections of CO_2 (pink) and PH_3 (green) at 1 bar and 650 K. (b) The JWST/G395H data in grey, compared to the best fitting model from our free retrieval on all three datasets in orange, and the best fitting interpolated spectrum from the Sonora Elf Owl grid in blue. (b) The observational residuals of both models from panel (a). The errorbars of the G395H data are represented by the grey shaded region. (c) The uniform-with-altitude mixing ratios of H_2O (brown), CH_4 (light blue), NH_3 (teal), CO (orange), and CO_2 (pink) from our retrieval on all three datasets are shown by the vertical shaded regions, which span the 1σ uncertainties of each abundance. The retrieved upper limit on the mixing ratio of PH_3 is indicated by the green line and accompanying arrow. The corresponding abundance profiles from the interpolated Sonora Elf Owl grid are shown by the dashed lines. Overplotted in light grey is the flux average contribution function.

4.3.3 Implications for Future NIRSpec/G395H Observations of Brown Dwarfs

Taking inventory of major carbon- and oxygen- bearing molecules: Our retrieval results on solely the JWST NIRSpec/G395H observations of 2MASS 0415-0935 allows us to constrain all major carbon- and oxygen-bearing molecules (H_2O, CO, CO_2, and CH_4) to within ∼0.15 dex, allowing robust estimations of the object's metallicity and C/O ratio. While the posteriors for each parameter shift and tighten with the addition of observations at other wavelengths, the G395H observations alone can provide significant insight into the atmosphere of this brown dwarf.

Measuring ^{12}CO/^{13}CO: 2MASS 0415-0935 is the fourth and coldest substellar object with a measured ^{12}CO/^{13}CO ratio. The measured ^{12}CO/^{13}CO = 97^{+25}_{-18} for the young L5 dwarf 2MASS J03552337+1133437 (Y. Zhang et al. 2021b) is similar to our measured value for 2MASS 0415-0935, both of which are close to the measured solar value of 93.5 ± 0.7 (Lyons et al. 2018). In contrast, both the widely-separated super Jupiter TYC 898-760-1 b and the hot Jupiter WASP 77 Ab show enchanced^{13}CO, with ^{12}CO/^{13}CO = 31^{+17}_{-10} and 20^{+23}_{-10}, respectively (Y. Zhang et al. 2021a; Line et al. 2021). Our ability to place tight constraints on the ^{12}CO/^{13}CO ratio for 2MASS 0415-0935 indicates the strong promise of JWST NIRSpec/G395H measuring this isotopologue ratio in addition to molecular abundances for a large sample of substellar objects in order to better tease out different formation pathways.

Testing our understanding of chemistry and vertical mixing: The precise constraints on chemical abundances we retrieve for 2MASS 0415-0935 allow us

to identify shortcomings with the Sonora Elf Owl grid of models in fitting the NIRSpec/G395H observations, particularly in matching observed PH_3 and CO_2 features. The increased spectral resolution of the observations presented here aid in disentangling the PH_3 and CO_2 features, which can blend and mask each other at lower resolutions(Beiler et al. 2023). Atmospheric retrieval studies on a large sample of cool brown dwarfs observed with NIRSpec/G395H will be an important step in identifying how our knowledge of the chemistry and physics that govern these atmospheres needs to be revised.

4.4 Methods and Extended Results

4.4.1 Observations and Data Reduction

JWST Program 2124 obtained both NIRSPEC G395H spectra and MIRI F1000W, F1280W, and F1800W photometry to fill out the peak of the spectral energy distribution (SED) and the tail of the SED for 12 brown dwarfs. NIRSPEC data was obtained using the F290LP filter, the G395H grating, the S200A1 aperture and the SUB2048 subarray. The resultant wavelength coverage ranged from 2.87 to 5.14 micron with a resolution of ∼2700. Acquisition images were first obtained for each target using the WATA method, the CLEAR filter, and the NRSRAPID readout pattern. W0415 was observed with NIRSPEC on 16 October 2022 with 11 groups per integration, 3 integrations per exposure and 3 total dithers for a summation of 9 total integrations in 168.488 seconds of exposure time. Recorded time including overhead for the W0415 NIRSPEC observation was 1.03 hours.

For the reduction of all JWST data, we relied on the pipeline outputs which update with calibration data as it is received from the telescope.

4.4.2 Retrieval Model

For our atmospheric retrieval analysis we used the CHIMERA framework which has been successfully applied previously to brown dwarf spectra (Line et al. 2017; Zalesky et al. 2019). We specifically use the version of CHIMERA (Zalesky et al. 2022) which uses graphical processing units (GPUs), modified as outlined in (Hood et al. 2023) for use on medium-resolution spectra. We use the affine-invariant MCMC ensemble sampler package *emcee*(Foreman-Mackey et al. 2013) to sample posterior probabilities. The free parameters in our model and our adopted prior ranges are listed in Extended Data Table 4.5. We include uniform-with-altitude volume mixing ratios of H_2O, CH_4, CO, CO_2, H_2S, NH_3, and PH_3. For retrievals including the SpeX spectrum we also include mixing ratios of the alkalis K and Na, as they are expected to contribute important opacity at the near-infrared wavelengths. The opacity sources for each included chemical species are listed in Extended Data Table 4.5. Extended Data Figure 4.7 shows the cross sections for each molecule at a representative pressure and temperature over the wavelengths of the G395H observations. As in Line et al. (2021), we include the $^{12}C^{16}O$ and $^{13}C^{16}O$ lines separately weighted by the terrestrial ratio of ^{12}C:^{13}C = 89:1 built into the HITRAN/HITEMP line lists. The CO isotopic abundance is parameterized as the $\log_{10}$ of the isotopic ratio relative to terrestrial.

We also include errorbar inflation exponents (Line et al. 2015) for each data set analyzed, to account for underestimated data uncertainties or missing physics in

the modeling framework. There are 15 independent temperature-pressure (TP) profile points, which are subject to a smoothing hyperparameter(Line et al. 2015). The TP profile points are interpolated onto a finer 70 layer pressure grid for the radiative transfer. Other free parameters include the surface gravity, a radius-to-distance scaling factor, and three cloud parameters: cloud volume mixing ratio, cloud pressure base, and sedimentation efficiency (Ackerman & Marley 2001). For the cloud opacity we used Mie scattering theory assuming a Mg2SiO4 cloud with optical properties from Wakeford & Sing (2015).

We generate the model spectrum piecewise at $\sim 10\times$ the spectral resolution of the incorporated datasets. For the G395H data, the spectral resolution of R$\sim$2700 is sufficient to potentially see effects from radial and rotational velocities. Thus, we incorporate these properties as free parameters as well, as described in Hood et al. (2023). In brief, the radial velocity is applied using the *dopplerShift* function from *PyAstronomy* (Czesla et al. 2019). The rotation velocity is applied using the *fastRotBroad* function from PyAstronomy, applied separately on the blue and red halves of the G395H model to minimize errors from not using the slower wavelength-dependent rotation kernel. The shifted and broadened model spectrum is then binned to the instrument wavelength arrays using a tophat kernel, and scaled to the observed flux using the $(R/D)^2$ parameter.

The choice of method used to smooth the forward model to the spectral resolution of the observations can affect the v sin i constraints from our retrieval. In addition to the tophat binning, we explored convolving the model with a Gaussian kernel meant to capture the wavelength-dependent resolving power of the instrument (assuming the

instrument line shape is Gaussian and Nyquist sampled) and then interpolating the smoothed model onto the input data wavelength grid. With this method, we no longer constrain the v sin i of this object and the median radial velocity decreases by 3 km s^{-1}. However, no other posteriors significantly change. As such, to avoid making as many assumptions about the exact instrument line profile, all reported values and posteriors are from retrievals using the tophat binning method. However, we caution that the resulting RV and v sin i constraints may not be reliable. Extended Data Figure 4.8 shows the corner plot summary of the posterior probability distribution, including the RV and v sin i.

4.4.3 Sonora Elf Owl Grid Retrieval

The Sonora Elf Owl grid includes cloud-free 1D radiative–convective equilibrium model atmospheres with vertical mixing induced disequilibrium chemistry across a large range of T_{eff} (275-2400 K), log(g) (3.25-5.5), the mixing parameter K_{zz} (10^2-10^9 cm^2/s), atmospheric metallicity (0.1× to 10× Solar), and C/O ratio (0.22 to 1.14). The model grid was computed using the open-sourced Python-based PICASO atmospheric model (Mukherjee et al. 2023; Batalha et al. 2019).

To make an even comparison with the retrieval results, the calculated TP profile and atmospheric chemistry from the Elf Owl grid is first used to recompute the thermal spectra from the Elf Owl grid using the same gaseous opacities which has been used for the retrieval analysis in this work. These recomputed high-resolution (R$\sim$ 30000) spectra are then used to perform a Bayesian grid fitting analysis on the observed spectra of 2MASS 0415-0935. The Python Scipy based linear interpolating function

RegularGridInterpolator (Virtanen et al. 2020) is used to linearly interpolate the Elf Owl grid spectra at each wavelength point as a function of T_{eff}, log(g), $\log_{10}K_{zz}$, metallicity, and C/O ratio. This spectral interpolator is then wrapped within the DYNESTY Bayesian sampler Speagle (2020). We assume uniform priors for T_{eff}, log(g), $\log_{10}K_{zz}$, metallicity, and C/O ratio within the extent of these parameter values covered by the Elf Owl grid. We also use a uniform prior for the object radius between 0.6 to 1.2 Jupiter radius. Additionally, uniform priors between 0-50 km/s are also used for both the rotational broadening velocity and radial velocity of the object. For each iteration of the Bayesian sampler, the interpolator is used to generate the model spectrum for the drawn atmospheric parameters. The interpolated spectrum is then rotationally broadened using the *fastRotBroad* function of the PyAstronomy package Czesla et al. (2019). The rotationally broadened spectrum is also doppler shifted with the *dopplerShift* function of the PyAstronomy package. The high-resolution spectrum is then scaled by the sampled object radius and finally binned down to the wavelength bins of the observed data. The model spectra and the observed data are then used to calculate a log-likelihood metric which the sampler tries to minimise while it iterates to find the best-fit model.

The obtained posterior distributions on the atmospheric and other parameters are then used to estimate the best-fit parameter values and their uncertainties. It should be noted that this technique doesn't take the model interpolation uncertainties into account while estimating the posterior distributions of each atmospheric parameter. Previous work has shown that the uncertainties on the estimated parameters can be somewhat boosted when the interpolation uncertainties are taken into account while

fitting the data (e.g., Z. Zhang et al. 2021).

4.4.4 Calculation of Physical Parameters

Table 4.1 lists a number of physical parameters of 2MASS 0415-0935 calculated from our retrieval on all three datasets (IRTF/SpeX, JWST/NIRSpec, and Spitzer/IRS), as well as the fit of these data to the Sonora Elf Owl grid of models and two previous studies of this object. To calculate these properties and their uncertainties from the parameters in our retrieval framework, we take 5000 random samples of the posterior. We calculate elemental abundances from our precise molecular volume mixing ratio constaints, with C/H = (CH_4 + CO + CO_2)/H, N/H = NH_3/H, O/H = (H_2O + CO + 2CO_2)/H, S/H = H_2S/H, and P/H = PH_3/H. We note that the total nitrogen abundance, and the resulting metallicity, is likely a lower limit as as a significant amount of the object's nitrogen could be in the form of N_2 instead of NH_3. As in previous works (Line et al. 2021; Zalesky et al. 2022), we account for potential depletion of atmospheric oxygen due to condensation by multiplying the oxygen abundance by 1.3 (the correction factor needed assuming 3.28 O atoms per Si atom from silicate cloud formation; Burrows & Sharp 1999). However, this oxygen correction factor has been called into question (Calamari et al. 2022) and therefore better understanding of potential oxygen sinks in brown dwarf atmospheres may be needed to more confidently connect measured atmospheric oxygen abundances to the bulk value.

From these elemental abundances, we calculate the metallicity M/H as the sum of the abundances and the metallicity relative to solar [M/H] = $\log_{10}$(M/$H_{0415-0935}$ / M/H_{solar}) assuming the solar abundances from Lodders & Palme (2009) for consistency

with the Sonora family of models. We also calculate the C/O ratio from the C and O abundances. To calculate the L_{Bol} and corresponding effective temperature T_{eff} implied by our retrieval results, we generate a low-resolution spectrum over 0.3 to 250 μm for each sample in our posterior.

4.4.5 Extended Results

3 μm NH_3 Feature

Beiler et al. (2023) recently reported a newly identified NH_3 feature at 3 μm in the JWST NIRSpec/PRISM spectrum (R $\sim$ 100) of the Y0 dwarf WISE J035934.06-540154.6, although the detection is tentative given the signal-to-noise and spectral resolution of the data as the NH_3 feature only impacts two data points. As shown in Extended Data Figure 4.7, the Q branch of the v_1 band of NH_3 overlaps with a window in CH_4 and H_2O opacity in this region. We can confidently confirm the presence of this 3 μm NH_3 feature in the NIRSpec/G395H spectrum of 2MASS 0415-0935. Extended Data Figure 4.9 shows the best fitting model from our JWST retrieval compared to the same model with significantly reduced NH_3 abundance, showing the importance of NH_3 opacity in reproducing the observed flux over $\sim$30 data points at this wavelength. This NH_3 feature also explains our ability to constrain the NH_3 abundance with the G395H spectrum alone as shown in Figure 4.2. Adding in the Spitzer/IRS data which covers the strong NH_3 feature at 10.5 μm does slightly shift and tighten our abundance constraint, but not substantially. Thus, future NIRSpec/G395H observations hold promise to constrain the NH_3 abundance for a multitude of cool brown dwarfs even when longer

wavelength observations are not available.

Elemental Abundances in Solar System Context

We normalize the calculated elemental abundances of 2MASS 0415-0935 (see above) by the protosolar values for comparison with solar system values as done in Atreya et al. (2016) and Line et al. (2021), with [X/H] = $\log_{10}(\frac{n_x/n_H}{n_{x,\odot}/n_{H,\odot}})$. Figure 4.10 shows these abundances compared to those of the solar system giants (Atreya et al. 2016; Li et al. 2020) and assuming the protosolar elemental abundances (Lodders & Palme 2009). The calculated nitrogen abundance from the retrieved NH_3 abundance is [N/H]=$0.073^{+0.007}_{-0.005}$; however, we plot this [N/H] as a lower limit since much of nitrogren content might instead be in N_2. While we plot an upper limit for [P/H] derived from our retrieved upper limit on the PH_3 abundance, our understanding of phosphorous chemistry needs to be revised (as discussed in the main text) so there may actually be much more phosphorous present in a different form. We get tight and bounded constraints for [C/H] = $1.36^{+0.07}_{-0.06}$ and [O/H] = $1.17^{+0.05}_{-0.05}$, consistent with a slightly super-solar metallicity and with a precision that in some cases greatly exceeds that for solar system objects.

4.5 Extended Data Tables and Figures

Table 4.2: Free Parameters in Our Retrieval Model

Parameter	Description	Prior Range
$\log_{10}(f_i)$	$\log_{10}$ of the uniform-with-altitude volume mixing ratios of H_2O, CH_4, CO, NH_3,H_2S, PH_3, Na, and K	-12 - 0
$^{13}CO/^{12}CO$	$\log_{10}$ isotopic ratio relative to terrestrial (1/89)	-3-3
log(g)	log surface gravity [cm s^{-2}]	0 - 6
$(R/D)^2$	radius-to-distance scale [R_{Jup}/pc]	0 - 1
T(P)	temperature at 15 pressure levels [K]	0 - 4000
b_j	errorbar inflation exponent for each dataset	$0.01 \cdot \min(err_j^2)$ - $100 \cdot \max(err_j^2)$
γ	TP profile smoothing hyperparameter	0 - ∞
log(Cloud VMR)	log of the cloud volume mixing ratio	-15 - 0
$\log(P_c)$	log of the cloud base pressure	-2.8 - 2.3
f_{sed}	sedimentation efficiency	0 -10
RV	radial velocity [km s^{-1}]	0 - 100
$v \sin i$	rotational velocity [km s^{-1}]	0 - 100

Table 4.3: Opacity Sources for Our Retrieval Model

Species	Opacity Sources
H2-H2, H2-He CIA	Richard et al. (2012)
H_2O	Polyansky et al. (2018)
CH_4	Hargreaves et al. (2020)
CO	Li et al. (2015),^{12}CO and ^{13}CO included separately weighted by the built-in terrestrial ratio
NH_3	Coles et al. (2019)
H_2S	Tennyson & Yurchenko (2012), Azzam et al. (2015), isotopologues Rothman et al. (2013)
K	Allard et al. (2016)
Na	Allard et al. (2019)

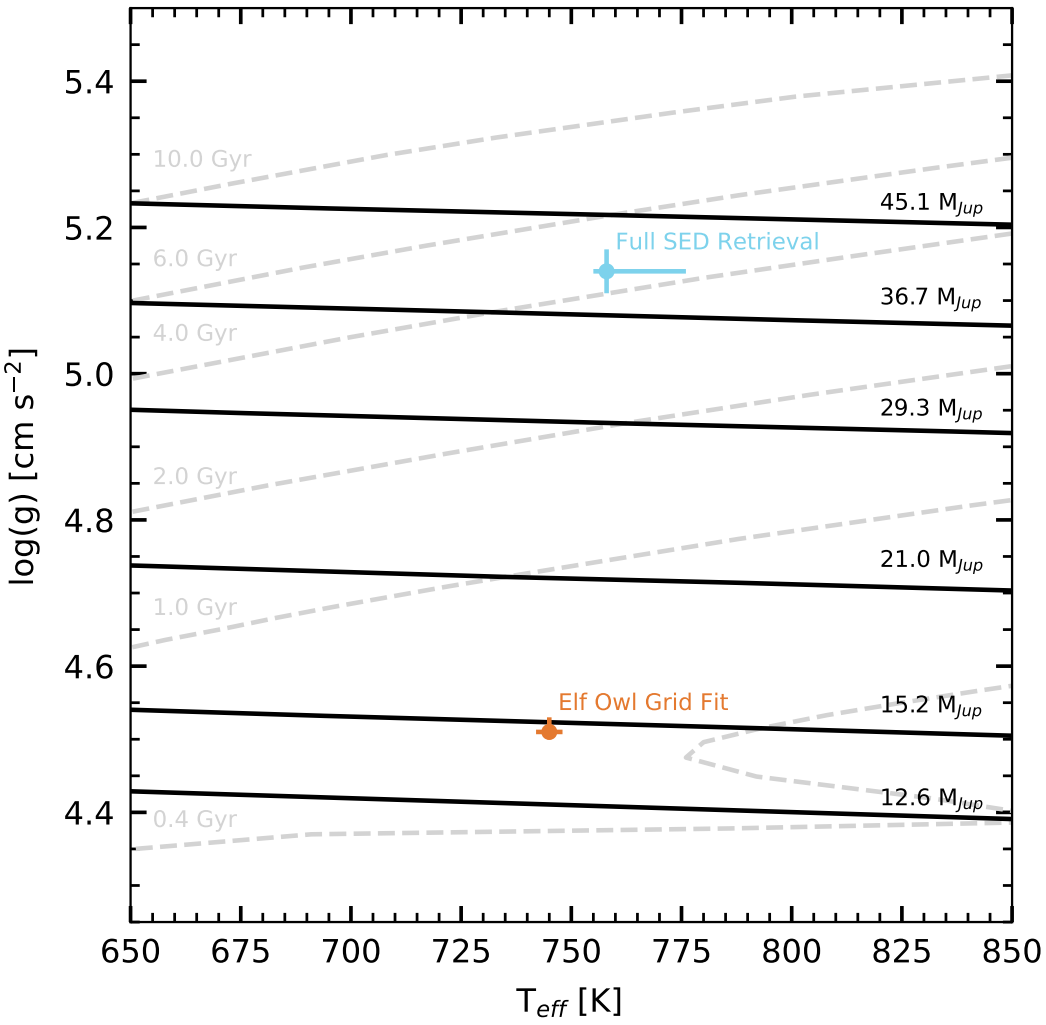

Figure 4.6: **Comparison of retrieved physical parameters of 2MASS 0415-0935 to Sonora Bobcat evolutionary models (Marley et al. 2021).** Isochrones are shown in black and cooling tracks are shown in grey in the surface gravity-efferctive temperature plane. The median values and uncertainties of these properties from our full SED retrieval are represented by the blue point and error bars, while the results of the Sonora Elf Owl grid retrieval are indicated by the orange point. Our retrieved surface gravity and effective temperature correspond to an age of 4 - 6 Gyr and a mass $\sim$ 39 M$_{Jup}$.

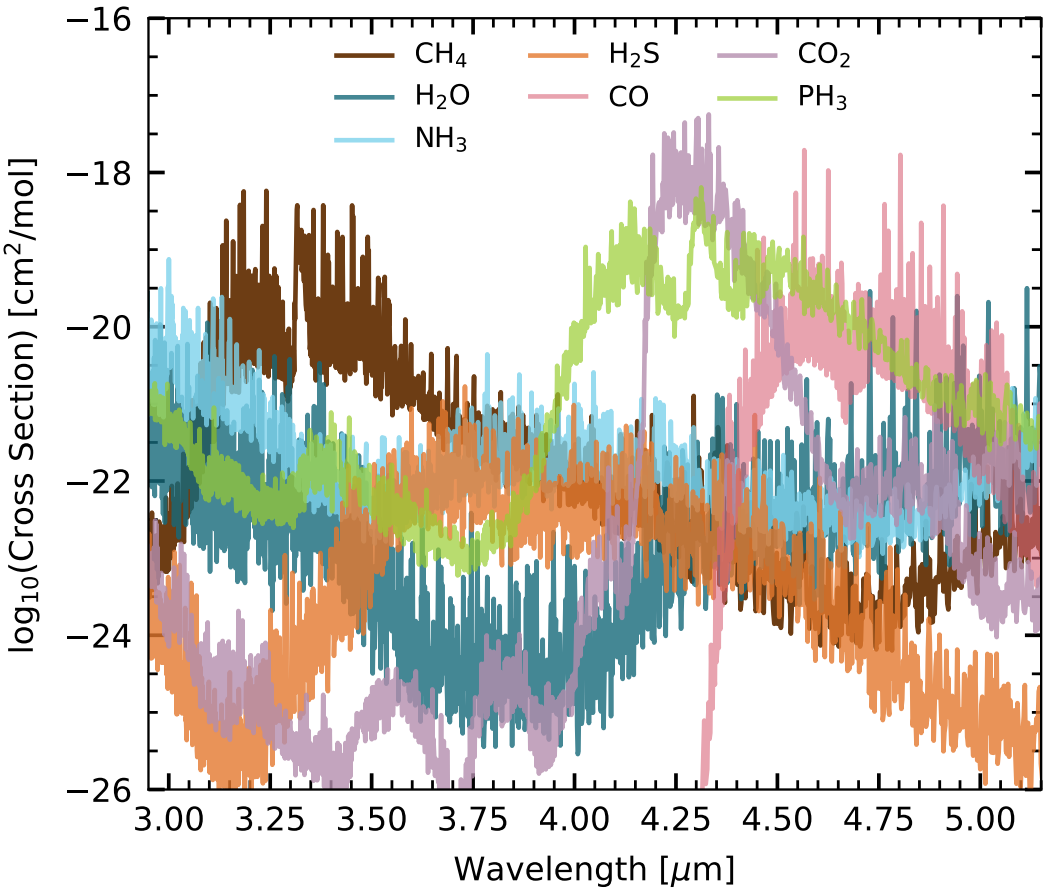

Figure 4.7: **Absorption cross sections for molecular species included in our retrieval analysis over the wavelengths covered by the JWST/ NIRSpec observations.** The plotted cross sections are for a temperature of 650 K and pressure of 1 bar.

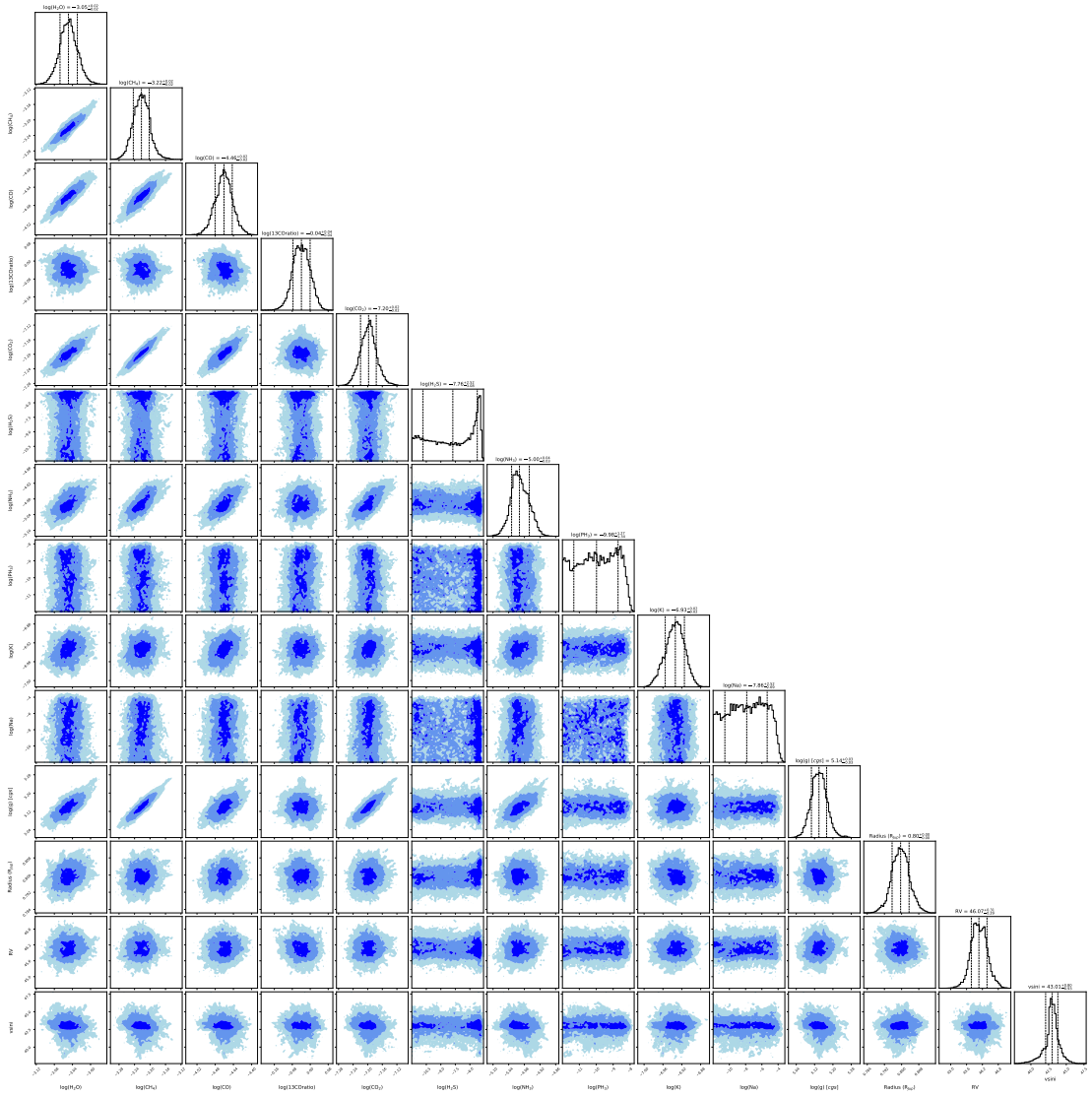

Figure 4.8: **Summary of the posterior probability distribution of the retrieval analysis on all three datasets (JWST/NIRSpec, IRTF/ SpeX, Spitzer/IRS).** For space constraints, we do not plot the posteriors for the temperature-pressure profile smoothing parameter γ, the error inflation terms for each dataset, or the cloud parameters, none of which showed strong correlations with other free parameters in our model.

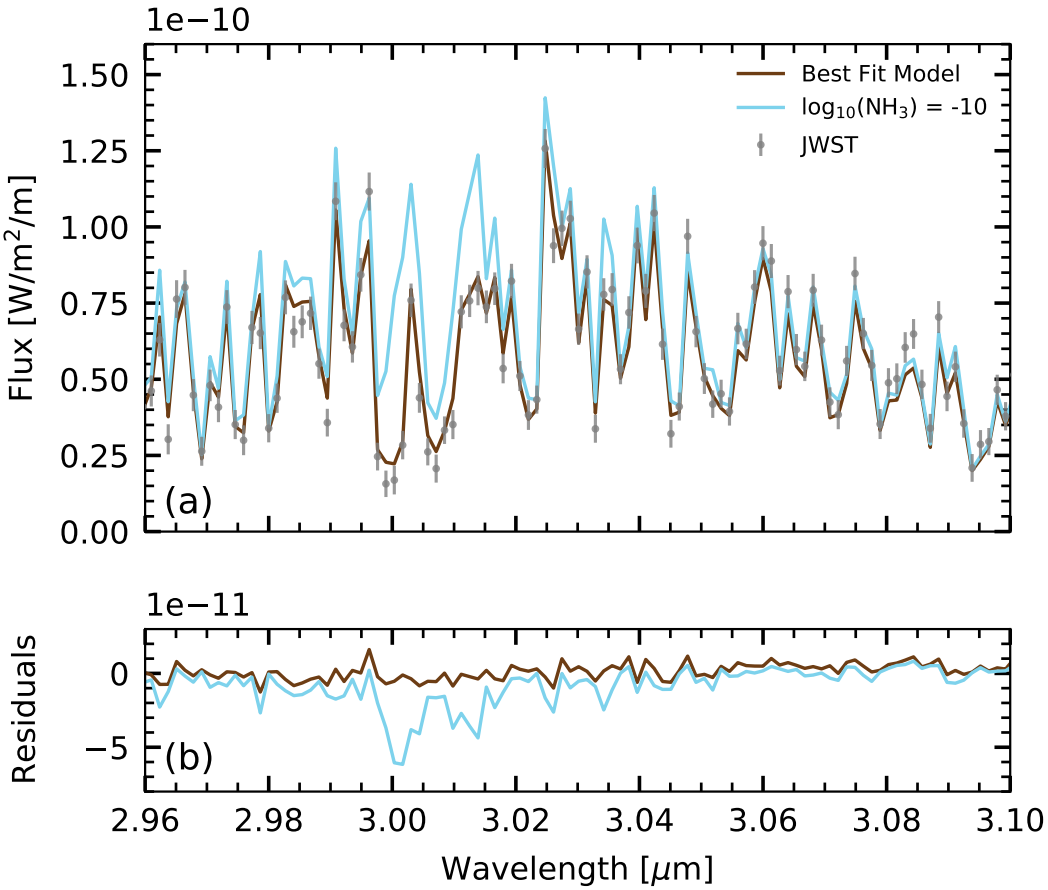

Figure 4.9: **Evidence of NH_3 absorption around 3 μm.** (a) The JWST NIRSpec/G395H data (grey data points) compared to the best fit model from our JWST-only retrieval (brown) and the same model but where the volume mixing ratio of NH_3 has been reduced to $\log_{10}(NH_3)$ = -10 (blue). (b) The observational residuals of each model from panel (a). The reduced NH_3 model clearly struggles to fit the observed spectrum $\sim 3\mu$m, confirming this small region as an NH_3 absorption feature.

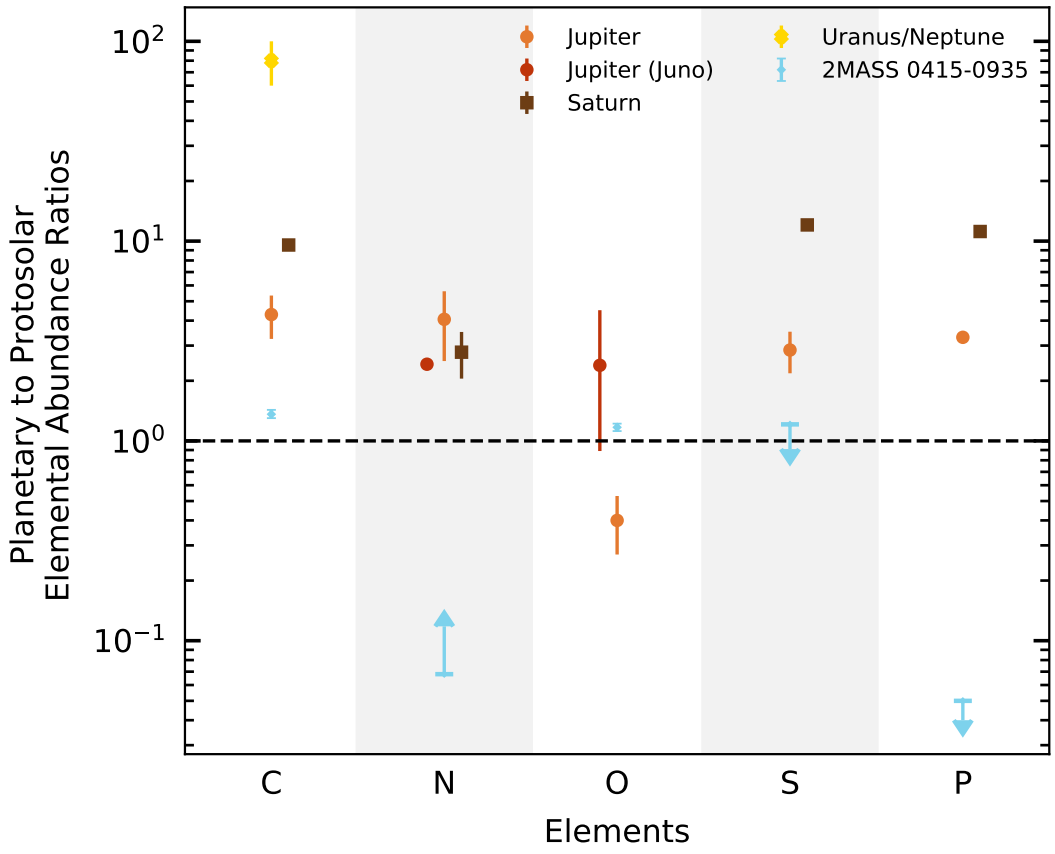

Figure 4.10: **Comparison of elemental abundance constraints for 2MASS 0415-0935 to the solar system objects, adapted from Atreya et al. (2016) and Line et al. (2021)** Elemental abundances from Atreya et al. (2016) for Jupiter are shown in orange, Saturn in brown, and Uranus and Neptune in yellow, while more recent measurements for Jupiter from JUNO (Li et al. 2020) are shown in red. The blue points and limits indicate the elemental constraints for 2MASS 0415-0935 derived from our retrieved abundances (see Methods). While we do retrieve tight constraints on the NH_3 abundance, the N/H value is shown as a lower limit as a significant amount of nitrogen may likely instead be in the form of N_2 in this object's atmosphere.

Chapter 5

Summary and Future Directions

In the past decade, substellar astrophysics has shifted focus from just detecting exoplanets and brown dwarfs to characterizing their atmospheres in depth. In this thesis, I have modeled substellar atmospheres and their observed spectra to determine what we can uniquely learn when increasing the spectral resolution of our observations. I have considered both transmission spectra of sub-Neptunes at R $\gtrsim$ 25,000 for high-resolution cross-correlation spectroscopy, and medium-resolution (R$\sim$ 3000-6000) emission spectra of brown dwarfs. The following sections contain a summary of each project and avenues for relevant future work, followed by a general look at the future of the field.

5.1 High-Resolution Cross-Correlation Spectroscopy of sub-Neptunes

Observed transmission spectra of sub-Neptunes at low spectral resolution are often featureless, hindering our ability to characterize their atmospheres due to hazes

or clouds that obscure molecular features. Chapter 2 showed the promise of applying high-resolution cross-correlation spectroscopy methods to sub-Neptunes, as the cores of the strongest lines are formed above the clouds. We modeled transmission spectra for GJ 1214b-like planets with thick photochemical hazes over 1 - 5 μm at R$\sim$25,000 - 100,000. In addition, we compared the cross-correlation function often used to a likelihood function derived for use in atmospheric retrievals of these kinds of observations (Brogi & Line 2019), finding the likelihood function more useful and particularly able to detect the presence of haze opacity. We presented the signal-to-noise needed to detect a host of molecules like H_2O, CH_4, CO, CO_2, and HCN as a function of wavelength range and spectral resolution. We then compared these requirements to the capabilities of current and future instruments under relatively ideal conditions, finding CO and H_2O should be detectable for observations of GJ 1214b in H and K bands with current instruments. High-resolution spectrographs behind AO on upcoming thirty meter class telescopes should enable the detection of molecular absorption signatures with minutes of observing time.

5.1.1 Future Directions

The most obvious future direction is to observe the transmission spectrum of GJ 1214b with a high-resolution spectrograph. I was awarded 10 hours (6 transits) of IGRINS time on the 8-meter Gemini South telescope in the 2022A semester as P.I. to do so, but only one transit was observed due to weather and instrument maintenance needs. A second attempt at taking these observations would be a clear way to test the predictions of this work. However, detecting CO or H_2O in the atmosphere of

GJ 1214b from these observations will require figuring out the best way to remove stellar contamination from the M dwarf host star. M dwarfs are often very active, posing problems of variability and even saturation to current techniques (Brogi & Birkby 2021). Furthermore, M dwarf stars have much more complicated spectra than hotter stars, including features from the very molecules one would attempt to detect in the atmosphere of the planet. While a challenge, this will be a critical step in pushing this technique to smaller planets in the future.

However, recent phase curve observations of GJ 1214b with JWST's MIRI instrument indicate the need for a high metallicity atmosphere ($\geqq$ 1000x solar) with a thick and highly-reflective aerosol layer to match the observations, although a steam atmosphere with high haze production would also be consistent (Kempton et al. 2023; Gao et al. 2023). Thus, the 50x solar metallicity and hydrocarbon haze (too absorptive) assumed for our model are unlikely characteristics of GJ 1214b specifically. The lower scale height implied by such a high metallicity atmosphere most likely means that longer exposure times and higher spectral resolutions may be needed to detect molecular absorption features than are presented in Chapter 2. Kempton et al. (2023) also report a tentative detection of H_2O absorption, but the feature is somewhat degenerate with the presence of CH_4 or HCN. Future observations of GJ 1214b with JWST are likely to provide even better insight into its atmosphere. Applying a similar analysis framework to that presented in Chapter 2, but with modeled atmospheres that are consistent with JWST observations of GJ 1214b, may allow for a better understanding of the observability of these hazy sub-Neptunes with high-resolution cross-correlation spectroscopy.

Furthermore, one could simulate the potential constraints from joint analysis of JWST observations with ground-based high-resolution spectroscopy, in order to identify the optimal observing strategies needed to fully characterize GJ 1214b's atmosphere.

5.2 Atmospheric Retrieval With Ground-Based Medium-Resolution Spectra of Brown Dwarfs

Atmospheric retrieval analyses of brown dwarf spectra have allowed for constraints on the compositions and thermal structure of a number of objects, but these studies have typically focused on low-resolution data R $\sim$ 100 (e.g., Line et al. 2017; Zalesky et al. 2022). Chapter 3 presented a first foray into applying atmospheric retrieval methods to a medium-resolution (R$\sim$6000) FIRE spectrum of the T9 dwarf UGPS J072227.51-054031.2 (U0722). We detail a number of modifications and tests performed when adapting the CHIMERA retrieval framework to data at this resolution, hopefully providing a "cookbook" for future modelers to consult when similarly moving to increased spectral resolution. For example, choices like CH_4 line list, alkali wing opacity, and how to deal with order stitching in the data, can all strongly affect retrieved constraints on atmospheric parameters. Compared to analysis of low-resolution observations of the same object, constraints on atmospheric abundances from the FIRE retrieval improve by an order of magnitude or more, leading to near-stellar precision ($\sim$ 0.02 dex). However, our retrieved radius is unphysically small at $\sim$ 0.5 R_{Jup}, calling into question the accuracy of our results and adding to a growing number of brown dwarfs with too small radii from retrievals.

5.2.1 Future Directions

One avenue for extending this work is just applying the best retrieval practices identified in Chapter 3 to a larger sample of brown dwarfs observed with FIRE. The sample with existing FIRE observations includes 14 other late T dwarfs, including the benchmark HD 3651B which orbits a K-type star. Performing an atmospheric retrieval on the FIRE observations of HD 3651B in particular would offer a great way to validate the framework and retrieved constraints by comparing our results to the metallicity and age of the host star, as was done for low-resolution observations by Line et al. (2015). Archival data sets of brown dwarf observations at this resolution or even higher exist for many other instruments as well, especially those used for brown dwarf radial velocity surveys. For one example, the very high quality R ∼45,000 spectrum of a T6 dwarf analyzed by Tannock et al. (2022) could be an interesting testbed for pushing this retrieval framework to even higher spectral resolutions.

Taking advantage of the wealth of literature on brown dwarf spectra will require further improvements on the modeling side, however. More retrieval frameworks in addition to CHIMERA should be adapted for use at this spectral resolution, perhaps similarly taking advantage of the computational power of GPUs, so results from different groups can be compared to one another. Continued work on opacity data, from improving accuracy of line positions to the treatment of pressure-broadened alkali line wings, will be crucial to accurately matching the observed features. Concentrated theoretical work focusing on the prevalence of small radii for brown dwarfs in retrieval studies, perhaps using simulated data sets from the best currently-available self-consistent mod-

els, could hopefully shed light on the source of the issue. Furthermore, extension to medium-resolution spectra of warmer objects like early T and L dwarfs may require a more sophisticated treatment of clouds within the forward model than is used here. Better quality data from JWST, discussed more in Chapter 4, could also yield further insight into modeling shortcomings. Comparing the JWST NIRSpec spectrum of an object with the FIRE spectrum, for example, could provide insight into any important instrumental systematics that bias results from the FIRE data. As we do not yet know if JWST observations will be sufficient to constrain the H_2S abundance of an object, combining JWST observations with ground-based spectra from FIRE or higher resolution instruments could also allow for precise abundance constraints for the important carbon-, oxygen-, nitrogen-, and sulfur-bearing species.

5.3 Atmospheric Retrieval With JWST Medium-Resolution Spectra of Brown Dwarfs

The launch of JWST promises unprecedented quality observations of exoplanets and brown dwarfs, particularly for wavelength ranges difficulty to reach from the ground. Chapter 4 presented the first retrieval analysis using the maximum resolution of JWST's NIRSpec instrument, using the G395H (R$\sim$2700, 2.87 - 5.14 μm) filter for observations of the T8 dwarf 2MASS 0415-0935. We also incorporated previous observations of this object with IRTF/SpeX and Spitzer/IRS to study the full spectral energy distribution of this object. We are able to fit the observed spectral features remarkably well with small residuals considering the high signal-to-noise of the data. We get precise

constraints on the abundances of all the major oxygen- and carbon- bearing species in the atmosphere (H_2O, CH_4, CO, and CO_2) in addition to NH_3, enabling robust determinations of the metallicity and C/O. Our constrained abundance for CO_2 and upper limit for PH_3 are in disagreement with predictions from disequilibrium chemistry grid models, indicating we need to revise our understanding of the chemical behavior of these species. At this spectral resolution, we are also able to constrain the isotopologue ratio of $^{12}CO/^{13}CO = 97^{+9}_{-8}$, making 2MASS 0415 the coldest ($\sim$ 760 K) object with such a measurement outside of our solar system. Our measurement of $^{12}CO/^{13}CO = 97^{+9}_{-8}$ is similar to the solar value and the only other brown dwarf measurement (Y. Zhang et al. 2021b) but significantly higher than the values measured for a hot Jupiter and widely-separated super Jupiter (Line et al. 2021; Y. Zhang et al. 2021a), hinting at different formation scenarios for the two types of objects.

5.3.1 Future Directions

Chapter 4 shows the promise of NIRSpec/G395H observations for obtaining near-stellar precision constraints on abundances, including isotopologues. Observing many other brown dwarfs with this grating and instrument combination offers the potential for a uniform retrieval analysis to obtain abundance measurements for a large sample of objects. Abundances of CO, CH_4, and CO_2 will particularly offer insight into the workings of disequilibrium chemistry, especially over a range in effective temperatures. PH_3 has not yet been observed in cool brown dwarfs even when expected (this work, Morley et al. 2018; Miles et al. 2020; Beiler et al. 2023), so potentially observing any clear spectral signatures of PH_3 or at least strong upper limits on its abundance for

a larger sample of objects will provide better guidance on our understanding of phosphorous chemistry. In addition, studying NIRSpec/G395H observations for a large sample of brown dwarfs could easily triple or quadruple the number of extrasolar objects with measured $^{12}CO/^{13}CO$ ratios, allowing for a better understanding of the distribution of this value across the brown dwarf population. Other potential isotopologues should also be considered for possible signatures in these observations, such as deuterium or ^{18}CO (Morley et al. 2019; Zhang et al. 2022).

However, G395H is not the only high-resolution grating available for NIRSpec. Performing a similar retrieval analysis on various combinations of observations using the G140H or G235H gratings ($\sim$ 0.8 - 3.0 μm) in addition to G395H may allow for even more precision on retrieved parameters than is reported here. Even for low-resolution JWST observations, it would be interesting to repeat the same analysis but swap in NIRSpec PRISM and MIRI observations for the IRTF/SpeX and Spitzer/IRS data sets considered here, to see if just the higher signal-to-noise significantly affects the constraints obtained from analyzing the whole spectral energy distribution.

5.4 Future of Atmospheric Characterization

The launch of JWST marks the dawn of a new era for the atmospheric characterization of exoplanets and brown dwarfs. Observations with JWST stand to revolutionize our understanding of substellar atmospheres with unprecedented data quality. Extremely large telescopes (ELTs) offer another important avenue forward, particularly with instruments capable of high contrast imaging combined with high-resolution

spectroscopy. Furthermore, jointly analyzing high-resolution observations with ELTs with lower resolution observations from JWST offers an important pathway for complete and accurate characterization of substellar atmospheres. Looking further into the future, a potential next Great Observatory consisting of a large (6 m aperture) infrared/optical/ultraviolet space telescope, as has been recommended by the National Academies' Decadal Survey on Astronomy and Astrophysics 2020, could find potential clues of life on planets outside of our solar system.

The promise of such novel and high quality data on the horizon require similar rapid development of modeling tools in order to fully take advantage of these improvements in instrumentation and observation. Laboratory astrophysics will be a crucial piece of this effort for refined studies of important modeling inputs like opacity data and aerosol properties. The full range of modeling techniques, from atmospheric retrievals to 1D and 3D self-consistent models, will need to be improved and tested in order to gain a better understanding of the assumptions and parameterizations that are valid for different types of objects and observations. We will need direct and open collaboration among researchers working on all aspects of substellar atmospheric characterization, including investigators of Solar System science, laboratory studies, formation models, atmosphere models, observations, and instrumentation. Together, we can hope to further our understanding of the formation and evolution of substellar objects, and in the process our own place in the vast and diverse ecosystem of alien worlds.

Bibliography

Ackerman A. S., Marley M. S., 2001, ApJ, 556, 872

Allard F., Freytag B., 2010, Highlights of Astronomy, 15, 756

Allard F., Hauschildt P. H., Alexander D. R., Tamanai A., Schweitzer A., 2001, ApJ, 556, 357

Allard N. F., Kielkopf J. F., Allard F., 2007a, European Physical Journal D, 44, 507

Allard F., Allard N. F., Homeier D., Kielkopf J., McCaughrean M. J., Spiegelman F., 2007b, A&A, 474, L21

Allard F., Homeier D., Freytag B., 2011, in Johns-Krull C., Browning M. K., West A. A., eds, Astronomical Society of the Pacific Conference Series Vol. 448, 16th Cambridge Workshop on Cool Stars, Stellar Systems, and the Sun. p. 91 (arXiv:1011.5405)

Allard N. F., Spiegelman F., Kielkopf J. F., 2016, A&A, 589, A21

Allard N. F., Spiegelman F., Leininger T., Molliere P., 2019, A&A, 628, A120

Alonso-Floriano F. J., et al., 2019, A&A, 621, A74

Artigau É., et al., 2014, SPIRou: the near-infrared spectropolarimeter/high-precision velocimeter for the Canada-France-Hawaii telescope. p. 914715, doi:10.1117/12.2055663

Asplund M., Grevesse N., Sauval A. J., Scott P., 2009, ARA&A, 47, 481

Atreya S. K., Crida A., Guillot T., Lunine J. I., Madhusudhan N., Mousis O., 2016, arXiv e-prints, p. arXiv:1606.04510

Azzam A. A. A., Lodi L., Yurchenko S. N., Tennyson J., 2015, J. Quant. Spec. Radiat. Transf., 161, 41

Baraffe I., Chabrier G., Barman T. S., Allard F., Hauschildt P. H., 2003, A&A, 402, 701

Barber R. J., Tennyson J., Harris G. J., Tolchenov R. N., 2006, MNRAS, 368, 1087

Barclay T., Pepper J., Quintana E. V., 2018, ApJS, 239, 2

Barman T. S., Macintosh B., Konopacky Q. M., Marois C., 2011, ApJ, 733, 65

Batalha N. M., et al., 2013, ApJS, 204, 24

Batalha N. E., Marley M. S., Lewis N. K., Fortney J. J., 2019, ApJ, 878, 70

Bean J. L., Miller-Ricci Kempton E., Homeier D., 2010, Nature, 468, 669

Bean J. L., et al., 2011, ApJ, 743, 92

Beiler S., Cushing M., Kirkpatrick D., Schneider A., Mukherjee S., Marley M., 2023, arXiv e-prints, p. arXiv:2306.11807

Benneke B., Seager S., 2012, ApJ, 753, 100

Beuzit J.-L., et al., 2008, in McLean I. S., Casali M. M., eds, Society of Photo-Optical Instrumentation Engineers (SPIE) Conference Series Vol. 7014, Ground-based and Airborne Instrumentation for Astronomy II. p. 701418, doi:10.1117/12.790120

Birkby J. L., 2018, arXiv e-prints, p. arXiv:1806.04617

Birkby J. L., de Kok R. J., Brogi M., de Mooij E. J. W., Schwarz H., Albrecht S.,

Snellen I. A. G., 2013, MNRAS, 436, L35

Birkby J. L., de Kok R. J., Brogi M., Schwarz H., Snellen I. A. G., 2017, AJ, 153, 138

Blake C. H., Charbonneau D., White R. J., 2010, ApJ, 723, 684

Bochanski J. J., Burgasser A. J., Simcoe R. A., West A. A., 2011, AJ, 142, 169

Booth R. A., Clarke C. J., Madhusudhan N., Ilee J. D., 2017, MNRAS, 469, 3994

Borucki W. J., et al., 2011, ApJ, 736, 19

Brandl B. R., et al., 2018, in Proc. SPIE. p. 107021U, doi:10.1117/12.2311492

Brogi M., Birkby J., 2021, in Madhusudhan N., ed., , ExoFrontiers; Big Questions in Exoplanetary Science. pp 8–1, doi:10.1088/2514-3433/abfa8fch8

Brogi M., Line M. R., 2019, AJ, 157, 114

Brogi M., Snellen I. A. G., de Kok R. J., Albrecht S., Birkby J., de Mooij E. J. W., 2012, Nature, 486, 502

Brogi M., de Kok R. J., Birkby J. L., Schwarz H., Snellen I. A. G., 2014, A&A, 565, A124

Brogi M., de Kok R. J., Albrecht S., Snellen I. A. G., Birkby J. L., Schwarz H., 2016, ApJ, 817, 106

Brogi M., Giacobbe P., Guilluy G., de Kok R. J., Sozzetti A., Mancini L., Bonomo A. S., 2018, A&A, 615, A16

Brown T. M., 2001, ApJ, 553, 1006

Bryan M. L., Benneke B., Knutson H. A., Batygin K., Bowler B. P., 2018, Nature Astronomy, 2, 138

Burgasser A. J., 2014, in Astronomical Society of India Conference Series. pp 7–16

(arXiv:1406.4887)

Burgasser A. J., et al., 2015, ApJS, 220, 18

Burke C. J., et al., 2014, ApJS, 210, 19

Burke C. J., et al., 2015, ApJ, 809, 8

Burningham B., Marley M. S., Line M. R., Lupu R., Visscher C., Morley C. V., Saumon D., Freedman R., 2017, MNRAS, 470, 1177

Burningham B., et al., 2021, MNRAS, 506, 1944

Burrows A., Sharp C. M., 1999, ApJ, 512, 843

Burrows A., Volobuyev M., 2003, ApJ, 583, 985

Burrows A., Hubbard W. B., Lunine J. I., Liebert J., 2001, Reviews of Modern Physics, 73, 719

Cabot S. H. C., Madhusudhan N., Hawker G. A., Gandhi S., 2019, MNRAS, 482, 4422

Caffau E., Ludwig H. G., Steffen M., Freytag B., Bonifacio P., 2011, Sol. Phys., 268, 255

Calamari E., et al., 2022, arXiv e-prints, p. arXiv:2210.13614

Canty J. I., et al., 2015, MNRAS, 450, 454

Carmichael T. W., et al., 2022, MNRAS, 514, 4944

Carter A. L., et al., 2023, ApJ, 951, L20

Chabrier G., Johansen A., Janson M., Rafikov R., 2014, in Beuther H., Klessen R. S., Dullemond C. P., Henning T., eds, Protostars and Planets VI. pp 619–642 (arXiv:1401.7559), doi:10.2458/azu˙uapress˙9780816531240-ch027

Charbonneau D., Brown T. M., Noyes R. W., Gilliland R. L., 2002, ApJ, 568, 377

Charbonneau D., et al., 2005, ApJ, 626, 523

Charbonneau D., et al., 2009, Nature, 462, 891

Chiavassa A., Brogi M., 2019, A&A, 631, A100

Coles P. A., Yurchenko S. N., Tennyson J., 2019, MNRAS, 490, 4638

Crossfield I. J. M., Kreidberg L., 2017, AJ, 154, 261

Crossfield I. J. M., Barman T., Hansen B. M. S., 2011, ApJ, 736, 132

Crossfield I. J. M., Barman T., Hansen B. M. S., Howard A. W., 2013, A&A, 559, A33

Cushing M. C., et al., 2008, ApJ, 678, 1372

Cushing M. C., et al., 2011, ApJ, 743, 50

Czesla S., Schröter S., Schneider C. P., Huber K. F., Pfeifer F., Andreasen D. T., Zechmeister M., 2019, PyA: Python astronomy-related packages (ascl:1906.010)

Deibert E. K., de Mooij E. J. W., Jayawardhana R., Fortney J. J., Brogi M., Rustamkulov Z., Tamura M., 2019, AJ, 157, 58

Del Burgo C., Martín E. L., Zapatero Osorio M. R., Hauschildt P. H., 2009, A&A, 501, 1059

Delorme J.-R., et al., 2021, Journal of Astronomical Telescopes, Instruments, and Systems, 7, 035006

Deming D., Wiedemann G., Bjoraker G., 2000, Prospects for Direct Spectral Detection and Characterization of "Hot Jupiters". p. 308

Deming D., Brown T. M., Charbonneau D., Harrington J., Richardson L. J., 2005, ApJ, 622, 1149

Deming D., et al., 2013, ApJ, 774, 95

Dressing C. D., Charbonneau D., 2015, ApJ, 807, 45

Espinoza N., Fortney J. J., Miguel Y., Thorngren D., Murray-Clay R., 2017, ApJ, 838, L9

Esteves L. J., de Mooij E. J. W., Jayawardhana R., Watson C., de Kok R., 2017, AJ, 153, 268

Faherty J. K., Burgasser A. J., Cruz K. L., Shara M. M., Walter F. M., Gelino C. R., 2009, AJ, 137, 1

Faherty J. K., et al., 2012, ApJ, 752, 56

Faherty J. K., et al., 2016, ApJS, 225, 10

Figueira P., Pont F., Mordasini C., Alibert Y., Georgy C., Benz W., 2009, A&A, 493, 671

Filippazzo J. C., Rice E. L., Faherty J., Cruz K. L., Van Gordon M. M., Looper D. L., 2015, ApJ, 810, 158

Flagg L., Johns-Krull C. M., Nofi L., Llama J., Prato L., Sullivan K., Jaffe D. T., Mace G., 2019, ApJ, 878, L37

Fletcher L. N., et al., 2007, Icarus, 189, 457

Foreman-Mackey D., Hogg D. W., Lang D., Goodman J., 2013, PASP, 125, 306

Fortney J. J., Mordasini C., Nettelmann N., Kempton E. M. R., Greene T. P., Zahnle K., 2013, ApJ, 775, 80

Fraine J., et al., 2014, Nature, 513, 526

Freedman R. S., Marley M. S., Lodders K., 2008, ApJS, 174, 504

Freedman R. S., Lustig-Yaeger J., Fortney J. J., Lupu R. E., Marley M. S., Lodders K.,

2014, ApJS, 214, 25

Fressin F., et al., 2013, ApJ, 766, 81

Fu G., Deming D., Knutson H., Madhusudhan N., Mandell A., Fraine J., 2017, ApJ, 847, L22

GRAVITY Collaboration et al., 2017, A&A, 602, A94

Gagné J., et al., 2018, ApJ, 856, 23

Gao P., Benneke B., 2018, ApJ, 863, 165

Gao P., et al., 2023, ApJ, 951, 96

Geballe T. R., Saumon D., Golimowski D. A., Leggett S. K., Marley M. S., Noll K. S., 2009, ApJ, 695, 844

Gibson N. P., et al., 2020, MNRAS, 493, 2215

Gonzales E. C., Burningham B., Faherty J. K., Cleary C., Visscher C., Marley M. S., Lupu R., Freedman R., 2020, ApJ, 905, 46

Gonzales E. C., Burningham B., Faherty J. K., Visscher C., Marley M., Lupu R., Freedman R., Lewis N. K., 2021, ApJ, 923, 19

Gonzales E. C., Burningham B., Faherty J. K., Lewis N. K., Visscher C., Marley M., 2022, ApJ, 938, 56

Gordon I. E., et al., 2017, J. Quant. Spec. Radiat. Transf., 203, 3

Gray D. F., 2008, The Observation and Analysis of Stellar Photospheres

Greene T. P., Line M. R., Montero C., Fortney J. J., Lustig-Yaeger J., Luther K., 2016, ApJ, 817, 17

Guilluy G., Sozzetti A., Brogi M., Bonomo A. S., Giacobbe P., Claudi R., Benatti S.,

2019, A&A, 625, A107

Hargreaves R. J., Gordon I. E., Rey M., Nikitin A. V., Tyuterev V. G., Kochanov R. V., Rothman L. S., 2020, ApJS, 247, 55

Harris G. J., Larner F. C., Tennyson J., Kaminsky B. M., Pavlenko Y. V., Jones H. R. A., 2008, MNRAS, 390, 143

Hawker G. A., Madhusudhan N., Cabot S. H. C., Gandhi S., 2018, ApJ, 863, L11

Heng K., Demory B.-O., 2013, ApJ, 777, 100

Hoch K. K. W., et al., 2022, AJ, 164, 155

Hoeijmakers H. J., Schwarz H., Snellen I. A. G., de Kok R. J., Bonnefoy M., Chauvin G., Lagrange A. M., Girard J. H., 2018, A&A, 617, A144

Hood C. E., et al., 2020, AJ, 160, 198

Hood C. E., Fortney J. J., Line M. R., Faherty J. K., 2023, arXiv e-prints, p. arXiv:2303.04885

Howe A. R., McElwain M. W., Mandell A. M., 2022, ApJ, 935, 107

Hsu C.-C., et al., 2021, ApJS, 257, 45

Huang X., Freedman R. S., Tashkun S. A., Schwenke D. W., Lee T. J., 2013, J. Quant. Spec. Radiat. Transf., 130, 134

Huang X., Gamache R. R., Freedman R. S., Schwenke D. W., Lee T. J., 2014, J. Quant. Spec. Radiat. Transf., 147, 134

Hubeny I., Burrows A., 2007, ApJ, 669, 1248

Iyer A. R., Swain M. R., Zellem R. T., Line M. R., Roudier G., Rocha G., Livingston J. H., 2016, ApJ, 823, 109

Jaffe D. T., Barnes S., Brooks C., Lee H., Mace G., Pak S., Park B.-G., Park C., 2016, GMTNIRS: progress toward the Giant Magellan Telescope near-infrared spectrograph. p. 990821, doi:10.1117/12.2232994

Jakobsen P., et al., 2022, A&A, 661, A80

Jones A., Noll S., Kausch W., Szyszka C., Kimeswenger S., 2013, A&A, 560, A91

Kass R. E., Raftery A. E., 1995, Journal of the American Statistical Association, 90, 773

Keenan P. C., 1985, in Hayes D. S., Pasinetti L. E., Philip A. G. D., eds, Vol. 111, Calibration of Fundamental Stellar Quantities. pp 121–136

Kempton E. M. R., Perna R., Heng K., 2014, ApJ, 795, 24

Kempton E. M. R., et al., 2018, PASP, 130, 114401

Kempton E. M. R., et al., 2023, arXiv e-prints, p. arXiv:2305.06240

Kirkpatrick J. D., 2005, ARA&A, 43, 195

Kirkpatrick J. D., et al., 2021, ApJS, 253, 7

Kitzmann D., Heng K., Oreshenko M., Grimm S. L., Apai D., Bowler B. P., Burgasser A. J., Marley M. S., 2020, ApJ, 890, 174

Knutson H. A., Benneke B., Deming D., Homeier D., 2014a, Nature, 505, 66

Knutson H. A., et al., 2014b, ApJ, 794, 155

Konopacky Q. M., Barman T. S., Macintosh B. A., Marois C., 2013, Science, 339, 1398

Kreidberg L., et al., 2014, Nature, 505, 69

Kreidberg L., Line M. R., Thorngren D., Morley C. V., Stevenson K. B., 2018, ApJ, 858, L6

Lecavelier des Etangs A., Lissauer J. J., 2022, New A Rev., 94, 101641

Leggett S. K., et al., 2012, ApJ, 748, 74

Leggett S. K., et al., 2021, ApJ, 918, 11

Li G., Gordon I. E., Rothman L. S., Tan Y., Hu S.-M., Kassi S., Campargue A., Medvedev E. S., 2015, ApJS, 216, 15

Li C., et al., 2020, Nature Astronomy, 4, 609

Line M. R., et al., 2013, ApJ, 775, 137

Line M. R., Fortney J. J., Marley M. S., Sorahana S., 2014, ApJ, 793, 33

Line M. R., Teske J., Burningham B., Fortney J. J., Marley M. S., 2015, ApJ, 807, 183

Line M. R., et al., 2017, ApJ, 848, 83

Line M. R., et al., 2021, Nature, 598, 580

Lodders K., 2010, in , Formation and Evolution of Exoplanets. p. 157, doi:10.1002/9783527629763.ch8

Lodders K., Fegley B., 2002, Icarus, 155, 393

Lodders K., Palme H., 2009, Meteoritics and Planetary Science Supplement, 72, 5154

Logsdon S. E., Mace G. N., McLean I. S., Martin E. C., 2018, ApJ, 867, 96

Lopez E. D., Fortney J. J., 2014, ApJ, 792, 1

Louie D. R., Deming D., Albert L., Bouma L. G., Bean J., Lopez-Morales M., 2018, PASP, 130, 044401

Lucas P. W., et al., 2010, MNRAS, 408, L56

Lueber A., Kitzmann D., Bowler B. P., Burgasser A. J., Heng K., 2022, ApJ, 930, 136

Lueber A., Kitzmann D., Fisher C. E., Bowler B. P., Burgasser A. J., Marley M., Heng

K., 2023, arXiv e-prints, p. arXiv:2305.07719

Luhman K. L., et al., 2023, ApJ, 949, L36

Lupu R. E., et al., 2014, ApJ, 784, 27

Lyons J. R., Gharib-Nezhad E., Ayres T. R., 2018, in 49th Annual Lunar and Planetary Science Conference. Lunar and Planetary Science Conference. p. 2907

Mace G., et al., 2018, in Proc. SPIE. p. 107020Q, doi:10.1117/12.2312345

Macintosh B., et al., 2014, Proceedings of the National Academy of Science, 111, 12661

Madhusudhan N., 2018, in Deeg H. J., Belmonte J. A., eds, , Handbook of Exoplanets. p. 104, doi:10.1007/978-3-319-55333-7˙104

Madhusudhan N., Seager S., 2009, ApJ, 707, 24

Mai C., Line M. R., 2019, ApJ, 883, 144

Marley M. S., Robinson T. D., 2015, ARA&A, 53, 279

Marley M. S., Seager S., Saumon D., Lodders K., Ackerman A. S., Freedman R. S., Fan X., 2002, ApJ, 568, 335

Marley M. S., Saumon D., Goldblatt C., 2010, ApJ, 723, L117

Marley M. S., et al., 2021, ApJ, 920, 85

Marocco F., et al., 2015, MNRAS, 449, 3651

Martin E. C., et al., 2017, ApJ, 838, 73

Martin E. C., et al., 2018, in Proc. SPIE. p. 107020A (arXiv:1808.06024), doi:10.1117/12.2312266

Mawet D., et al., 2019, in BAAS. p. 134 (arXiv:1908.03623)

Mayor M., Queloz D., 1995, Nature, 378, 355

McGovern M. R., Kirkpatrick J. D., McLean I. S., Burgasser A. J., Prato L., Lowrance P. J., 2004, ApJ, 600, 1020

McLean I. S., et al., 1998, in Fowler A. M., ed., Society of Photo-Optical Instrumentation Engineers (SPIE) Conference Series Vol. 3354, Proc. SPIE. pp 566–578, doi:10.1117/12.317283

McLean I. S., McGovern M. R., Burgasser A. J., Kirkpatrick J. D., Prato L., Kim S. S., 2003, ApJ, 596, 561

McLean I. S., Prato L., McGovern M. R., Burgasser A. J., Kirkpatrick J. D., Rice E. L., Kim S. S., 2007, ApJ, 658, 1217

Miles B. E., et al., 2020, AJ, 160, 63

Miles B. E., et al., 2023, ApJ, 946, L6

Miller-Ricci Kempton E., Zahnle K., Fortney J. J., 2012, ApJ, 745, 3

Mollière P., Snellen I. A. G., 2019, A&A, 622, A139

Mollière P., et al., 2022, ApJ, 934, 74

Morley C. V., Fortney J. J., Marley M. S., Visscher C., Saumon D., Leggett S. K., 2012, ApJ, 756, 172

Morley C. V., Fortney J. J., Kempton E. M. R., Marley M. S., Visscher C., Zahnle K., 2013, ApJ, 775, 33

Morley C. V., Fortney J. J., Marley M. S., Zahnle K., Line M., Kempton E., Lewis N., Cahoy K., 2015, ApJ, 815, 110

Morley C. V., Knutson H., Line M., Fortney J. J., Thorngren D., Marley M. S., Teal D., Lupu R., 2017, AJ, 153, 86

Morley C. V., et al., 2018, ApJ, 858, 97

Morley C. V., Skemer A. J., Miles B. E., Line M. R., Lopez E. D., Brogi M., Freedman R. S., Marley M. S., 2019, ApJ, 882, L29

Moses J. I., et al., 2013, ApJ, 777, 34

Mukherjee S., Fortney J. J., Batalha N. E., Karalidi T., Marley M. S., Visscher C., Miles B. E., Skemer A. J. I., 2022, ApJ, 938, 107

Mukherjee S., Batalha N. E., Fortney J. J., Marley M. S., 2023, ApJ, 942, 71

Mullally F., et al., 2015, ApJS, 217, 31

Nakajima T., Oppenheimer B. R., Kulkarni S. R., Golimowski D. A., Matthews K., Durrance S. T., 1995, Nature, 378, 463

Nettelmann N., Fortney J. J., Kramm U., Redmer R., 2011, ApJ, 733, 2

Newton E. R., Irwin J., Charbonneau D., Berta-Thompson Z. K., Dittmann J. A., 2016, ApJ, 821, L19

Noll K. S., Geballe T. R., Marley M. S., 1997, ApJ, 489, L87

Noll S., Kausch W., Barden M., Jones A. M., Szyszka C., Kimeswenger S., Vinther J., 2012, A&A, 543, A92

Öberg K. I., Murray-Clay R., Bergin E. A., 2011, ApJ, 743, L16

Origlia L., et al., 2014, High resolution near IR spectroscopy with GIANO-TNG. p. 91471E, doi:10.1117/12.2054743

Palma-Bifani P., et al., 2023, A&A, 670, A90

Park C., et al., 2014, Design and early performance of IGRINS (Immersion Grating Infrared Spectrometer). p. 91471D, doi:10.1117/12.2056431

Parmentier V., Crossfield I. J. M., 2018, in Deeg H. J., Belmonte J. A., eds, , Handbook of Exoplanets. p. 116, doi:10.1007/978-3-319-55333-7˙116

Patience J., King R. R., De Rosa R. J., Vigan A., Witte S., Rice E., Helling C., Hauschildt P., 2012, A&A, 540, A85

Petigura E. A., Howard A. W., Marcy G. W., 2013, Proceedings of the National Academy of Science, 110, 19273

Petrus S., et al., 2020, A&A, 633, A124

Petrus S., et al., 2021, A&A, 648, A59

Petrus S., et al., 2022, arXiv e-prints, p. arXiv:2207.06622

Petrus S., et al., 2023, A&A, 670, L9

Phillips M. W., et al., 2020, A&A, 637, A38

Piette A. A. A., Madhusudhan N., 2020, MNRAS, 497, 5136

Pino L., et al., 2018, A&A, 619, A3

Piskorz D., et al., 2018, AJ, 156, 133

Polyansky O. L., Kyuberis A. A., Zobov N. F., Tennyson J., Yurchenko S. N., Lodi L., 2018, MNRAS, 480, 2597

Quirrenbach A., et al., 2016, CARMENES: an overview six months after first light. p. 990812, doi:10.1117/12.2231880

Rauscher E., et al., 2019, in AAS/Division for Extreme Solar Systems Abstracts. p. 333.06

Rey M., Nikitin A. V., Tyuterev V. G., 2017, ApJ, 847, 105

Richard C., et al., 2012, J. Quant. Spec. Radiat. Transf., 113, 1276

Ricker G. R., et al., 2015, Journal of Astronomical Telescopes, Instruments, and Systems, 1, 014003

Rieke G. H., et al., 2015, PASP, 127, 584

Rigby J., et al., 2023, PASP, 135, 048001

Robinson T. D., 2017, ApJ, 836, 236

Rodgers C. D., 2000, Inverse Methods for Atmospheric Sounding: Theory and Practice, doi:10.1142/3171.

Rodler F., Lopez-Morales M., Ribas I., 2012, ApJ, 753, L25

Rogers L. A., Seager S., 2010, ApJ, 712, 974

Rothman L. S., et al., 2010a, J. Quant. Spec. Radiat. Transf., 111, 2139

Rothman L. S., et al., 2010b, J. Quant. Spec. Radiat. Transf., 111, 2139

Rothman L. S., et al., 2013, J. Quant. Spec. Radiat. Transf., 130, 4

Rowe J. F., et al., 2015, ApJS, 217, 16

Saumon D., Geballe T. R., Leggett S. K., Marley M. S., Freedman R. S., Lodders K., Fegley B. J., Sengupta S. K., 2000, ApJ, 541, 374

Saumon D., et al., 2007, ApJ, 656, 1136

Schwarz G., 1978, Annals of Statistics, 6, 461

Schwarz H., Ginski C., de Kok R. J., Snellen I. A. G., Brogi M., Birkby J. L., 2016, A&A, 593, A74

Seager S., Lissauer J. J., 2010, in Seager S., ed., , Exoplanets. pp 3–13

Showman A. P., Guillot T., 2002, A&A, 385, 166

Simcoe R. A., et al., 2013, PASP, 125, 270

Sing D. K., et al., 2016, Nature, 529, 59

Snellen I. A. G., de Kok R. J., de Mooij E. J. W., Albrecht S., 2010, Nature, 465, 1049

Snellen I. A. G., Brandl B. R., de Kok R. J., Brogi M., Birkby J., Schwarz H., 2014, Nature, 509, 63

Snellen I., et al., 2015, A&A, 576, A59

Sorahana S., Yamamura I., 2012, ApJ, 760, 151

Sparks W. B., Ford H. C., 2002, ApJ, 578, 543

Speagle J. S., 2020, MNRAS, 493, 3132

Stevenson K. B., 2016, ApJ, 817, L16

Sullivan P. W., et al., 2015, ApJ, 809, 77

Szydłowski M., Krawiec A., Kurek A., Kamionka M., 2015, European Physical Journal C, 75, 5

Tannock M. E., Metchev S., Hood C. E., Mace G. N., Fortney J. J., Morley C. V., Jaffe D. T., Lupu R., 2022, MNRAS, 514, 3160

Tennyson J., Yurchenko S. N., 2012, MNRAS, 425, 21

Toon O. B., McKay C. P., Ackerman T. P., Santhanam K., 1989, J. Geophys. Res., 94, 16287

Tremblin P., Amundsen D. S., Chabrier G., Baraffe I., Drummond B., Hinkley S., Mourier P., Venot O., 2016, ApJ, 817, L19

Trotta R., 2008, Contemporary Physics, 49, 71

Vigan A., et al., 2022, in Schreiber L., Schmidt D., Vernet E., eds, Society of Photo-Optical Instrumentation Engineers (SPIE) Conference Series Vol. 12185, Adaptive

Optics Systems VIII. p. 121850S (arXiv:2207.06436), doi:10.1117/12.2629208

Virtanen P., et al., 2020, Nature Methods, 17, 261

Wakeford H. R., Sing D. K., 2015, A&A, 573, A122

Wakeford H. R., et al., 2017, ApJ, 835, L12

Wakeford H. R., Wilson T. J., Stevenson K. B., Lewis N. K., 2019, Research Notes of the AAS, 3, 7

Wang J., et al., 2022, AJ, 163, 189

Wilcomb K. K., Konopacky Q. M., Barman T. S., Theissen C. A., Ruffio J.-B., Brock L., Macintosh B., Marois C., 2020, AJ, 160, 207

Wildi F., et al., 2017, in Proc. SPIE. p. 1040018, doi:10.1117/12.2275660

Xuan J. W., et al., 2022, ApJ, 937, 54

Yurchenko S. N., Tennyson J., 2014, MNRAS, 440, 1649

Yurchenko S. N., Barber R. J., Tennyson J., 2011, MNRAS, 413, 1828

Yurchenko S. N., Tennyson J., Barber R. J., Thiel W., 2013, Journal of Molecular Spectroscopy, 291, 69

Zalesky J. A., Line M. R., Schneider A. C., Patience J., 2019, ApJ, 877, 24

Zalesky J. A., Saboi K., Line M. R., Zhang Z., Schneider A. C., Liu M. C., Best W. M. J., Marley M. S., 2022, ApJ, 936, 44

Zapatero Osorio M. R., Martín E. L., Béjar V. J. S., Bouy H., Deshpande R., Wainscoat R. J., 2007, ApJ, 666, 1205

Zellem R. T., et al., 2019, PASP, 131, 094401

Zhang Y., Snellen I. A. G., Brogi M., Birkby J. L., 2022, Research Notes of the American

Astronomical Society, 6, 194

Zhang Y., et al., 2021a, Nature, 595, 370

Zhang Y., Snellen I. A. G., Mollière P., 2021b, A&A, 656, A76

Zhang Z., Liu M. C., Marley M. S., Line M. R., Best W. M. J., 2021, ApJ, 921, 95

de Kok R. J., Brogi M., Snellen I. A. G., Birkby J., Albrecht S., de Mooij E. J. W., 2013, A&A, 554, A82

de Kok R. J., Birkby J., Brogi M., Schwarz H., Albrecht S., de Mooij E. J. W., Snellen I. A. G., 2014, A&A, 561, A150

Šubjak J., et al., 2020, AJ, 159, 151